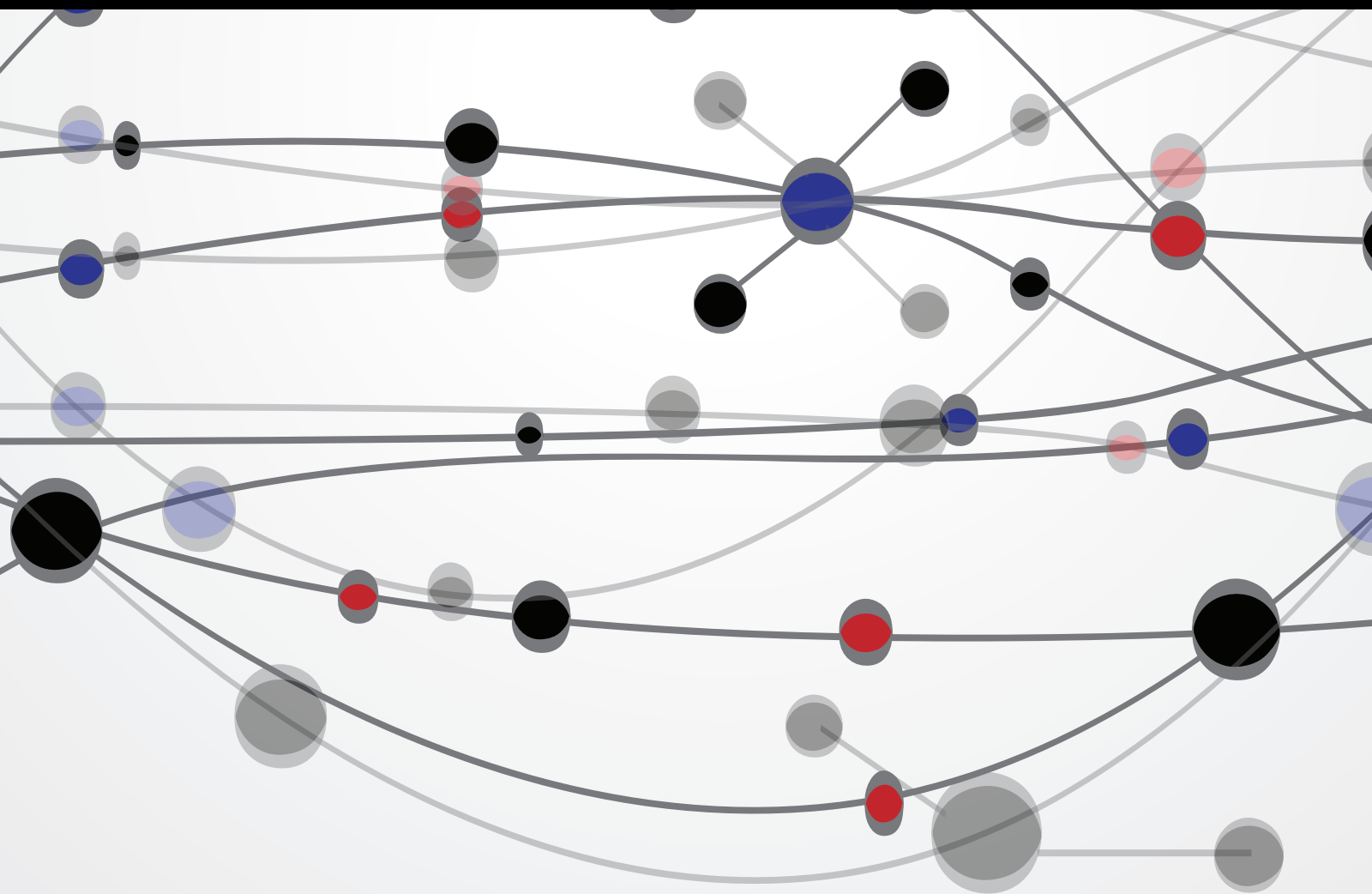


Semiconductor-Based Photocatalytic, Photoelectrochemical, and Photovoltaic Solar-Energy Conversion

Guest Editors: Dengwei Jing, Jinwen Shi, Patrick Meyrueis,
and Han Zhou





**Semiconductor-Based Photocatalytic,
Photoelectrochemical, and Photovoltaic
Solar-Energy Conversion**

The Scientific World Journal

**Semiconductor-Based Photocatalytic,
Photoelectrochemical, and Photovoltaic
Solar-Energy Conversion**

Guest Editors: Dengwei Jing, Jinwen Shi, Patrick Meyrueis,
and Han Zhou



Copyright © 2014 Hindawi Publishing Corporation. All rights reserved.

This is a special issue published in “The Scientific World Journal.” All articles are open access articles distributed under the Creative Commons Attribution License, which permits unrestricted use, distribution, and reproduction in any medium, provided the original work is properly cited.

Contents

Semiconductor-Based Photocatalytic, Photoelectrochemical, and Photovoltaic Solar-Energy Conversion, Dengwei Jing, Jinwen Shi, Patrick Meyrueis, and Han Zhou
Volume 2014, Article ID 695204, 1 page

Solar Tracking Error Analysis of Fresnel Reflector, Jiantao Zheng, Junjie Yan, Jie Pei, and Guanjie Liu
Volume 2014, Article ID 834392, 6 pages

Modeling, Control, and Simulation of Battery Storage Photovoltaic-Wave Energy Hybrid Renewable Power Generation Systems for Island Electrification in Malaysia, Nahidul Hoque Samrat, Norhafizan Bin Ahmad, Imtiaz Ahmed Choudhury, and Zahari Bin Taha
Volume 2014, Article ID 436376, 21 pages

Synthesis of CdIn₂S₄ Microsphere and Its Photocatalytic Activity for Azo Dye Degradation, Jianhui Huang, Wei Lin, and Jianqin Chen
Volume 2014, Article ID 241234, 6 pages

Photocatalysis and Photoelectrochemical Properties of Tungsten Trioxide Nanostructured Films, Chin Wei Lai
Volume 2014, Article ID 843587, 7 pages

Enhanced Water Splitting by Fe₂O₃-TiO₂-FTO Photoanode with Modified Energy Band Structure, Eul Noh, Kyung-Jong Noh, Kang-Seop Yun, Bo-Ra Kim, Hee-June Jeong, Hyo-Jin Oh, Sang-Chul Jung, Woo-Seung Kang, and Sun-Jae Kim
Volume 2013, Article ID 723201, 8 pages

Editorial

Semiconductor-Based Photocatalytic, Photoelectrochemical, and Photovoltaic Solar-Energy Conversion

Dengwei Jing,¹ Jinwen Shi,¹ Patrick Meyrueis,² and Han Zhou³

¹ *International Research Center for Renewable Energy, Xi'an Jiaotong University, Xi'an 710049, China*

² *Photonics Systems Laboratory, University of Strasbourg, 67412 Illkirch, France*

³ *Department of Colloid Chemistry, Max Planck Institute of Colloids and Interfaces, Research Campus Golm, 14476 Potsdam, Germany*

Correspondence should be addressed to Dengwei Jing; dwjing@mail.xjtu.edu.cn

Received 11 May 2014; Accepted 11 May 2014; Published 12 June 2014

Copyright © 2014 Dengwei Jing et al. This is an open access article distributed under the Creative Commons Attribution License, which permits unrestricted use, distribution, and reproduction in any medium, provided the original work is properly cited.

Semiconductor-based photocatalytic, photoelectrochemical, and photovoltaic solar-energy conversion has been considered very promising to address the energy and environmental challenges. At the heart of the technology is the lack of suitable semiconductor materials and efficient systems that can perform the solar-energy conversion efficiently and inexpensively. Much work needs to be done in this research field, for instance, full control of growth characteristics and physicochemical properties of targeted semiconductor materials and rational design of systems efficiently utilizing incident solar light.

The main objective of this special issue is to bring together researchers and engineers working on semiconductor-based solar-energy conversion and to bridge between fundamental materials research and solar-energy conversion. After critical peer review, 6 papers of high quality were selected from many submissions. The topics of all the accepted papers are closely related to the subject of this thematic issue. As per photovoltaic solar-energy conversion, N. H. Samrat et al. reported the modeling, control, and simulation of a PV-wave energy hybrid power generation system that is assumed to be used for island electrification in Malaysia. The concept is interesting and theoretically applicable. J. Zheng et al. described an interesting solar tracking error analysis for Fresnel reflector. Considering the rapidly increased use of Fresnel reflector in concentrating PV, the error analysis could be of importance for the design of such PV system. Tseng et al. reported an interleaved boost converter with coupled inductor for PV energy conversion. The proposed

soft-switching boost converter uses an interleaved method to increase its power density and coupled-inductor technology to extend its step-up voltage ratio. The proposed strategy has been demonstrated to be quite suitable for PV energy conversion.

Other three papers are related to the photocatalytic, photoelectrochemical application of semiconductor film as electrodes or powders as photocatalysts. Their work represented important progress in the design of semiconductors with multiple compositions, functional nanostructures, and, most importantly, enhanced properties. So the reported work is expected to be of interest for a broad range of readership.

In summary, semiconductor-based photocatalytic, photoelectrochemical, and photovoltaic solar-energy conversion is gaining more and more attention, and the papers presented in this special issue represent the important progress in their research. Nevertheless, many problems remain unresolved, and more research is necessary. We look forward to new progress on the basis of and beyond the work reported in this issue.

Dengwei Jing
Jinwen Shi
Patrick Meyrueis
Han Zhou

Research Article

Solar Tracking Error Analysis of Fresnel Reflector

Jiantao Zheng,^{1,2} Junjie Yan,¹ Jie Pei,² and Guanjie Liu²

¹ School of Energy and Power Engineering, Xi'an Jiaotong University, Xi'an 710049, China

² Huaneng Clean Energy Research Institute, Beijing 100098, China

Correspondence should be addressed to Jiantao Zheng; zhengjiantao@hnceri.com

Received 18 February 2014; Accepted 17 March 2014; Published 6 May 2014

Academic Editors: D. Jing, P. Meyrueis, J. Shi, and H. Zhou

Copyright © 2014 Jiantao Zheng et al. This is an open access article distributed under the Creative Commons Attribution License, which permits unrestricted use, distribution, and reproduction in any medium, provided the original work is properly cited.

Depending on the rotational structure of Fresnel reflector, the rotation angle of the mirror was deduced under the eccentric condition. By analyzing the influence of the sun tracking rotation angle error caused by main factors, the change rule and extent of the influence were revealed. It is concluded that the tracking errors caused by the difference between the rotation axis and true north meridian, at noon, were maximum under certain conditions and reduced at morning and afternoon gradually. The tracking error caused by other deviations such as rotating eccentric, latitude, and solar altitude was positive at morning, negative at afternoon, and zero at a certain moment of noon.

1. Introduction

Solar energy is plentiful and unlimited. Solar-photovoltaic power generation and solar thermal power generation are two basic solar-energy-utilization ways [1]. Owing to solar thermal power generation performing good stability, high reliability, long working time, and middle/high temperature steam provision, solar thermal power generation is widely focused in the energy field.

In 1960s, Giovanni Francica (Italy) firstly applied linear Fresnel reflector (LFR) for development of linear and two-axis tracking Fresnel steam generating system [2, 3]. From then on, lots of research was gradually carried out. In order to enhance the utilization of land area and reduce the shading created by adjacent reflectors, Mills and Morrison invented the multiabsorption towers technology based on compact linear Fresnel reflector which was suitable for large-scale solar thermal power plants [4, 5]. Mathur et al. proposed an optimal design of the width of primary mirror [6]. Sootha and Negi made optical design and focused characteristic research about linear concentrating technology without secondary reflectors [7]. Du et al. estimated the tracking and radiation for LFR system by increasing the spacing between the adjacent reflectors and got the best method for estimating height [8]. Pu and Xia designed a small linear concentrating test device, conducting the light tracing simulation and concentration research [9].

The above research is carried out to optimize the key components and eventually achieve the real-time sun tracking by the tracking program, so the concentrating system and tracking accuracy are key components to realize the high efficiency, high performance parameters in Fresnel solar thermal power generation system. There are many ways to realize the solar tracking. In the condition of low tracking accuracy requirement or reducing complexity and costs, open loop single axis tracking method can be used [10]. Du et al. resolved sun vector properly by using vector method, and then the tracking rotation angle was got after simple geometric derivation, which was applicable to linear Fresnel reflector without the eccentric structure [11].

This paper analyzes the main impact factors of the tracking accuracy of Fresnel solar reflectors and calculated the tracking error and its influence.

2. Fresnel Tracking System Error and Analysis

2.1. Fresnel Lens System Introduction. The LFR field which are comprise of 11 rows of flat mirrors can be imagined as a broken-up parabolic trough reflector by using linear segments to focus the radiation, as Figure 1 shows. The parabolic trough shape is simulated by several flat reflectors at different positions, in order to make the sunlight reflect to the receiver tubes fixed on the top of mirrors. Each mirror must

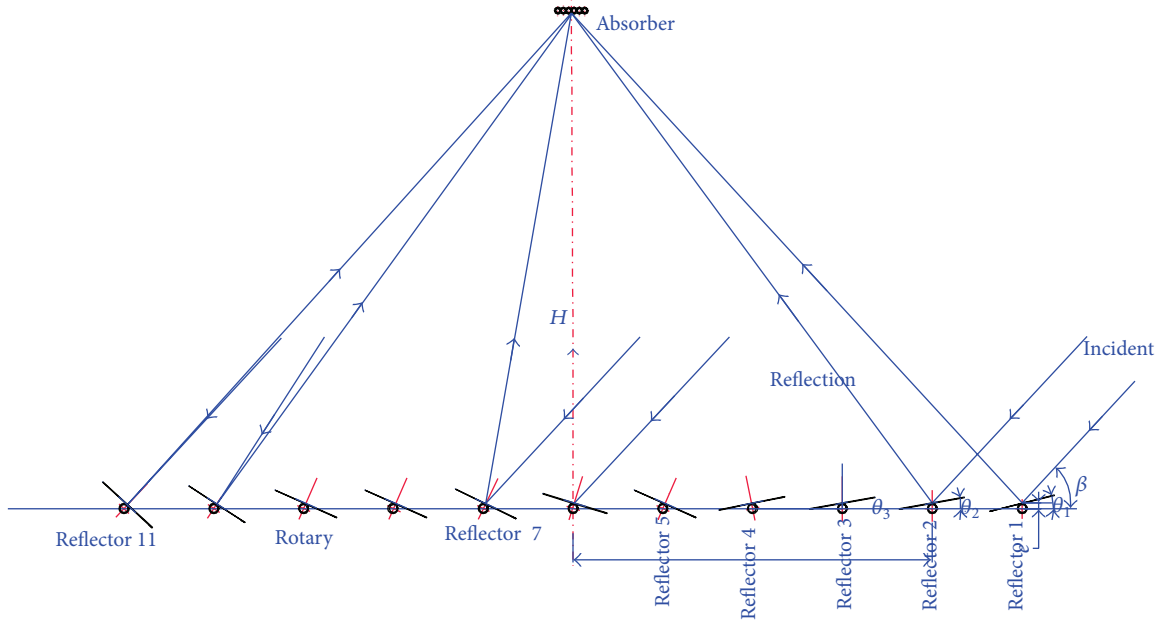


FIGURE 1: Diagram of the Fresnel solar reflection technology.

tracks accurately, to ensure the virtual parabolic shape and keep the reflected solar radiation on the absorber all the time. Therefore, improving tracking accuracy plays an important role in promoting the collection efficiency [12].

The tracking error of Fresnel reflectors could be affected by time, mirror exocentric structure, collector orientation, height of absorbers, axis position, solar altitude angle, and so on. This paper analyzed the influence of these factors on the tracking error.

2.2. The Analysis of Tracking System Rotation Angle. It is well known that in order to track the sun the exact position of sun is necessary. The main parameters of sun position are shown in Figure 2, which are sun declination angle δ , hour angle ω , elevation angle θ , geographic latitude φ , and longitude ϵ . The sunlight irradiates to point P on the surface of earth, which is determined by elevation angle h_s and azimuth angle λ of the tangent plane. The sun position in the tracking system is calculated by international SPA algorithm whose accuracy is 0.0003° [13, 14].

In Figure 2, the sunlight irradiates to the center of mirror $(L, 0, 0)$ at space vector of elevation angle h_s and azimuth angle λ ; reflection light is vector \vec{r} , and the normal vector of central point of mirror is \vec{n} . The angle between mirror and horizontal X -axis direction is θ , and the location position of reflected rays on collector tubes is $(0, e, H)$.

If the mirror rotation center is located on the center of mirror, one has the following:

$$\vec{r} = \left(\frac{-L}{R}, \frac{e}{R}, \frac{H}{R} \right), \quad R = \sqrt{L^2 + e^2 + H^2},$$

$$\vec{n} = (-\sin \theta, 0, \cos \theta),$$

$$\vec{s} = (s_x, s_y, s_z),$$

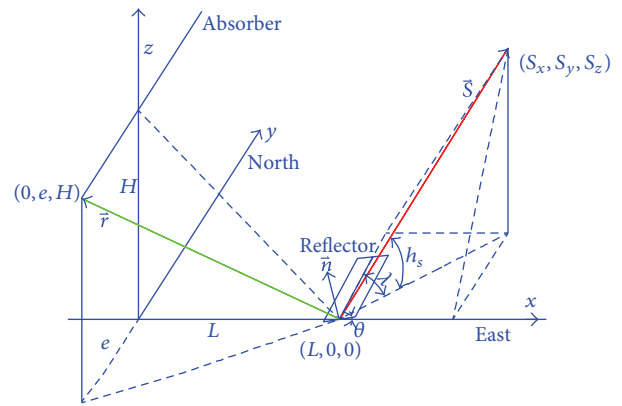


FIGURE 2: Diagram of ray reflection of Fresnel technology.

$$\vec{s} \times \vec{n} = \begin{vmatrix} \vec{i} & \vec{j} & \vec{k} \\ s_x & s_y & s_z \\ -\sin \theta & 0 & \cos \theta \end{vmatrix} = s_y \cos \theta \vec{i} - (s_x \cos \theta + s_z \sin \theta) \vec{j} + s_y \sin \theta \vec{k},$$

$$\vec{n} \times \vec{r} = \begin{vmatrix} \vec{i} & \vec{j} & \vec{k} \\ -\sin \theta & 0 & \cos \theta \\ -\frac{L}{R} & \frac{e}{R} & \frac{H}{R} \end{vmatrix} = -\frac{e}{R} \cos \theta \vec{i} - \left(\frac{L}{R} \cos \theta - \frac{H}{R} \sin \theta \right) \vec{j} - \frac{e}{R} \sin \theta \vec{k}.$$

(1)

According to the law of light reflection, it is known that

$$\begin{aligned}
 s_y \cos \theta &= -\frac{e}{R} \cos \theta, \\
 s_x \cos \theta + s_z \sin \theta &= \frac{L}{R} \cos \theta - \frac{H}{R} \sin \theta, \\
 s_y \sin \theta &= -\frac{e}{R} \sin \theta.
 \end{aligned}
 \tag{2}$$

Then

$$\begin{aligned}
 \tan \theta &= \frac{L/R - s_x}{H/R + s_z}, \\
 e &= \frac{-s_y}{\sqrt{1 - s_y^2}} \sqrt{L^2 + H^2}.
 \end{aligned}
 \tag{3}$$

In the equation, s_x, s_y, s_z are the vector components of sun position along the X, Y, Z axis. The rotation angle of mirror θ and deviation distance e of reflected solar radiation in the direction of absorber can be calculated at a certain moment.

There are two rotation methods for mirror rotation: one is rotating around the geometric center of the mirror and the other is using the reflector supporting shaft as rotation center. This paper mainly analyzes the tracking error under the second condition.

When the rotation axis is not located in the center of mirror, L and H in formula (3) need to be replaced by $L-R \sin \theta$ and $H-R \cos \theta$. Assuming that mirror width is 800 mm, spacing between adjacent reflectors is 200 mm, and focal length is 7 m, the tracking error under different deviation factors was obtained by computer program.

3. The Influence of Main Parameters Deviation on Tracking Accuracy

3.1. The Influence of Frame Eccentric Error on Tracking Accuracy. Because the rotation axis of reflectors is not located at the geometry center of the mirror, the orbit of incident point on the mirror usually is an ellipse. Meanwhile, reflectors in different columns rotate at different speeds at the same time, which results in different tracking errors. Figure 3 shows that, at winter solstice, when reflection mirror 1 and reflection mirror in middle column performed 10 cm eccentric distance, at 8:00, the tracking error is 0.26° and the tracking error of reflection mirror 11 is 0.1° . At 18:00, the tracking errors of reflection mirrors 1, 6, and 11 are $-0.12^\circ, -0.28^\circ,$ and -0.27° , and the minimum error happens at 15:00, 12:40, and 10:25, respectively.

Eccentric deviation value has significant effect on the tracking error. It is shown in Figure 4 that the maximum tracking error at winter solstice, caused by different eccentric distances (5, 10, 15, and 20 cm), mainly occurs at 8:00 or 18:00. Nevertheless, the tracking error at around 12:40 is zero, and the ratio of eccentric distance is consistent with the ratio of tracking error.

In different dates throughout the year, the tracking error caused by reflector eccentric also changes. As shown in

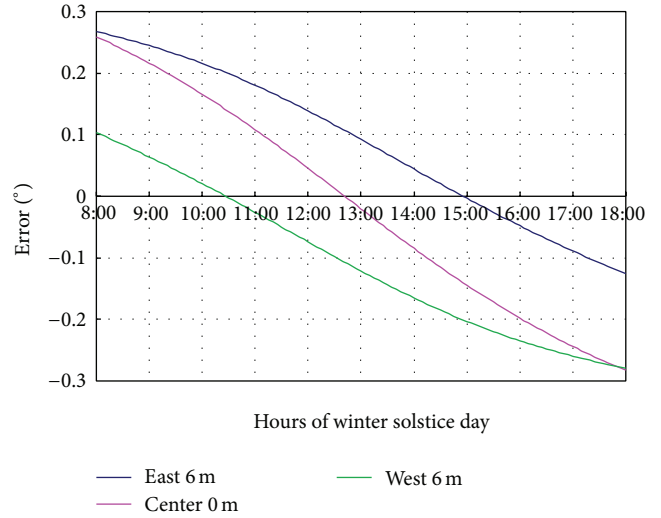


FIGURE 3: The tracking error caused by eccentric deviation of different column.

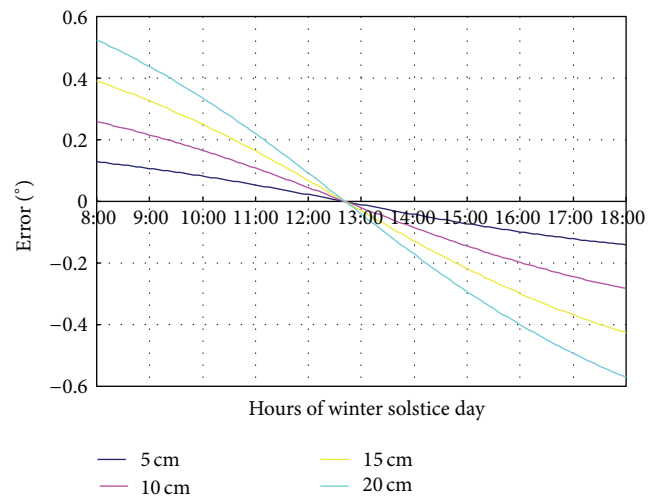


FIGURE 4: The tracking error caused by eccentric deviation of the middle columns.

Figure 5, the maximum tracking error of middle column (column 6) with a 10 cm eccentric deviation at the typical dates of vernal equinox, summer solstice, autumnal equinox, and winter solstice happens at 8:00 and 18:00 with about 0.23° . Especially, the maximum tracking error happens at winter solstice.

Because of eccentric influence, different columns and different time lead to different tracking error. On the same day, there is a big error at morning and afternoon but almost no error at a certain moment at noon.

3.2. The Influence of North-South Orientation Deviation on Tracking Accuracy. Because geographic north/south is different from geomagnetic north/south, there exists magnetic declination. The sun location algorithm is based on geographic north and south; thus the truly geographical

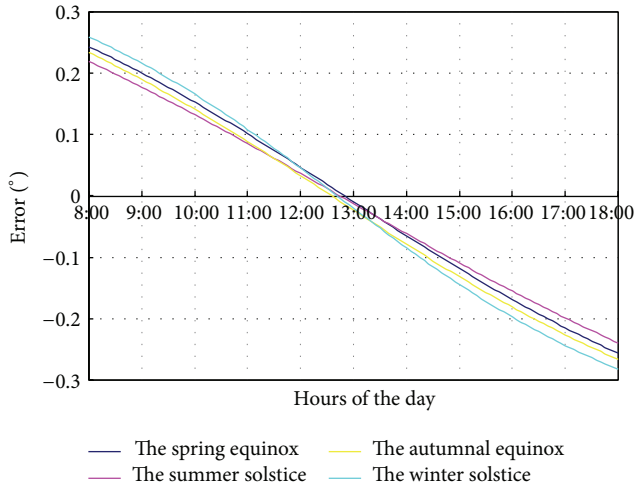


FIGURE 5: The tracking error on four typical days.

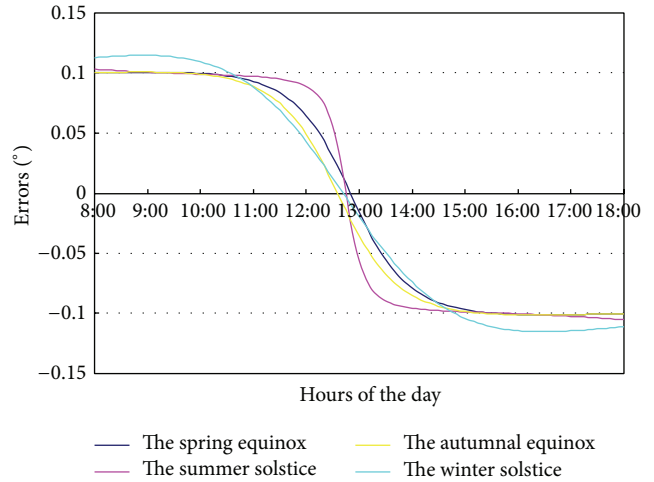


FIGURE 7: The tracking error of solar altitude 0.2° deviation.

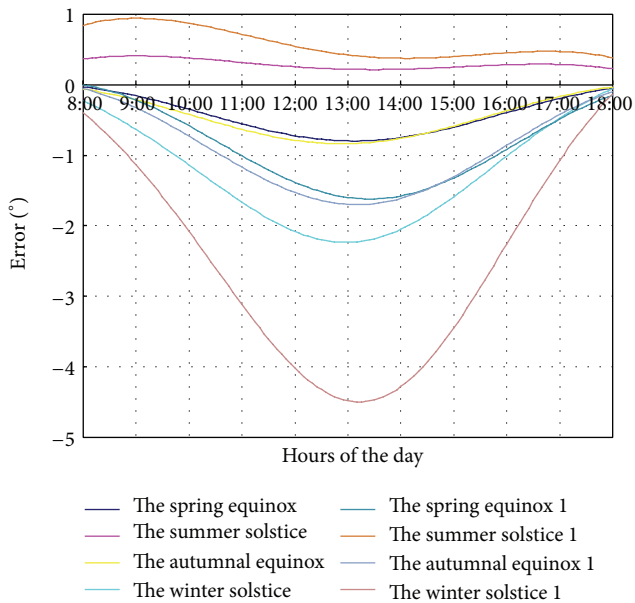


FIGURE 6: The tracking error caused by north and south direction negative deviation on four typical days.

north/south of solar field is very important for the tracking system. Assuming that southwest is negative deviation for solar field orientation, the influence of north-south orientation deviation on tracking error can be simulated. The variation trend of tracking error for different orientation deviation (5° and 10°) at vernal equinox, summer solstice, autumnal equinox, and winter solstice is shown in Figure 6.

When the orientation axis lays west of 10°, the tracking error curves at winter solstice has the biggest slope. The tracking error increases from 0.66° (8:00) to 4.5° (12:00), then it decreases gradually. At 18:00, the value is around 0.08°.

The tracking errors at vernal equinox and autumnal equinox are much smaller than that at winter solstice. The error value is positive, which means the mirror rotation

angle is bigger relative to theoretical tracking angle and the tracking system runs too fast. Nevertheless, at summer solstice, tracking error presents a negative value, which implies that the tracking system is too slow.

The tracking error with an orientation axis deviation of 5° westward, comparing with an orientation axis deviation of 10° deviation, has a similar changing trend, but the value of the former is about half of the latter.

3.3. The Influence of Center Height and Center Distance Deviation on Tracking Accuracy. The height of middle column (column 6) and center distance deviation performs no effect on tracking error in each typical day.

When the height of reflectors shows -10 cm and -5 cm deviation, its tracking error is 0.2° and 0.1°, respectively. When the center distance shows -10 cm deviation, its tracking error is 0.4°. In the case of -5 cm deviation, its tracking error is 0.2°.

3.4. The Influence of Solar Altitude Angle Deviation on Tracking Accuracy. In the Fresnel solar concentrating system, solar altitude angle is one of the key factors for calculating the sun position. It is shown in Figure 7, when the deviation of solar altitude angle is 0.2°, that the tracking error from 8:00 to 11:00 and from 14:00 to 18:00 is about 0.1°. The error is positive in the morning (rotating too fast), while it is negative in the afternoon (rotating too slow). In the three hours from 11:00 to 14:00, the error changes gradually from 0.1° to -0.1°. However, at summer solstice, this change mainly occurs from 12:30 to 13:30.

3.5. The Influence of Geographical Latitude-Longitude Deviation on Tracking Accuracy. Owing to the low energy density of solar energy, it usually requires large area for solar power generation; thus the geographical latitude longitudes are different in different area of solar field. As shown in Figure 8, when the longitude has 0.1° deviation at winter solstice, the tracking error increases from 0.047° (at 8:00) to 0.062° (at 12:45) then decreases to 0.045° (at 18:00). The error value and

TABLE 1: Effect of the tracing error for the middle mirror.

Influence factor	Eccentric distance	Eccentric distance	Eccentric distance	Eccentric distance
Value	10 cm	10 cm	10 cm	10 cm
Typical data	Winter solstice	Autumnal equinox	Summer solstice	Spring equinox
Maximum error	0.27°	0.23°	0.22°	0.24
Influence factor	Eccentric distance	Eccentric distance	North and south deviation	North and south deviation
Value	5 cm	15 cm	-10°	-10°
Typical data	Winter solstice	Winter solstice	Winter solstice	Spring equinox
Maximum error	0.17°	0.4°	4.5°	1.6°
Influence factor	North and south deviation	Autumnal equinox	Center distance deviation	Height deviation
Value	-10°	-10°	-10 cm	-10 cm
Typical data	Autumnal equinox	Summer solstice	Typical day	Typical day
Maximum error	1.6°	-0.94°	0°	0°
Influence factor	Longitude deviation	Longitude deviation	Longitude deviation	Angle deviation
Value	0.1°	0.1°	0.1°	0.05°
Typical data	Winter solstice	Equinoxes	Summer solstice	Typical day
Maximum error	0.065°	0.053°	0.045°	0.025°
Influence factor	Latitude deviation	Latitude deviation	Latitude deviation	Angle deviation
Value	0.1°	0.1°	0.1°	0.2°
Typical data	Winter solstice	Equinoxes	Summer solstice	Typical day
Maximum error	0.026°	0.008°	0.013°	0.12°

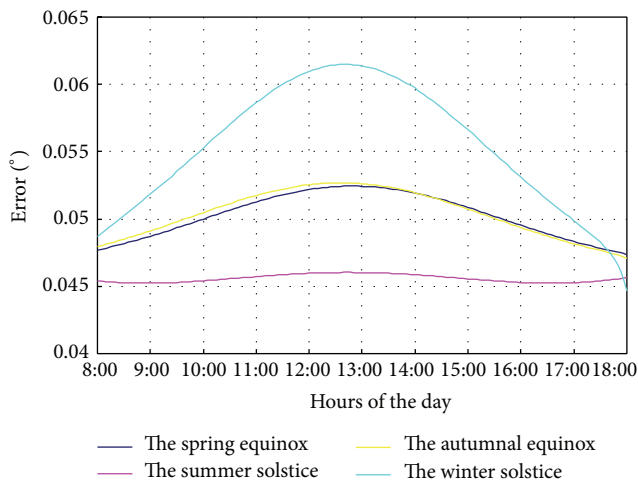


FIGURE 8: The tracking error of longitude 0.1° deviation.

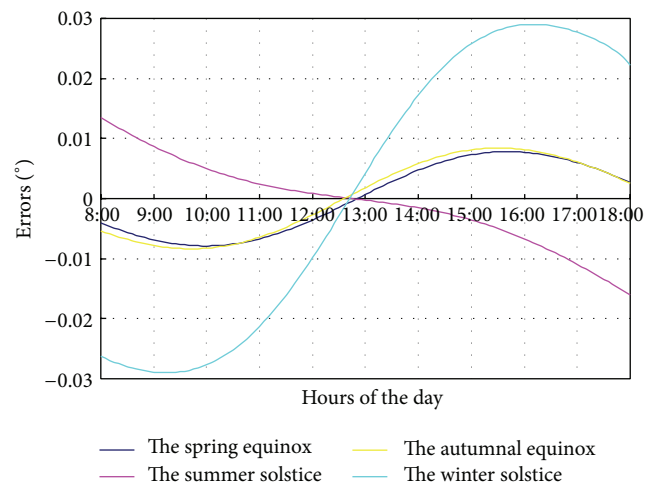


FIGURE 9: The tracking error of latitude 0.1° deviation.

trend at vernal equinox and autumnal equinox are consistent. At summer solstice, the tracking error is almost invariable in the whole day.

Figure 9 shows that, when latitude has 0.1° deviation at winter solstice, vernal equinox, and autumnal equinox, the trends of the tracking errors curves are similar. However, the error value at winter solstice is much higher than the other two typical days. Different from other typical day, the error value at summer solstice gradually decreases from +0.013° (at 8:00) to zero then increases to a maximum value of 0.016° at 18:00.

3.6. Comparison of All Factors. By calculating the tracking error of middle reflector (column 6) due to the various factors, the comparison results are shown in Table 1.

From Table 1, the order of influence on tracking error is north-south orientation deviation, eccentric deviation, altitude angle deviation, longitude deviation, latitude deviation, center distance, and height deviation successively.

Height deviation almost has no effect on the tracking precision of middle mirror. However, if the height deviation is 10 cm, the tracking error for mirror 1 is 0.2° in typical day, and if the center distance deviation is 10 cm, the error can reach 0.4°.

4. Conclusion

There are many influence factors for Fresnel solar tracking error, such as reflector supporting structure, rotation axis position, driver accuracy, tracking software algorithm, deviation of geographic latitude-longitude, and related structure error. When north-south orientation and geographic longitude have deviation, the tracking error is biggest at noon, and it is smaller at morning and afternoon on the same day. When the mirror rotating center, solar altitude, and geographic latitude have deviation, the error value changes from positive to negative, and at a certain moment in the midday, the error is zero.

Tracking error has a great influence on the solar collection efficiency. For Fresnel solar concentrating system, if the error of tracking is 0.1° , the light energy collected by the receiver tubes decreases by 10%. Therefore, improving efficiency and accuracy of automatic tracking system plays an important role in increasing solar collection efficiency and energy generation and decreasing the cost of solar power.

Conflict of Interests

The authors declare that there is no conflict of interests regarding the publication of this paper.

Acknowledgment

The authors gratefully acknowledge the financial support of the National Energy Applied Technology Research and Engineering Demonstration Project (no. NY20130101).

References

- [1] J. Song and S. Ding, *Solar Thermal Power Plant*, Mechanical Industry Press, Beijing, China, 2013.
- [2] X. Li, "The current situation and development of linear concentrated solar thermal power generation technology," *East China Electric Power*, vol. 39, no. 12, pp. 2071–2075, 2011.
- [3] G. Francia, "Pilot plants of solar steam generating stations," *Solar Energy*, vol. 12, no. 1, pp. 51–64, 1968.
- [4] D. R. Mills and G. L. Morrison, "Compact linear Fresnel reflector solar thermal powerplants," *Solar Energy*, vol. 68, no. 3, pp. 263–283, 2000.
- [5] D. R. Mills, G. Morrison, J. Pye, and P. Le Lièvre, "Multi-tower line focus Fresnel array project," *Journal of Solar Energy Engineering*, vol. 128, no. 1, pp. 118–120, 2006.
- [6] S. S. Mathur, T. C. Kandpal, and B. S. Negi, "Optical design and concentration characteristics of linear Fresnel reflector solar concentrators-I. Mirror elements of varying width," *Energy Conversion and Management*, vol. 31, no. 3, pp. 205–219, 1991.
- [7] G. D. Sootha and B. S. Negi, "A comparative study of optical designs and solar flux concentrating characteristics of a linear Fresnel reflector solar concentrator with tubular absorber," *Solar Energy Materials and Solar Cells*, vol. 32, no. 2, pp. 169–186, 1994.
- [8] C. Du, P. Wang, Y. Wu, and C. Ma, "Linear Fresnel collecting lens radiation quantity calculation method," *Journal of Chemical Engineering*, vol. 62, no. 1, pp. 179–184, 2011.
- [9] S. Pu and C. Xia, "Optical design of a linear reflecting solar concentrator with all-flat mirrors," *Transactions of the Chinese*

Society of Agricultural Engineering, vol. 27, no. 12, pp. 282–285, 2011.

- [10] X. Zheng and Q. Huang, "Study on sun tracking methods and application," *Energy Technology*, vol. 24, no. 4, pp. 149–151, 2003.
- [11] C. Du, P. Wang, C. Ma, and Y. Wu, "Vector algorithm of tracking tilted angle of Fresnel concentrated solar power systems," *Acta Energetica Solaris Sinica*, vol. 32, no. 6, pp. 831–835, 2011.
- [12] R. Grena, "Five new algorithms for the computation of sun position from 2010 to 2110," *Solar Energy*, vol. 86, no. 5, pp. 1323–1337, 2012.
- [13] X. Huang, Z. Wang, Y. Li, H. Qiu, and W. Huang, *Solar Thermal Power Generation Technology*, China Electric Power Press, Beijing, China, 2013.
- [14] Q. Li, J. Zheng, H. Xu, M. Liu, and J. Pei, "The development of linear Fresnel solar thermal power generation technology," *Solar Energy*, no. 7, pp. 41–45, 2012.

Research Article

Modeling, Control, and Simulation of Battery Storage Photovoltaic-Wave Energy Hybrid Renewable Power Generation Systems for Island Electrification in Malaysia

**Nahidul Hoque Samrat,¹ Norhafizan Bin Ahmad,¹
Imtiaz Ahmed Choudhury,¹ and Zahari Bin Taha²**

¹ Centre for Product Design and Manufacturing (CPDM), Department of Mechanical Engineering, Faculty of Engineering, University of Malaya, 50603 Kuala Lumpur, Malaysia

² Innovative Manufacturing, Mechatronics and Sports Laboratory (iMAMS), Faculty of Manufacturing Engineering, Universiti Malaysia Pahang, Pekan, 26600 Pahang, Malaysia

Correspondence should be addressed to Norhafizan Bin Ahmad; norhafizan@um.edu.my

Received 21 February 2014; Accepted 23 March 2014; Published 30 April 2014

Academic Editors: P. Meyrueis and H. Zhou

Copyright © 2014 Nahidul Hoque Samrat et al. This is an open access article distributed under the Creative Commons Attribution License, which permits unrestricted use, distribution, and reproduction in any medium, provided the original work is properly cited.

Today, the whole world faces a great challenge to overcome the environmental problems related to global energy production. Most of the islands throughout the world depend on fossil fuel importation with respect to energy production. Recent development and research on green energy sources can assure sustainable power supply for the islands. But unpredictable nature and high dependency on weather conditions are the main limitations of renewable energy sources. To overcome this drawback, different renewable sources and converters need to be integrated with each other. This paper proposes a standalone hybrid photovoltaic- (PV-) wave energy conversion system with energy storage. In the proposed hybrid system, control of the bidirectional buck-boost DC-DC converter (BBDC) is used to maintain the constant dc-link voltage. It also accumulates the excess hybrid power in the battery bank and supplies this power to the system load during the shortage of hybrid power. A three-phase complex vector control scheme voltage source inverter (VSI) is used to control the load side voltage in terms of the frequency and voltage amplitude. Based on the simulation results obtained from Matlab/Simulink, it has been found that the overall hybrid framework is capable of working under the variable weather and load conditions.

1. Introduction

In developing countries like Malaysia, the development of islands is mostly related to the electric power availability, because there are many islands all over Malaysia where electric power grid is not available. Among these island communities electricity is supplied by traditional energy sources, but the fuel cost increases significantly with remoteness. Furthermore, the energy produced by the conventional sources raises the greenhouse gas emissions, which may be the key source of global warming. It is projected that, by 2020, Malaysia will release 285.73 million tons of CO₂ which is an increase of 68.86% compared to the amount of CO₂ emitted in the year 2000. In Malaysia, electricity generation

alone contributes 43.40% of the total CO₂ emission, which is the largest among all sectors [1]. Malaysia signed the previous Kyoto protocol on reduction of CO₂ emission to the atmosphere. For this reason, the Malaysian government is very much concerned about environmental issue and the government wants the overall improvement of the CO₂ emission. As a result, island electrification in Malaysia by renewable energy sources is the only way to overcome the challenge.

Among the renewable energy sources, solar energy is an environmentally friendly and the fastest growing green energy source. But the main drawback of the PV system is that the power produced by this system is highly dependent on climatic conditions. For example, a PV system could

not able to produce any power at night and during cloudy periods. So the PV system intermittently produces power, which means that PV system may not totally satisfy the load demand at each instant. This problem can be solved by combining PV system with other renewable energy sources and/or energy storage systems (such wind, wave, fuel cell, battery bank, ultracapacitor bank, and hydrogen storage tank) in a suitable hybrid framework [2–7]. As an island surrounded by sea, wave energy can be considered one of the environmentally friendly hybrid power generating sources for island communities.

Wave energy is a renewable energy generated by the force of surface waves from the ocean. Although many wave energy conversion techniques have been patented and new patents are granted each month [8], there are only nine basic techniques on which these conversions are based. The nine basic techniques are cavity resonators or oscillating water column, pressure devices, heaving and pitching bodies, Salter's duck, surging wave energy converters, particle motion converters, Russell's rectifier, Cockerell's rafts, and wave focusing techniques [9–11]. In this study, an OWC wave energy converter device is preferred because OWC is generally considered one of the most promising wave energy conversion devices among the various wave energy converters [12]. However, assisting PV-wave hybrid system with battery banks makes economic sense when satisfying the transient's period or peak load demands. Battery based energy storage system is widely used in standalone system because of its mature technology, high efficiency, quick response, and low cost [13, 14]. Without battery bank, the PV-wave hybrid system must meet all load demands, thus increasing the cost and size of the hybrid system.

An extensive review based on the solar and other relevant areas has been reported in the literature to model hybrid renewable energy system. Among them, Onar et al. [6, 7] described detail dynamic model, mathematical modeling, and simulation of both solar/fuel cell/ultracapacitor and wind/fuel cell/ultracapacitor hybrid system. In [15], a wind, PV, and wave based large-scale hybrid system integration was analyzed and grid connection was discussed. Bhende et al. [13] investigated a standalone fuel cell based wind energy supply system. Power conditioning for hydrogen storage based wind energy system has been reported in [16]. In [2, 6, 7, 13, 15], the authors are silent about the wave energy based hybrid system design for island communities.

In this paper, detailed modeling, control, and simulation of a PV-wave hybrid renewable power generation system are developed for island communities. OWC wave energy device is used to generate the electrical power from the sea waves and PV model is used to generate power from solar radiation. A control algorithm is developed using a BBDC between the battery bank and dc-link, and a switch mode inverter is placed at the load side end. A simple passive L-C filter is placed after the inverter at load side end to eliminate the unwanted high frequency harmonics, which are generated by the load side VSI based on the inverter switching frequency.

The simulation model can be used not only for analyzing the battery storage based PV-wave hybrid system performance, but also for designing and sizing the system HRES to

meet the consumer load demands for any available meteorological condition. The proposed standalone PV-wave hybrid system model in this paper has been modeled, designed, and simulated using Matlab, Simulink, and SimPowerSystems software packages. In addition, simulation results are presented to verify the effectiveness of the proposed system under variable weather conditions.

The sequential workflow hints of this paper are as follows. In Section 2 the complete modeling process of PV-wave hybrid system has been described with the necessary mathematical equations. And also Section 2 presents the control algorithm of dc-link voltage and load side VSI. In Section 3, according to the meteorological data, Perhentian Island is considered as a potential area for generating electric power from PV and wave energy sources. In Section 4 all the necessary simulation results and discussions are given to check the feasibility of the hybrid system. Finally, a conclusion has been drawn by combining all the important points of the study in Section 5.

2. System Description

In this section, the detailed simulation model of PV-wave hybrid renewable power generation system is briefly described. Figure 1 shows the complete block diagram of the standalone PV-wave HRES. The developed hybrid system consists of five main parts: PV system, OWC system, battery bank, a BBDC with proportional integral (PI) control duty cycle, and a pulse width modulation (PWM) insulated-gate bipolar transistor (IGBT) VSI located at the load side. The solar PV system consists of PV array and DC-DC converter with maximum power point tracking (MPPT) algorithm. In PV system, MPPT is used to increase the system efficiency by controlling DC-DC converter. The OWC system was configured by the bidirectional Darrieus turbine driven permanent magnet synchronous generator (PMSG) and an AC-DC three-phase rectifier.

In the HRES, the renewable PV and wave energy system is considered as a main power generation source to meet the system load demand and battery bank is used as a backup energy storage system. The HRES is proposed to implement in island areas in Malaysia; hence, if generated power from HRES is not enough to meet the system load demands, then battery bank will deliver power to balance the system power demand. To interface PV, wave, and battery bank in hybrid framework, the dc-link voltage must be constant. Hence, a BBDC with PI controller is used in the HRES to maintain the constant dc-link voltage. A three-phase VSI with relatively complex vector control scheme is used at load side to control load side voltage in terms of the amplitude and frequency. The detailed description of each component of the overall HRES and controller is given in the following parts.

2.1. Modeling and Characteristics of PV System. Solar PV systems generate electric power by converting solar photon energy into electrical energy in the form of direct current using solar cell or PV cell. Crystalline or polycrystalline materials are commonly used for solar cell [17]. Each of the

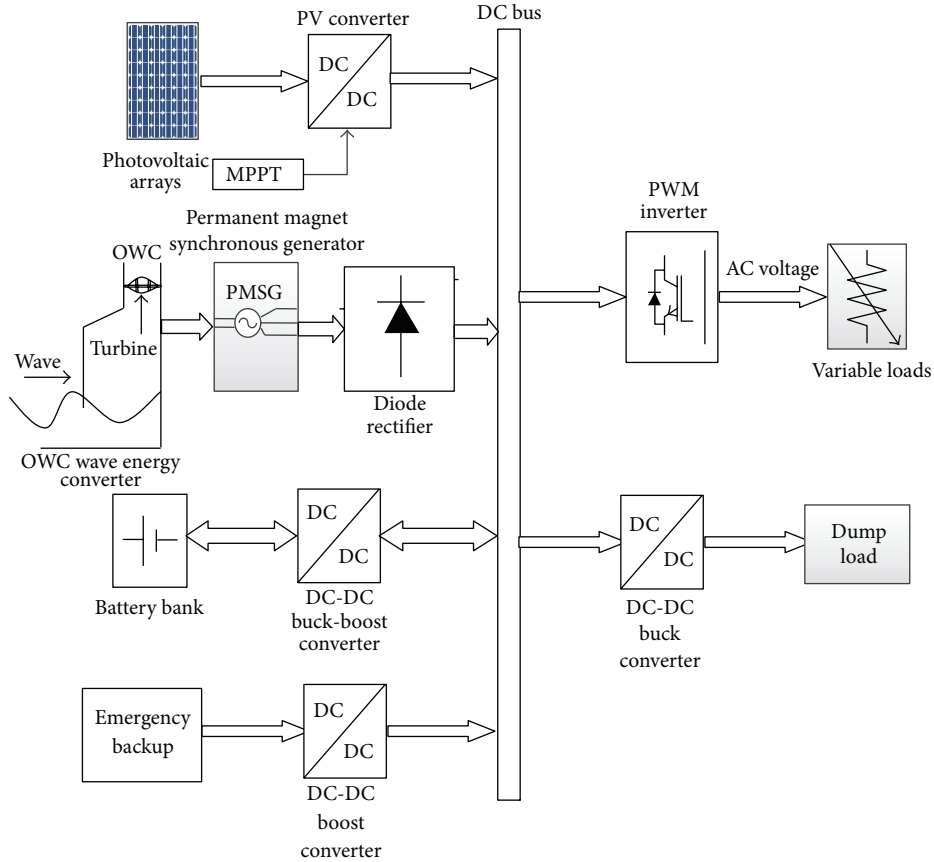


FIGURE 1: Block diagram of the proposed standalone PV-wave hybrid system.

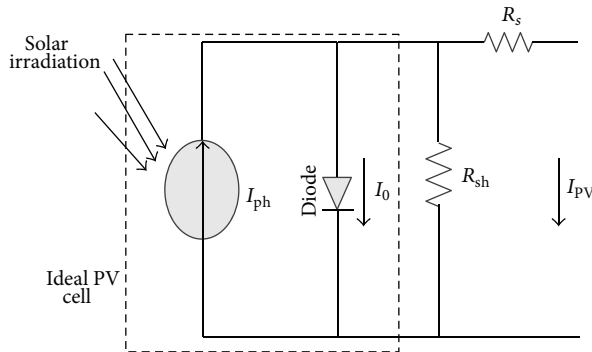


FIGURE 2: Circuit diagram of single diode PV model.

PV cells produces around 0.5 V and it is the smallest unit of the solar PV system. Cells are further connected in series or/and parallel combination to form a PV array. Figure 2 shows widely used one diode equivalent circuit model for a PV cell [18]. PV cell equivalent circuit model consists of a current source parallel with a diode and the output terminals of the circuit are connected to the load through the shunt and series resistor. The current-voltage characteristics of PV array can be expressed using some nonlinear mathematical exponential equations. The ideal relationship between voltage and current is given by [18–21]

$$\begin{aligned}
 I_{PV} &= I_{ph} - I_D - I_{sh} \\
 &= I_{ph} - I_0 \left[\exp \frac{q}{AKT} (V_{PV} + I_{PV}R_s) - 1 \right] \\
 &\quad - \frac{V_{PV} + I_{PV}R_s}{R_{sh}},
 \end{aligned} \tag{1}$$

where I_{PV} is the output current of the PV cell (A), I_{ph} is the photocurrent, I_D is the diode current, I_{sh} is the current through the shunt resistance, I_0 is the reverse saturation

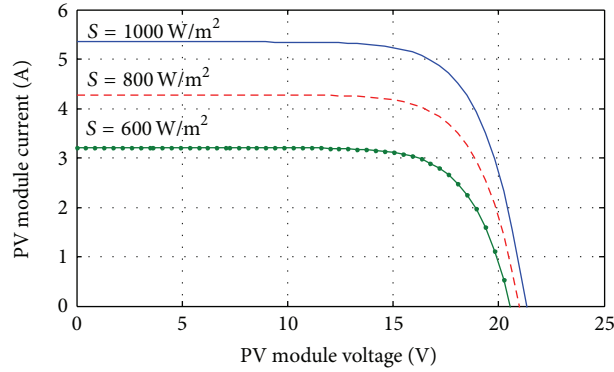


FIGURE 3: KOYCERA KC85T-87W PV model I-V characteristics curve with varying irradiation.

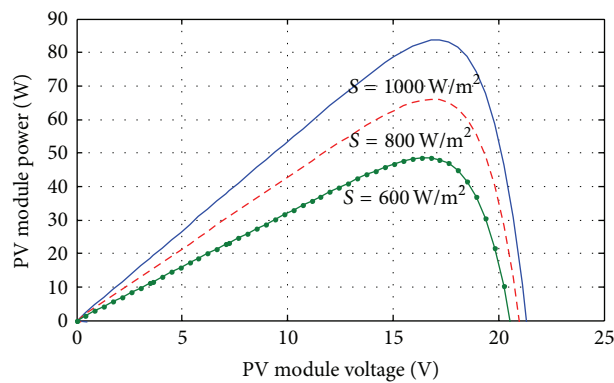


FIGURE 4: KOYCERA KC85T-87W PV model P-V characteristics curve with varying irradiation.

current, K , the Boltzmann constant $= 1.38 \times 10^{-23}$ (J/K), q , the charge of electron $= 1.6 \times 10^{-19}$ (C), T is the cell temperature (K), V_{PV} is the output terminal voltage of the PV cell (V), A is the quality factor (lies between 1.2 and 1.6 for crystalline silicon), R_s is the series resistance (Ω), and R_{sh} is the shunt resistance (Ω).

The output power from solar PV array is given by

$$P_{PV} = V_{PV} I_{PV} \eta_{conv}, \quad (2)$$

where η_{conv} is the DC-DC converter efficiency (typically 90–95%). In this paper total five KOYCERA KC85T-87W PV models are used for 400 W power generation and all the five models connected in series with one another. The power-voltage and current-voltage characteristics of KOYCERA KC85T-87W PV model are obtained according to the value of the variables I_{ph} , I_0 , R_{sh} , and R_s . The value of the variables can be collected from [18]; they usually provide values for I_{PV} and V_{PV} at open circuit, short circuit, and maximum power point and finally the number of the PV cells. The current-voltage and power-voltage characteristics of a solar PV module operating at a standard temperature of 25°C and different solar irradiance are shown in Figures 3 and 4.

According to solar irradiation or load current, the maximum output power of the PV module varies. Therefore, a proper control system is needed to use the PV model more efficiently as an electric power source by building a MPPT. There are many different MPPT methods discussed in

[18, 19, 22], among them perturbation and observation method (P&O) is most widely used because it is much simpler and needs fewer measured variables. In this paper from [19], P&O method is used for building MPPT in Simulink environment. According to (1), (2), and the literature described in [20, 21], PV model with MPPT is developed using Matlab Simulink, which is illustrated in Figures 5(a), 5(b), and 5(c).

2.2. Modeling of OWC. It should be noted that this paper focuses on the designing of a battery storage standalone PV-wave hybrid supply system for island communities and, therefore, the mathematical modeling for individual elements such as OWC wave chambers is simplified. The detailed design and complete mathematical modeling of OWC wave energy system can be found in [23–29], where more precise model is established.

The operating principle of the OWC as shown in Figure 6 is much like a wind energy system via the wave induced air pressurization principle. In this system sea wave motion causes the rise and fall of the water level within the wave chamber. This causes pressure oscillations, which can be used to drive a bidirectional air turbine. The bidirectional turbine extracts the kinetic energy of sea wave and turned it into mechanical energy which is fed into the electrical generator. The generator converts this mechanical energy into electrical energy which will feed directly either to the load or in the grid.

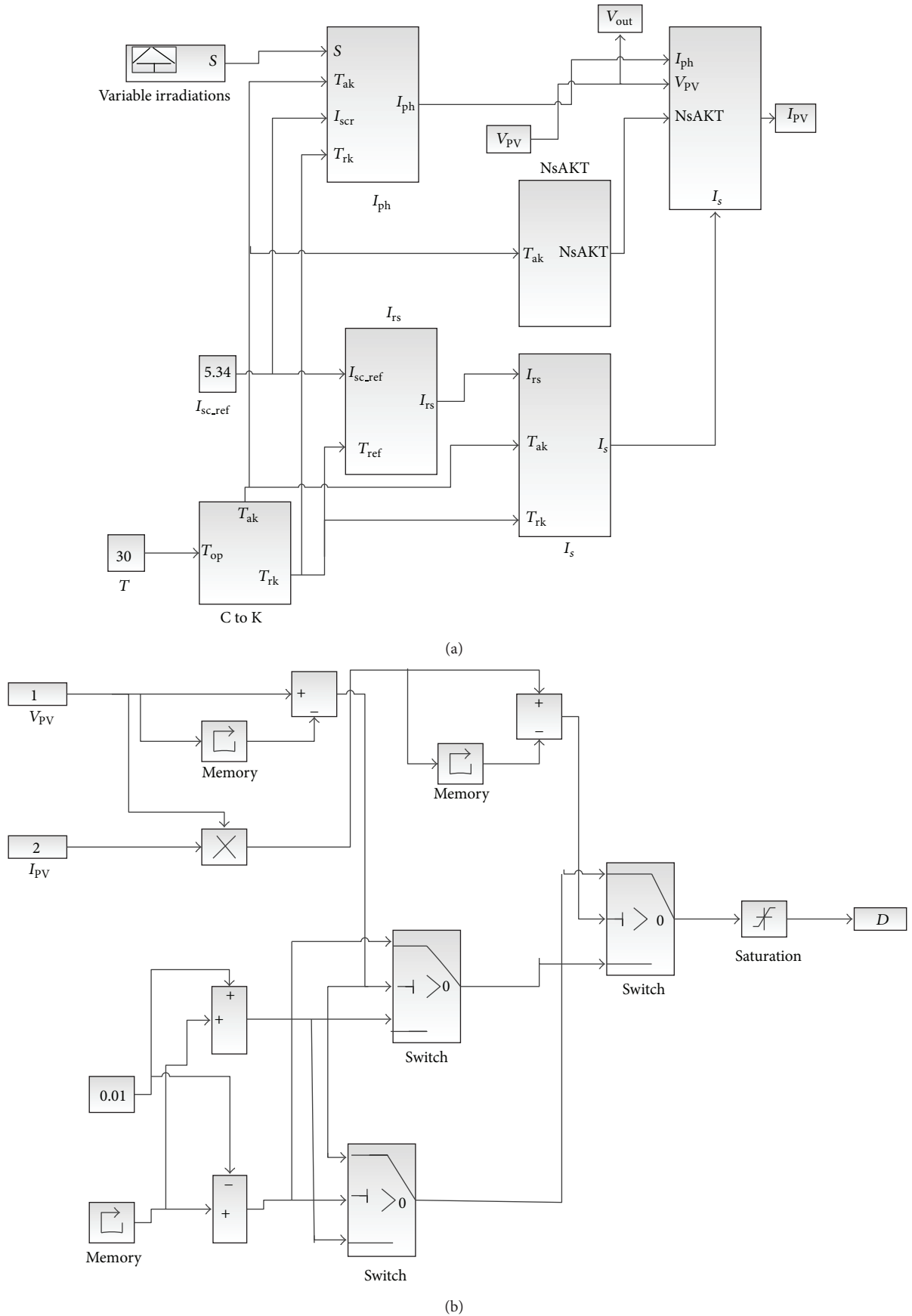


FIGURE 5: Continued.

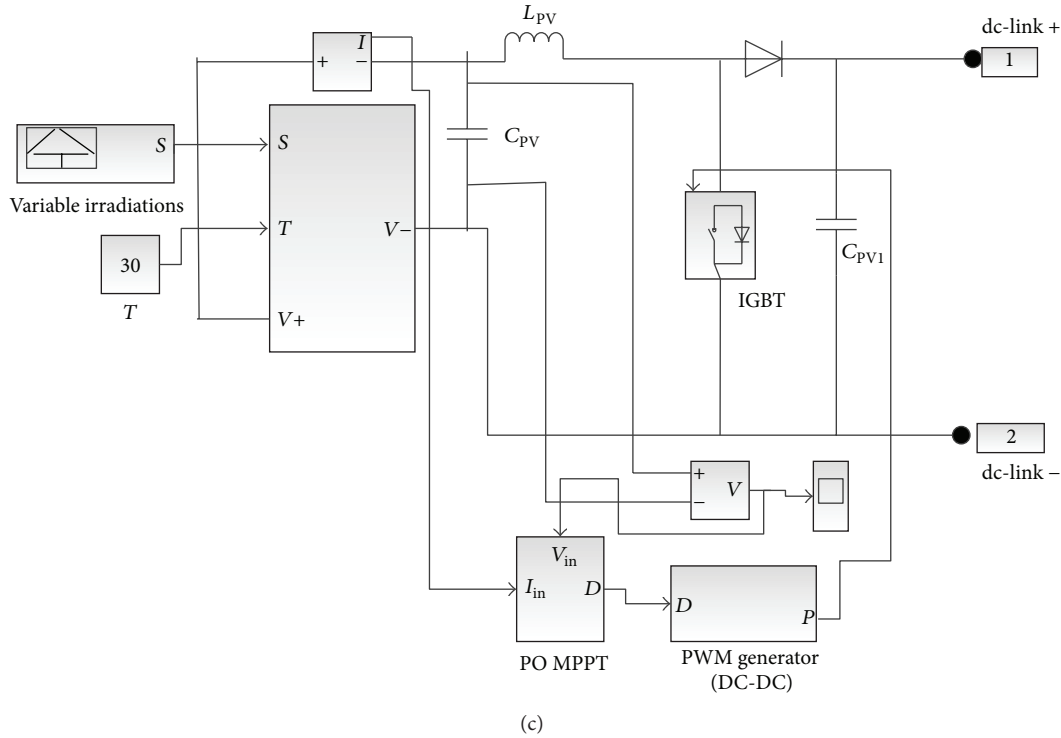


FIGURE 5: The Simulink diagram of the PV model with MPPT. (a) PV Simulink model; (b) MPPT model; (c) complete Simulink PV model with MPPT.

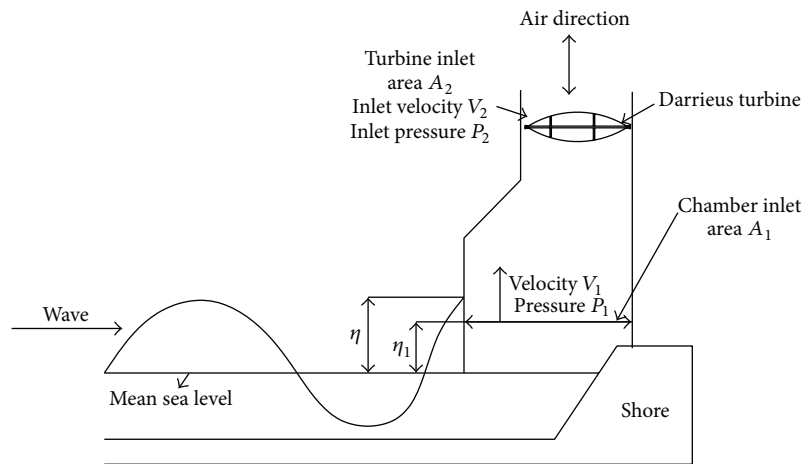


FIGURE 6: OWC chamber parameters.

In this section, a set of equations is present to describe the power generated by OWC system. As mentioned earlier, OWC wave energy operating principle is much like wind turbine system, so the power available at the wave turbine consists of two terms: air velocity term P_a and air pressure term P_{pt} . Therefore, the total inlet power can be described using the following equation:

$$\text{Inlet Power } P_{in} = P_a + P_{pt}, \tag{3}$$

where the power P_a acting on the turbine due to the air

velocity term is

$$P_a = \frac{\rho A_2 V_2^3}{2}. \tag{4}$$

The available output power developed by the OWC is a function of the turbine power coefficient C_p , so the total output power developed by the OWC is

$$P_{total} = (P_a + P_{pt}) \times C_p. \tag{5}$$

The power due to the air velocity term is straightforward and shown in (4). But power due to the pressure term is more

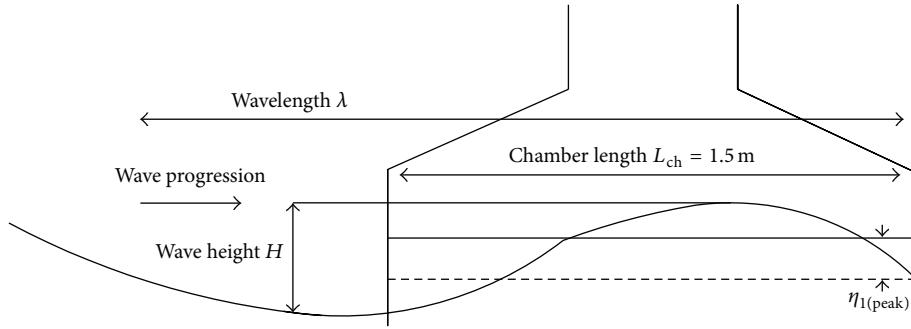


FIGURE 7: OWC full chamber arrangements [23].

complex. It is mainly depending on the surface elevation in OWC chamber. But this wave surface elevation further depends on the two major factors, namely, the turbine inlet velocity and air pressure term. Both of these factors are related to the OWC chamber length, water depth, and so forth. So, in this paper, the mathematical modelling of OWC wave energy system mainly focuses on the air pressure term and its derivative from the literature [23–29], which is discussed here.

Figures 6 and 7 illustrate the parameters related to the OWC. At first, it assumed that the regular outer wave free surface elevation can be stated as [24]

$$\text{Outer wave surface elevation } \eta_0 = \frac{H}{2} \cos\left(\frac{2\pi}{T}t\right), \quad (6)$$

where H is the wave height (m) and T is the wave period (s). If the chamber length of OWC is L_{ch} with respect to the wavelength, then free surface elevation in OWC can be approximated as follows:

$$\eta_1 = \frac{H_{in}}{2} \cos\left(\frac{2\pi}{T}t\right) \times \frac{2 \sin(\theta/2)}{\theta}, \quad (7)$$

where H_{in} is the averaged internal wave height (m) and it is calculated from the literature in [23, 25]. The angular chamber length θ (rad) is defined as

$$\theta = \frac{2\pi L_{ch}}{\lambda}, \quad (8)$$

where λ is the actual wave length; for calculating this wavelength an equation can be formulated [30] as follows:

$$\lambda \cong \left(1 - \frac{\pi d}{3\lambda_0}\right) \times T \sqrt{gd}, \quad (9)$$

where d is the water depth (m), g is the gravitational constant (9.81 ms^{-2}), and λ_0 is the theoretical deep water wavelength, which is given by [23]

$$\lambda_0 = \frac{gT^2}{2\pi}. \quad (10)$$

The velocity of the air adjacent to the internal free surface is the liner velocity of water height, where

$$V_1 = \frac{d\eta_1}{dt} = -\frac{\omega H_{in}}{\theta} \sin(\omega t) \times \sin\left(\frac{\theta}{2}\right), \quad (11)$$

$$\omega = \frac{2\pi}{T}.$$

Since the system is relatively low-pressure system, so the axial velocity passage through the turbine is

$$V_2 = \frac{A_1}{A_2} V_1 = -\frac{A_1}{A_2} \frac{\omega H_{in}}{\theta} \sin(\omega t) \times \sin\left(\frac{\theta}{2}\right), \quad (12)$$

where A_1 is the flow surface area of the chamber and A_2 is the inlet turbine area. The power P_{pt} available at the turbine depends on the volume of air flow rate Q across the turbine and the gradient of pressure. Hence, the power available at the turbine due to the air pressure term (for completeness, this equation is derived in Appendix D) is

$$P_{pt} = \left[-\frac{A_1}{A_2} \frac{H_{in}^2}{\theta^2} \omega^2 \{2 \cos(\omega t)^2 - 1\} \right. \\ \left. \times \sin^2\left(\frac{\theta}{2}\right) + \frac{Q}{A_2} (V_2 - V_1) \right] \times Q \times \rho. \quad (13)$$

According to (3) and (13), OWC model is developed using Matlab Simulink, which is illustrated in Figures 8(a) and 8(b).

2.3. Modeling of Battery. A standard battery model presented in [31] is implemented in this paper. To avoid the battery algebraic loop problem, this model uses only the state of charge (SOC) of the battery as a state variable. Moreover, model in [31] can precisely characterize four types of battery chemistries including lead-acid battery.

The battery is modeled using a simple series connected controlled voltage source with a constant resistive value, as shown in Figure 9, where the controlled voltage source is described by

$$E = E_0 - K \frac{Q}{Q - \int i dt} + A \exp\left(-B \int i dt\right), \quad (14)$$

$$V_{\text{Battery}} = E - R_{in} I_{\text{Battery}}, \quad (15)$$

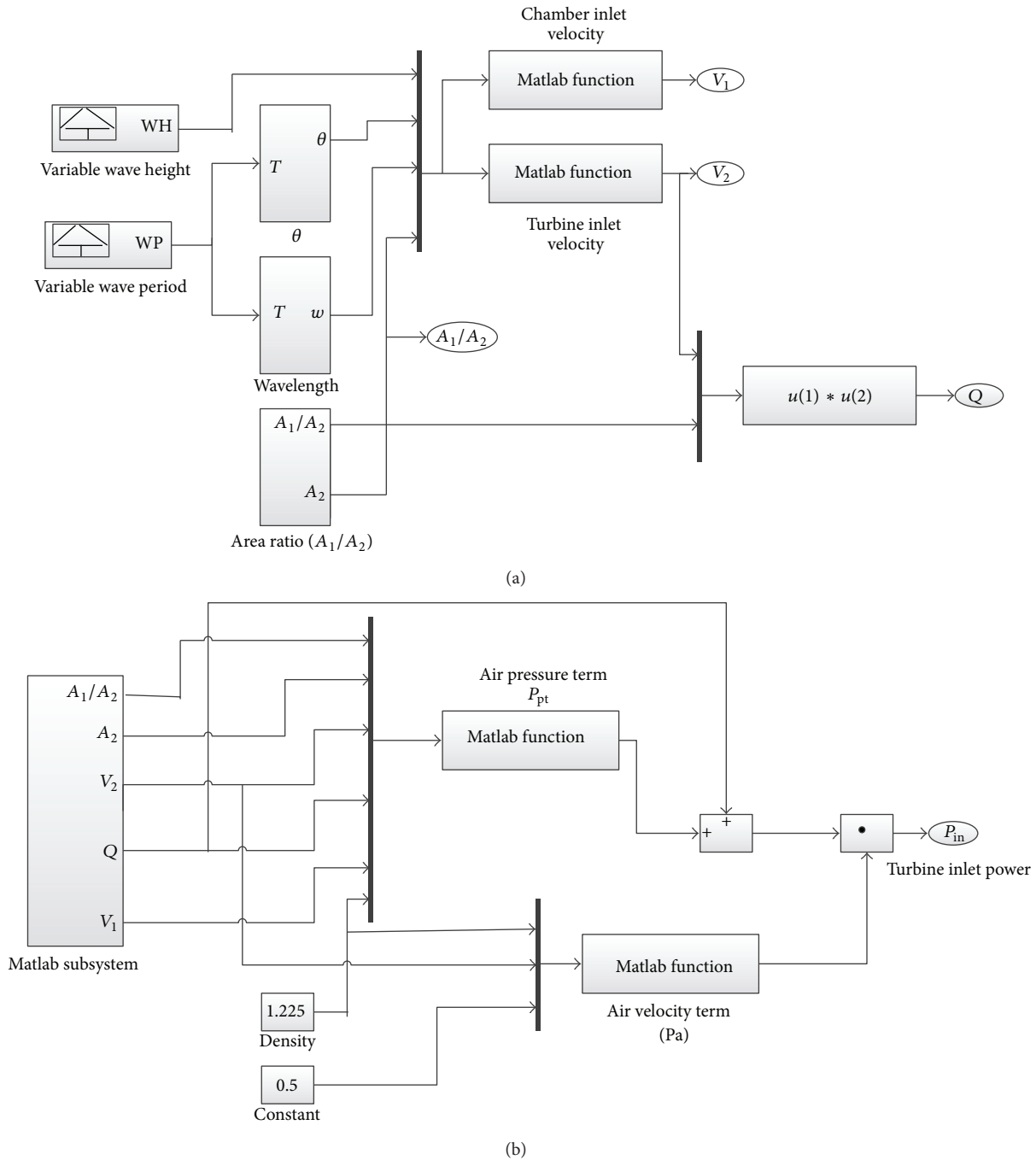


FIGURE 8: The Simulink diagram of the OWC model.

where E_0 is the no load battery voltage (V), K is the polarization voltage (V), Q is the battery capacity (Ah), A is the exponential zone amplitude (V), B is the exponential zone time constant inverse $(Ah)^{-1}$, $V_{Battery}$ is the battery voltage (V), R_{in} is the battery internal resistance (Ω), $I_{Battery}$ is the battery current (A), and $\int i dt$ is the charge supplied and drawn by the battery (Ah).

The battery model based on (14) is developed in Matlab Simulink environment and connected to a DC-DC

buck-boost bidirectional converter using controlled voltage source as shown in Figure 10.

2.4. Control of dc-Link Voltage. The circuit topology of the proposed PV-wave hybrid standalone system is shown in Figure 11. A neutral wire is placed between the capacitors connected before the VSI for feeding single-phase as well as three-phase loads to the proposed system, as shown in Figure 11.

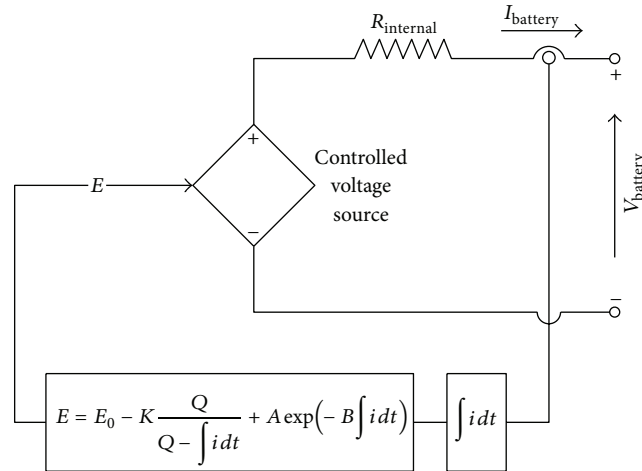


FIGURE 9: Nonlinear standard battery model [31].

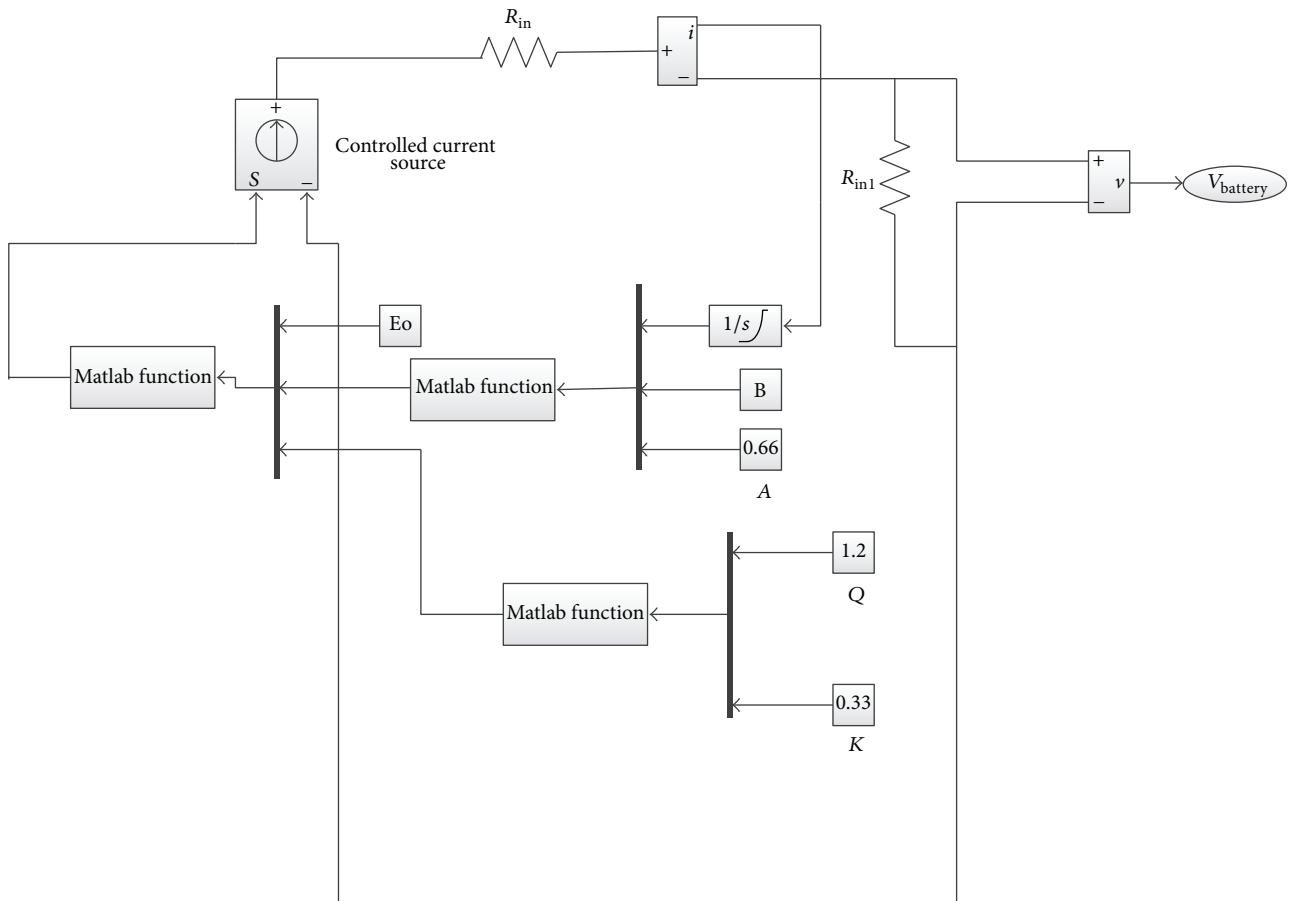


FIGURE 10: The Simulink diagram of the battery model.

In this paper, through BBDC the dc link side is connected to batteries bank; the primary objective of the control of this BBDC is to maintain constant dc-link voltage as a reference value in addition to discharge/charge current from/to batteries bank according to the required load power. The schematic

diagram of the battery bank BBDC controller is depicted in Figure 12. The voltage of the battery bank can be kept lower as compared to the reference dc-link voltage (V_{dc}^*) by using BBDC and hence fewer numbers of batteries are required to be connected in series. In the proposed standalone system,

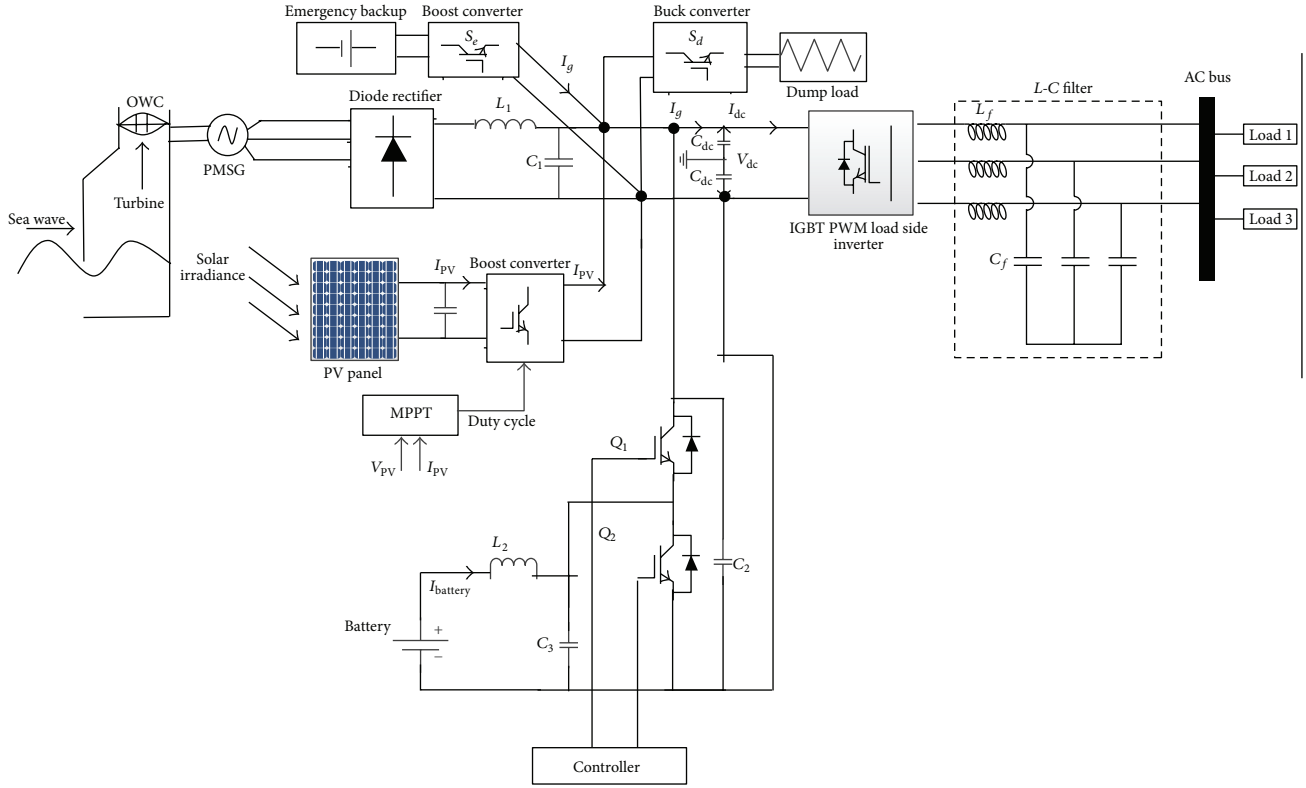


FIGURE 11: Circuit topology of the proposed PV-wave hybrid standalone system with emergency backup and dump load.

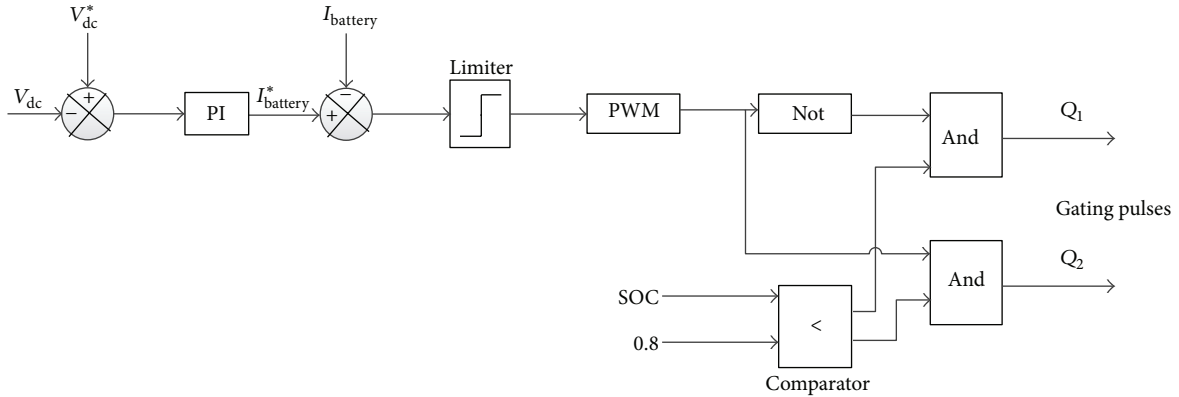


FIGURE 12: The schematic diagram of DC-DC converter controller.

the voltage of the battery bank is kept at around 300 V, whereas $V_{dc}^* = 650$ V. In this paper, the batteries bank depth of discharge is considered 60% [13] and is based on the assumption that it should provide the electric power to the loads of a 2.5 kW for approximately an hour when the generated wave power is zero. The details of the rating of the batteries bank calculation are discussed in Appendix A.

The value of the inductor used in BBDC is crucial for the conduction mode operation of it. And also the inductor existence in the batteries bank side is shown lower ripple current results which gives long lifetime and higher efficiency. Conduction mode operation also depends on input and

output current, capacitors value, and switching frequency. The value of the inductor and capacitors is as follows [32, 33]:

$$\text{Inductance } L_2 = \frac{V_{\text{Battery}} \times (V_{\text{dclink}} - V_{\text{Battery}})}{I_{\text{Battery}} \times f_s \times V_{\text{dclink}}},$$

$$\text{Buck mode capacitance } C_2 = \frac{k_L \times I_{\text{Battery}}}{8 \times f_s \times V_{\text{Battery(ripple)}}},$$

$$\text{Boost mode capacitance } C_3 = \frac{D_{\text{Boost}} \times I_{\text{dclink}}}{f_s \times V_{\text{dclink(ripple)}}},$$

(16)

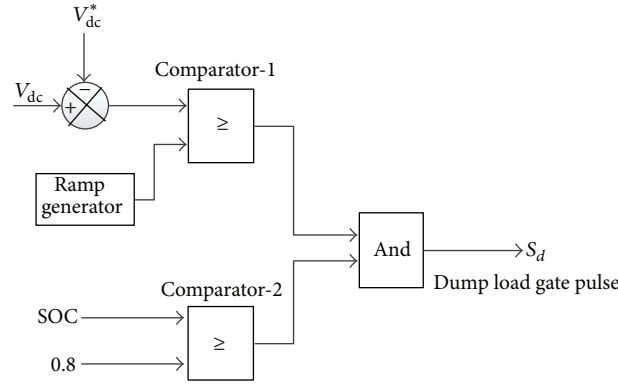


FIGURE 13: The schematic diagram of dump load controller.

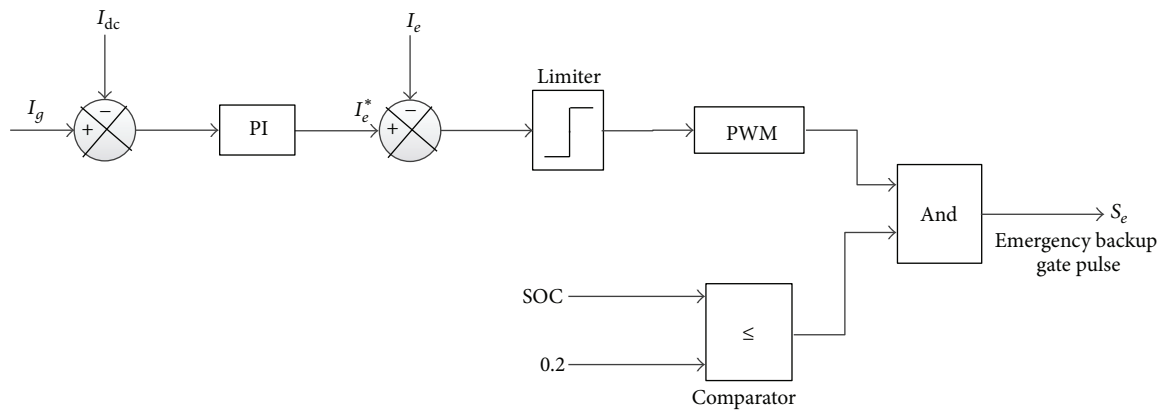


FIGURE 14: The schematic diagram of emergency backup controller.

where $V_{Battery}$ is the battery bank voltage, V_{dclink} is the dc-link voltage, I_{dclink} is the dc-link current, $I_{Battery}$ is the battery bank current, $V_{Battery(ripple)}$ is the buck side output desired ripple voltage, $V_{dclink(ripple)}$ is the boost side output desired ripple voltage, k_L is the estimated coefficient of indicator ripple current at buck side, and f_s is the switching frequency.

In this paper, the battery bank can act either as a power supply or as a sink. As a result, it should discharge/charge within specified limits when there is lack/surplus of hybrid power due to the weather condition. In this work, due to high wave and solar power condition, the surplus power at first is supplied to the battery bank until it reach its upper limit of charge carrying capacity and then additional power is absorbed by the dump load and is regulated via the chopper control shown in Figure 13. In this case, controller switching decision is made by comparing the upper limit of SOC and present status of SOC.

In case of long term when there is no PV and (/or) wave or lower PV and (/or) wave power the battery bank may not able to meet the load demand. In this case, an emergency backup is integrated with hybrid system. Control action algorithm of emergency backup is depicted in Figure 14.

Figure 15 shows a dc-link voltage control flowchart based on the above discussion for controlling the dc-link voltage, where the lower and upper limits for the battery bank SOC are kept at 0.2 and 0.8, respectively [13].

2.5. Control of Load Side VSI. At the load end, a three-phase vector control VSI is used as interface element between the consumer load and DC link voltage. The load side VSI control is responsible to control the frequency and voltage at the consumer load end. In the proposed HRES system, the output load voltages should be controlled in terms of frequency and voltage amplitude because there is no electric power grid connection. The space vector control technique is used to regulate the output voltage during the variation of required hybrid power or load power.

In this paper, the vector control technique is used based on the synchronously rotating frame described in [34, 35]. The three-phase V_a, V_b, V_c voltages and I_a, I_b, I_c currents should be transformed and measured from the reference stationary $a-b-c$ frame to the reference rotating $d-q$ frame using the preferred output load voltage electrical frequency. In this paper, the specified root-mean-square (RMS) value of the output phase voltage and the load voltage frequency are 220 V and 50 HZ, respectively.

The equations of voltage using reference rotating $d-q$ frame transformation are taken from [34, 35] as follows:

$$\begin{aligned}
 v_d &= v_{di} - L_f \frac{di_d}{dt} + L_f \omega i_q, \\
 v_q &= v_{qi} - L_f \frac{di_q}{dt} - L_f \omega i_d.
 \end{aligned}
 \tag{17}$$

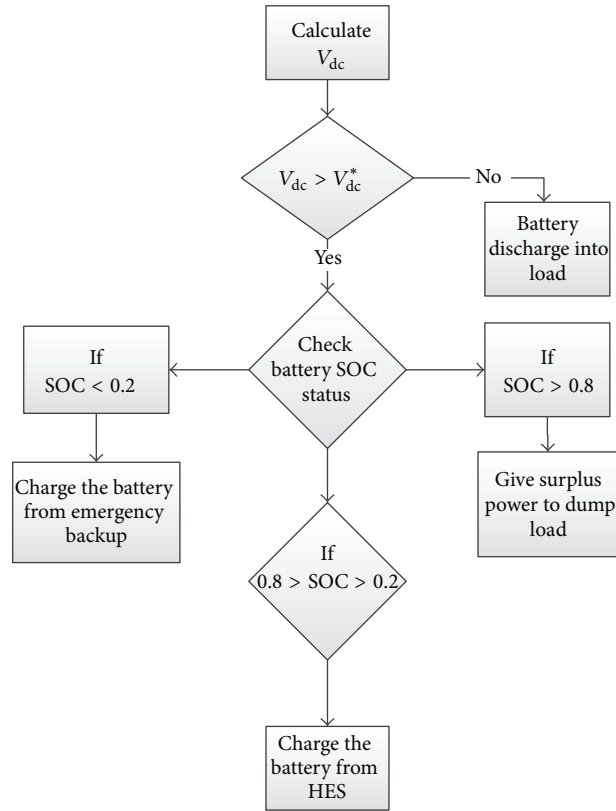


FIGURE 15: Flowchart for dc-link voltage control.

By using d - q reference rotating frame transformation, the active power and reactive power are given by

$$\text{Active power } P = \frac{3}{2} (v_d i_d + v_q i_q), \quad (18)$$

$$\text{Reactive Power } Q = \frac{3}{2} (v_d i_q - v_q i_d).$$

The active and reactive power equations will be as follows if the reference rotating frame is as $v_q = 0$ and $v_d = |V|$:

$$P = \frac{3}{2} v_d i_d = \frac{3}{2} |V| i_d, \quad (19)$$

$$Q = \frac{3}{2} v_d i_q = \frac{3}{2} |V| i_q.$$

Therefore, the active and reactive power can be controlled by controlling direct and quadrature current elements, respectively. Also, for resistive load, case V_d^* can be directed by

$$V_d^* = \sqrt{2} V_{\text{RMS}}^*, \quad (20)$$

where V_{RMS}^* is the output RMS phase voltage reference value. In this control technique, the load output current in the internal control loops and the load output voltages in the external control loops are regulated by PI controllers. All the PI controllers used in this paper are tuned by using Ziegler-Nichols tuning method [36]. The control technique of the VSI is used in load side as shown in Figure 16.

Based on the inverter switching frequency, the high frequency unwanted harmonics will generate in output ac voltage by the load side VSI which ultimately creates power quality problem in the customer end. In this controller, space vector PWM (SV-PWM) method is used because it slightly reduces the system harmonics contents in the output voltage. In addition, it raises the fundamental load output voltage. A simple passive L - C filter is used in load side end to eliminate the high frequency unwanted harmonics for preventing the power quality problem occurring in the customer end. The design of the passive L - C filter [37] is given in Appendix B and the values are

$$\begin{aligned} L_f &= 0.052 \text{ H}, \\ C_f &= 2 \mu\text{F}. \end{aligned} \quad (21)$$

3. Site Selection

Malaysia is situated between 1° and 7° in the North Latitude and 100° and 120° in the East Longitude. But Malaysia is vastly surrounded by water and it has the 29th longest coastline in the world. It has a total coastline of 4,675 kilometers and 878 islands [38, 39], so Malaysia has a massive potential of wave energy that may be a vital source of electrical energy generation especially for the coast and the island communities. Among those islands, Perhentian Island (shown in Figure 17) is one of the most popular resort islands in Malaysia situated in the northeastern coast of

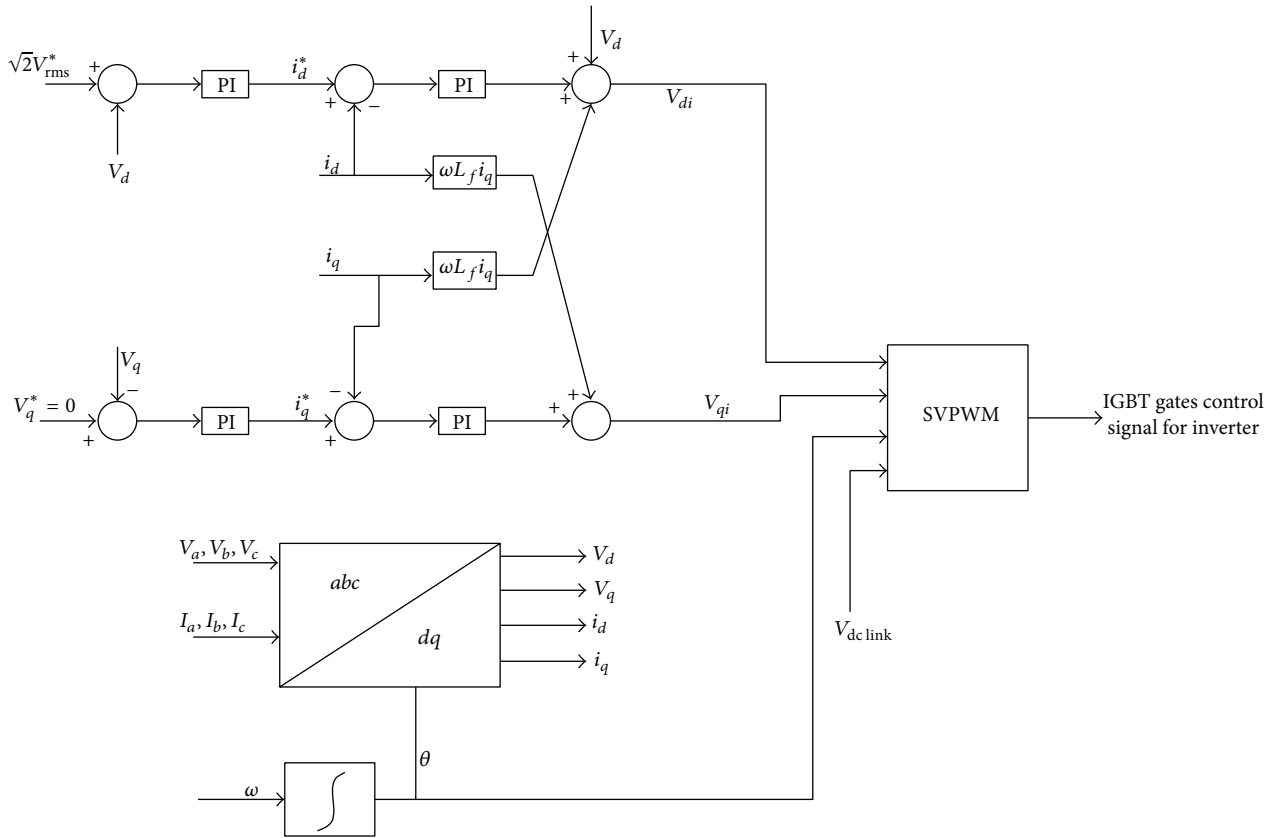


FIGURE 16: The load side three-phase VSI controller.



FIGURE 17: Location of target site (Perhentian Island) (modified from [45]).

Western Malaysia. It is approximately 20 km from the coast of Terengganu. In this island, the majority of the buildings are resorts and only one village where the local people live. Diesel generators are used as the main sources for electricity generation in this island. In 2007 [40], Universiti Kebangsaan Malaysia and National Energy Policies (NEP) installed a wind-solar hybrid energy system in this island, although till now it was not connected to the electrical network because of lower wind power. The winds are rare in this area.

Perhentian Island has uniform climate characteristics and it has abundant rainfall and temperature with high humidity.

Since it is located in the equatorial doldrums area, it has naturally great sunshine and solar radiation. But it is quite difficult to have a fully sunny day with completely clear sky. Perhentian Island receives daily average 5.5 hours of the sunshine. The solar data of Perhentian Island is as shown in Figure 18.

Solar energy cannot meet the consumer load demand at each instant because of its daily limited sunshine hours. So to build HRES in this island, wave energy can be considered one of the efficient power generation sources. The wave data of Perhentian Island is illustrated in Figure 19, where the peak

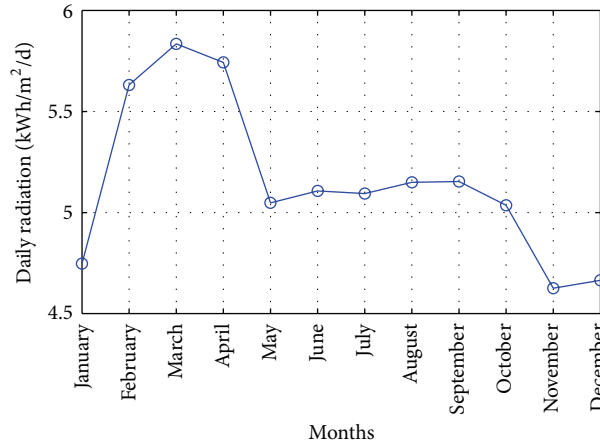


FIGURE 18: Annually solar irradiation.

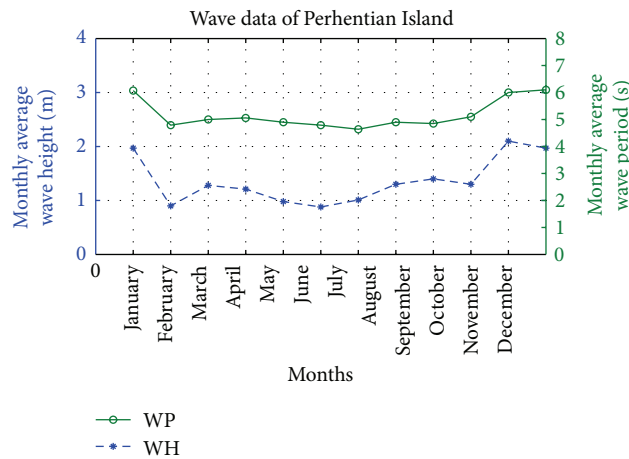


FIGURE 19: Monthly average WH/WP data of a year for Perhentian Island.

average wave height (WH) and wave period (WP) occur from November to January. Both solar and wave data are obtained by Malaysian Meteorological Department Labuan (MMDL) from 2005 to 2012. In addition, wave data is analyzed by the “hindcast” technique [41]. MMDL collected wave data by using Acoustic Doppler Current Profiler (ADCP) equipment and Voluntary Observation Ship (VOS) scheme.

At this site, the maximum average WH measured in the month of November was 2.1m and the minimum in the month of June was 0.88 m. On the other hand, the maximum average WP measured in the month of December was 6.1s and the minimum in the month of July was 4.64 s. Based on the wave theory and equations in [1, 29], wave power level during the whole year is shown in Figure 20 and is mainly depending on WH and WP.

It could be found from [1] that Malaysian sea has an average of 8.5 kW/m wave power level. But, from Figure 20, it could be seen that Perhentian Island has an average of 15.9 kW/m wave power level. So Perhentian Island site is identified as economically viable for commercial scale wave power generation in Malaysia, because any site in the world

is able to produce wave power at competitive prices if it has an average wave power level equal or above 15 kW/m. In addition, these sites are considered to have exceptionally high-energy resources than other renewable energy sources like wind. The main aim of the propose hybrid system in this paper is to establish a commercial scale PV-wave hybrid power plant in the Perhentian Island by eliminating the intermittent power generation nature of both PV and wave energy sources.

4. Simulation Result and Discussion

The simulation model of the proposed standalone PV-wave hybrid system with energy storage is built in Matlab Simulink environment under different operating conditions. PMSG is modeled in Matlab Simulink from the literature [42, 43] and the parameters are taken from [44] which are presented in Appendix C. In addition, the parameters used for PV array, OWC design, and Darrieus turbine are also mentioned in Appendix C. In this section, the average solar irradiation of January, February, and March months and the average wave

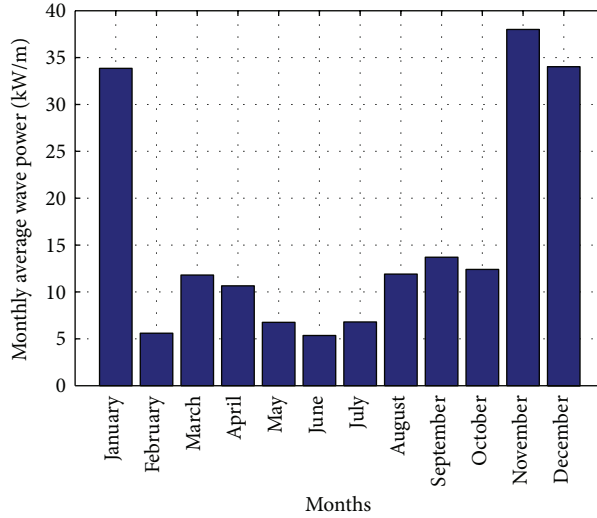


FIGURE 20: Average wave power level of a year for Perhentian Island.

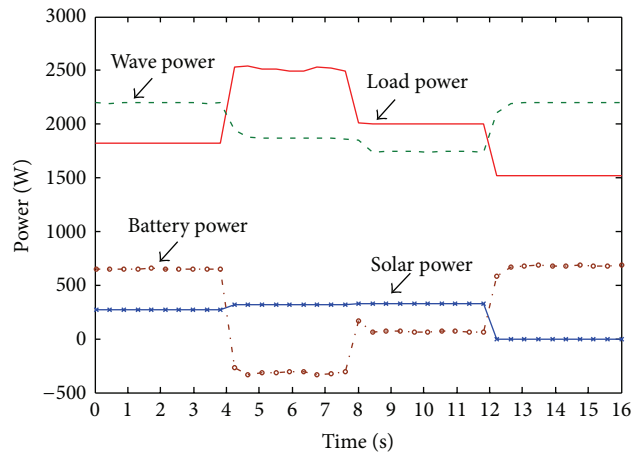


FIGURE 21: PV-wave hybrid system powers distribution.

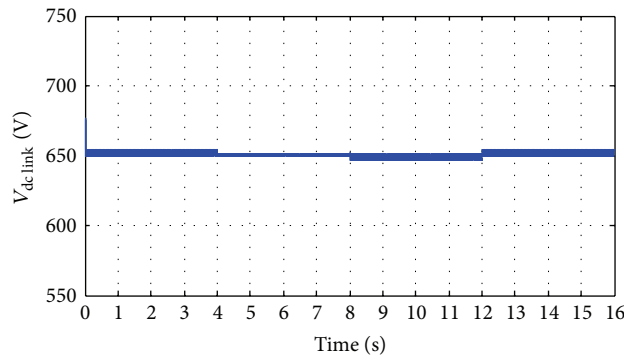


FIGURE 22: Dc-link voltage.

height and wave period of February, March, and June months from Section 3 are used to observe the performance of the proposed system under the variable load condition.

The performance of buck-boost DC-DC bidirectional converter controller is presented in Figures 21 and 22.

Figure 21 shows the power distribution curve of generated solar power, wave power, load power, and battery bank power. From Figure 21 it is seen that during the solar power, wave power, and required load variation, power from the battery bank changes (discharge/charge) to maintain the power

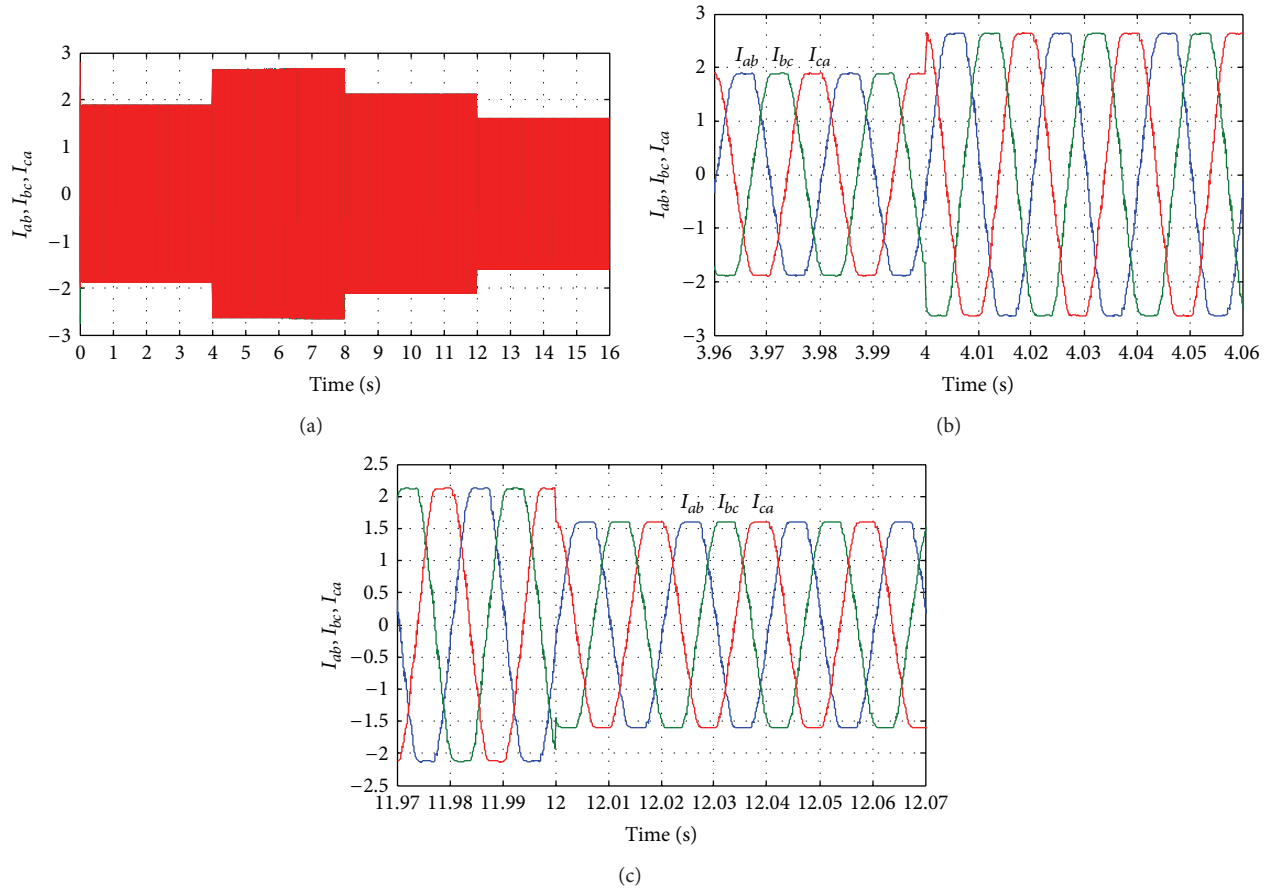


FIGURE 23: Output line current response with change in required load power. (a) Output line currents throughout the full simulation time; (b) output line current when the load increases at simulation time from 3.96 s to 4.06 s; (c) output line current when the load decreases at simulation time from 11.97 s to 12.07 s.

stability of the system. So it could be clear from Figure 21 that, when the generated hybrid power is more than the required load power, the controller is able to charge the battery bank, and when the required load power is more than generated hybrid power then controller is able to discharge the battery bank. Further, it can also establish the constant dc-link voltage at 650 V when there is a change in hybrid power and load demand, as shown in Figure 22. The absence of solar power after 12-second in Figure 21 indicate that cloudy or night period. In this case, wave power and battery bank power satisfactorily meet the load demand at each instant. So it can be established that the performance of the buck-boost DC-DC bidirectional converter controller is quite satisfactory in both transient and steady-state hybrid power and load demand condition.

The output load current response during the long time simulation is shown in Figure 23(a). Figures 23(b) and 23(c) show the output load current when the load power increases at simulation time from 3.96 s to 4.06 s and when the load power decreases at simulation time from 11.97 s to 12.07 s, respectively. The output voltage response for whole simulation time and the output voltage response when load increases and decreases are shown in Figures 24(a)–24(c),

respectively. Figure 24 shows the output RMS phase voltage (for phase a V_a) where it is maintained 220 V as reference value. In Figures 26(a) and 26(b), it is seen that the total harmonic distortion (THD) in the output ac line voltage is about 1.8% and similarly the THD in the output ac line current is about 1.5% in all the three phases. The modulation indexes are shown in Figure 27 for all the three phases.

From Figures 24, 25, 26, and 27, it can be clear that a suitable quality of voltage and current can be delivered to the load with the help of SV-PWM control inverter switching and a passive L - C filter. Finally, it is ascertained that the proposed hybrid system can successfully accommodate solar irradiation, WH, WP, and load changes, and the control system can efficiently track the change of hybrid power generation and load demand.

5. Conclusion

In this paper, a novel standalone PV-wave hybrid system with appropriate energy flow controllers is designed and modeled for island users where the electric power grid is not available. The power generated by PV sources is highly dependent on environmental conditions. To overcome this intermittent

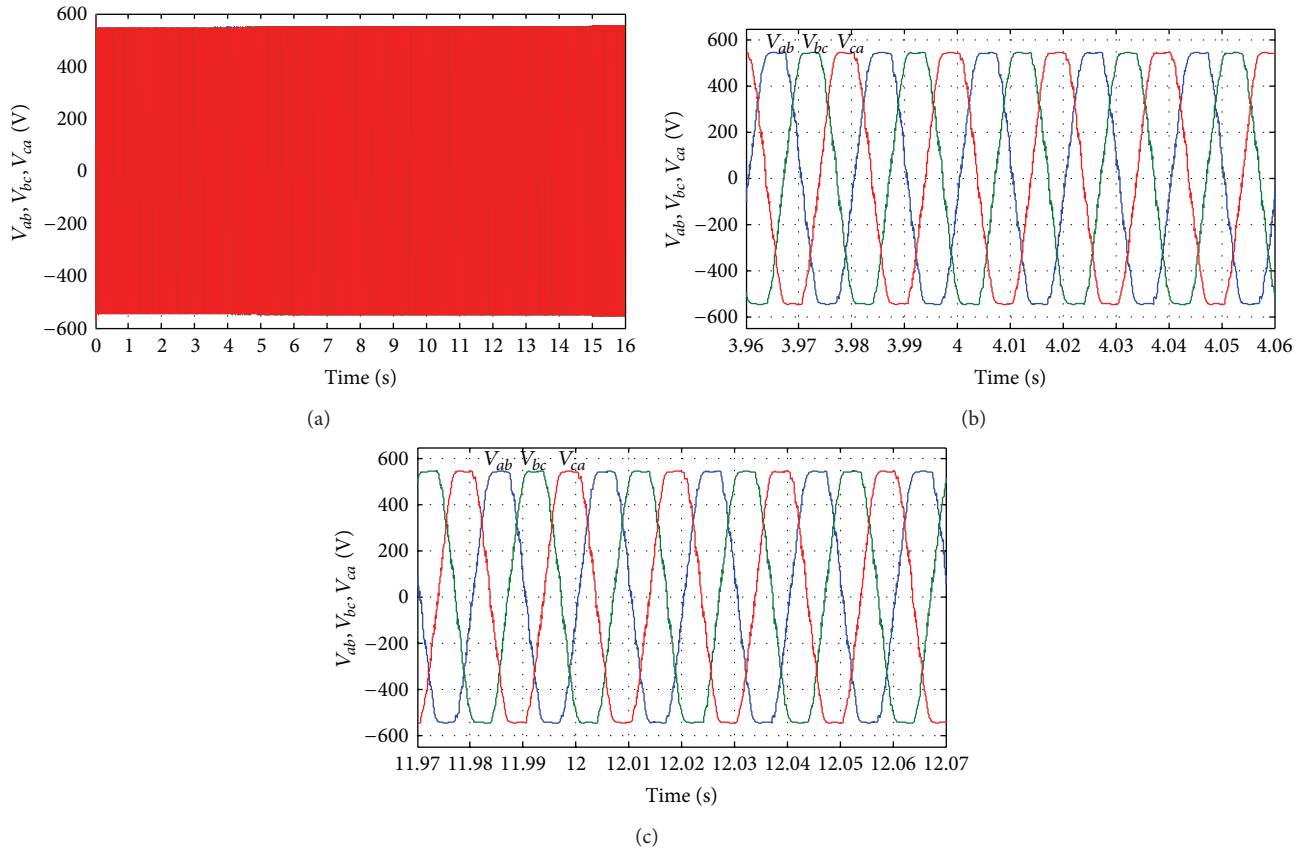


FIGURE 24: Output line voltage response with change in required load power. (a) Output line voltages throughout the full simulation time; (b) output line voltage when the load increases at simulation time from 3.96 s to 4.06 s; (c) output line voltage when the load decreases at simulation time from 11.97 s to 12.07 s.

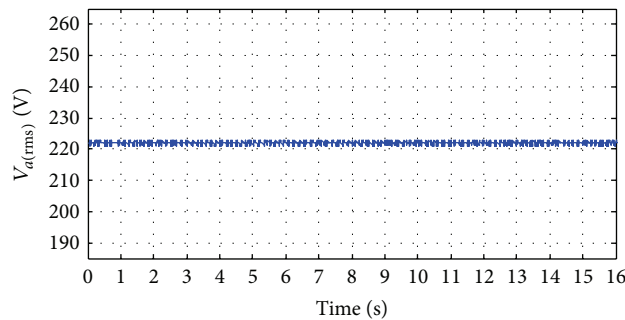


FIGURE 25: The output RMS phase voltage.

power generation nature of PV system, in this paper, PV system integrated with the wave energy converter device and battery bank, because wave energy is easily predictable and consistent than other green energy sources such as wind. The hybrid PV-wave topology with broad analysis and Matlab Simulink simulation results is presented in this paper. It has been seen from the simulation results that the controller can maintain the dc-link voltage at constant value in spite of variation in generated hybrid power and required load power. Furthermore, the controller is developed in such a way that the battery bank has been able to accumulate the

excess power generated by hybrid system and supply it to the system load during the hybrid power shortage by controlling BBDC. This controller not only maintains the constant dc-link voltage, but also acts as a dc-link side active filter and reduces the generator torque oscillation of OWC PMSG during the variation in load. Finally, it has been explained how the space vector controls three-phase VSI controller to control the load side output voltage in terms of frequency and voltage amplitude to the resistive load. The THD in voltage and current at load side is about 1.7% and 1.55%, respectively, which illustrates the good quality of voltage and current

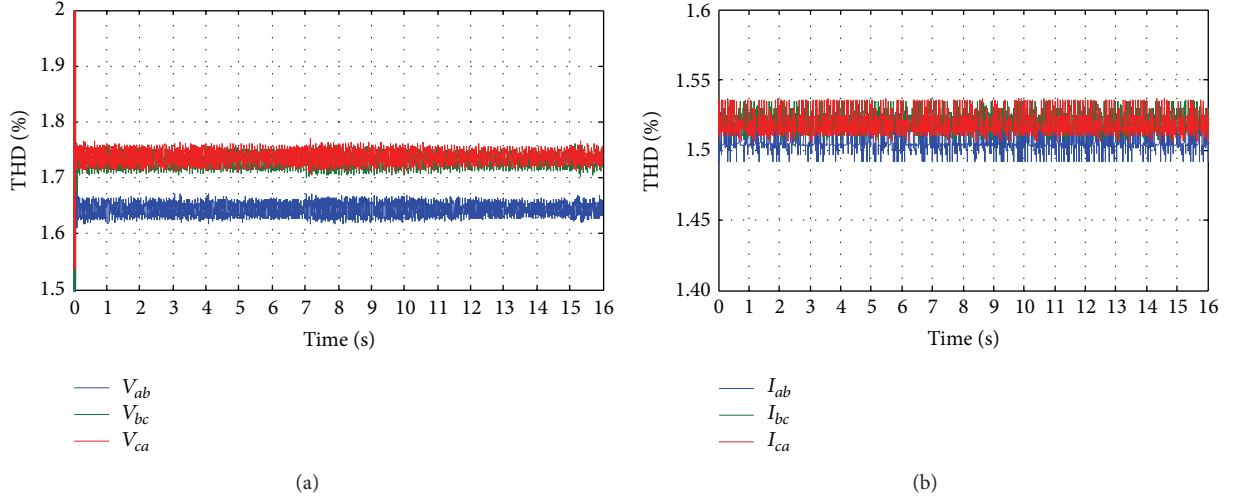


FIGURE 26: The total harmonic distortion throughout the whole simulation time. (a) THD of line voltage; (b) THD of line current.

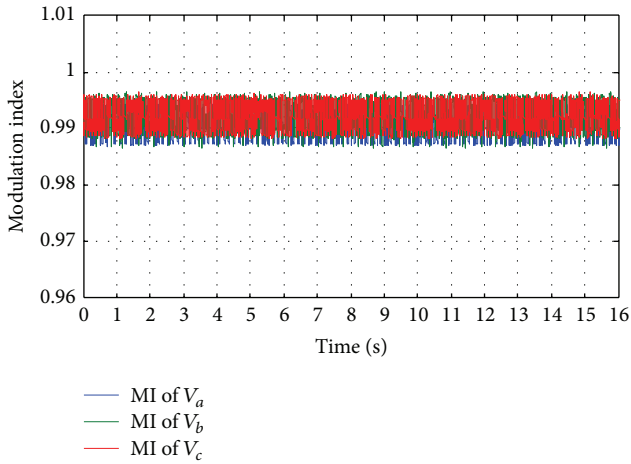


FIGURE 27: Modulation indexes for all three phases.

generated at the consumer side end. The simulation results show that the performance of the proposed hybrid system is satisfactory under the steady-state power as well as transient solar, wave, and load power conditions. This study can be considered as the initial part of building prototype standalone PV-wave hybrid system. The future work will aim to set up a standalone PV-wave hybrid system in the University of Malaya laboratory to verify the simulations results with experiment.

Appendices

A.

The battery bank rating calculation is

$$\text{Battery rating} = \frac{2.5 \text{ kW} \times 1 \text{ hr}}{300 \text{ V} \times 0.6} = 13.89 \text{ Ahr.} \quad (\text{A.1})$$

TABLE 1: Parameters of PMSG.

Number of poles	4
Rated power	3 kW
Rated speed	241 rad/s
Per phase stator resistance (R)	0.4578 Ω
d -axis and q -axis stator inductance (L_d & L_q)	0.00334 H
Magnetic flux induced in the stator windings (ψ)	0.171 Wb
Rated torque	14.2 Nm

Hence, 12-V, 14-Ahr battery rating is considered and, consequently, 25 numbers of batteries are required to connect in series.

B.

The equations [13, 37] related to passive L - C filter design are

$$K = \left[\frac{k^2 - 15/4k^4 + 64/5\pi k^5 - 5/4k^6}{1440} \right]^{1/2}$$

$$L_f = \frac{V_0}{I_0 f_{sw}} \left\{ K \frac{V_{dlink}}{V_{0,av}} \left[1 + 4\pi^2 \left(\frac{f}{f_{sw}} \right)^2 K \frac{V_{dlink}}{V_{0,av}} \right] \right\}^{1/2}$$

$$C_f = \frac{V_{dlink}}{L_f f_{sw}^2 V_{0,av}}, \quad (\text{B.1})$$

where k (modulation index) = 1, V_0 (Load Voltage) = 220 V, I_0 (Load Current) = 4.58 A, f (fundamental frequency) = 50 HZ, f_{sw} (switching frequency) = 2 kHz, $V_{0,av}$ (total harmonic load voltage) = 5% of V_0 , L_f is the inductance of filter, and C_f is the capacitance of filter.

C.

See Tables 1, 2, 3, and 4.

TABLE 2: Parameters of OWC.

OWC chamber length (L_{ch})	1.5 m		
Water surface area inside the chamber (A_1)	1.4 m ²		
Turbine inlet area (A_2)	0.012 m ²		
Water depth (d)			
WH (m)	0.98	0.9	0.88
WP (s)	4.9	4.79	4.79
d (m)	16.47	15.75	15.73

TABLE 3: Parameters of Darrieus turbine.

Swept area by balde (A)	0.012 m ²
Air density	1.22 Kg/m ³
Height of the rotor (H_t)	240 mm
Diameter of the rotor (D_t)	100 mm

TABLE 4: Parameters of PV array.

Maximum rated power (P_{max})	87 W
Maximum voltage (V_{max})	17.4 V
Maximum current (I_{max})	5.02 A
Open circuit voltage (V_{oc})	21.7 V
Short circuit voltage (I_{sc})	5.34 A
Number of modules required	5

D.

Using the literature [23, 25, 27, 29, 30], expression for the power due to the air pressure term can be obtained. This power term is derived in [23, 25] but present here for completeness. According to the above literature, it is clear that the power available at the wave turbine consists of two terms: air velocity term P_a and air pressure term P_{pt} . The power P_{pt} mainly depends on the volume of air flow rate Q across the turbine and the pressure gradient. So power due to the air pressure term can be define as [23]

$$P_{pt} = (p_2 - p_0) \times Q, \quad (D.1)$$

where, from the continuity equation,

$$Q = A_1 \times V_1 = V_2 \times A_2. \quad (D.2)$$

The exhausted pressure p_0 is assumed to be constant and ambient, even close to the turbine. The upstream inner pressure p_2 near the turbine is related to the pressure within the air chamber by the Bernoulli energy equation:

$$p_2 = p_1 + 0.5 \times \rho \times (V_1^2 - V_2^2) + \rho \frac{\delta}{\delta t} (\varphi_1 - \varphi_2), \quad (D.3)$$

where the velocity potentials φ_1 and φ_2 are approximated by

$$\begin{aligned} \varphi_1 &\approx V_1 \eta_1, \\ \varphi_2 &\approx V_2 \eta_2. \end{aligned} \quad (D.4)$$

Based on the linear momentum equation theory, the pressure difference in (D.1) can be derived as

$$p_2 - p_0 \approx \rho \frac{A_1}{A_2} \frac{\delta \varphi_1}{\delta t} + \rho \frac{Q}{A_2} (V_2 - V_1). \quad (D.5)$$

From (D.1) and (D.5),

$$P_{pt} = \left[\rho \frac{A_1}{A_2} \frac{\delta \varphi_1}{\delta t} + \rho \frac{Q}{A_2} (V_2 - V_1) \right] \times Q. \quad (D.6)$$

But the rate of change of velocity potentials φ_1 is

$$\frac{\delta \varphi_1}{\delta t} = -\frac{H_{in}^2}{\theta^2} \omega^2 \{2 \cos(\omega t)^2 - 1\} \times \sin^2\left(\frac{\theta}{2}\right). \quad (D.7)$$

Hence, power due to the air pressure term is

$$\begin{aligned} P_{pt} = & \left[-\frac{A_1}{A_2} \frac{H_{in}^2}{\theta^2} \omega^2 \{2 \cos(\omega t)^2 - 1\} \right. \\ & \left. \times \sin^2\left(\frac{\theta}{2}\right) + \frac{Q}{A_2} (V_2 - V_1) \right] \times Q \times \rho. \end{aligned} \quad (D.8)$$

Conflict of Interests

The authors declare that there is no conflict of interests regarding the publication of this paper.

Acknowledgments

The authors would like to thank KeTTTHA, Ministry of Energy, Green Technology and Water, and Postgraduate Research Grant, University of Malaya, for providing financial support under the Research Grant “Active Control and Efficiency Optimization of Turbine Blades for Oscillating Water Column Device.”

References

- [1] N. H. Samrat, N. Ahmad, I. A. Choudhury, and Z. Taha, “Prospect of wave energy in Malaysia,” in *Proceedings of the IEEE 8th International Power Engineering and Optimization Conference*, 2014.
- [2] D. Amorndechaphon, S. Premrudeepreechacharn, K. Higuchi, and X. Roboam, “Modified grid-connected CSI for hybrid PV/wind power generation system,” *International Journal of Photoenergy*, vol. 2012, Article ID 381016, 12 pages, 2012.
- [3] L. Zhang, D. Jing, L. Zhao, J. Wei, and L. Guo, “Concentrating PV/T hybrid system for simultaneous electricity and usable heat generation: a review,” *International Journal of Photoenergy*, vol. 2012, Article ID 869753, 8 pages, 2012.
- [4] C.-L. Shen and S.-H. Yang, “Multi-input converter with MPPT feature for wind-PV power generation system,” *International Journal of Photoenergy*, vol. 2013, Article ID 129254, 13 pages, 2013.
- [5] K. Agbossou, M. Kolhe, J. Hamelin, and T. K. Bose, “Performance of a stand-alone renewable energy system based on energy storage as hydrogen,” *IEEE Transactions on Energy Conversion*, vol. 19, no. 3, pp. 633–640, 2004.
- [6] O. C. Onar, M. Uzunoglu, and M. S. Alam, “Modeling, control and simulation of an autonomous wind turbine/photovoltaic/fuel cell/ultra-capacitor hybrid power system,” *Journal of Power Sources*, vol. 185, no. 2, pp. 1273–1283, 2008.
- [7] M. Uzunoglu, O. C. Onar, and M. S. Alam, “Modeling, control and simulation of a PV/FC/UC based hybrid power generation system for stand-alone applications,” *Renewable Energy*, vol. 34, no. 3, pp. 509–520, 2009.

- [8] J. R. Halliday and D. G. Dorrell, "Review of wave energy resource and wave generator developments in the UK and the rest of the world," in *Proceedings of the 4th LASTED International Conference on Power and Energy Systems*, pp. 76–83, June 2004.
- [9] Z. Chen, H. Yu, M. Hu, G. Meng, and C. Wen, "A review of offshore wave energy extraction system," *Advances in Mechanical Engineering*, vol. 2013, Article ID 623020, 9 pages, 2013.
- [10] S. Diaconu and E. Rusu, "The environmental impact of a wave dragon array operating in the Black Sea," *The Scientific World Journal*, vol. 2013, Article ID 498013, 20 pages, 2013.
- [11] M. E. McCormick, *Ocean Wave Energy Conversion*, Dover, New York, NY, USA, 2007.
- [12] R.-S. Tseng, R.-H. Wu, and C.-C. Huang, "Model study of a shoreline wave-power system," *Ocean Engineering*, vol. 27, no. 8, pp. 801–821, 2000.
- [13] C. N. Bhende, S. Mishra, and S. G. Malla, "Permanent magnet synchronous generator-based standalone wind energy supply system," *IEEE Transactions on Sustainable Energy*, vol. 2, no. 4, pp. 361–373, 2011.
- [14] F. Ding, P. Li, B. Huang, F. Gao, C. Ding, and C. Wang, "Modeling and simulation of grid-connected hybrid photovoltaic/battery distributed generation system," in *Proceedings of the China International Conference on Electricity Distribution (CICED '10)*, September 2010.
- [15] H. Lund, "Large-scale integration of optimal combinations of PV, wind and wave power into the electricity supply," *Renewable Energy*, vol. 31, no. 4, pp. 503–515, 2006.
- [16] H. De Battista, R. J. Mantz, and F. Garelli, "Power conditioning for a wind-hydrogen energy system," *Journal of Power Sources*, vol. 155, no. 2, pp. 478–486, 2006.
- [17] S. S. Deshmukh and R. F. Boehm, "Review of modeling details related to renewably powered hydrogen systems," *Renewable and Sustainable Energy Reviews*, vol. 12, no. 9, pp. 2301–2330, 2008.
- [18] H. Mahamudul, M. Saad, and M. I. Henk, "Photovoltaic system modeling with fuzzy logic based maximum power point tracking algorithm," *International Journal of Photoenergy*, vol. 2013, Article ID 762946, 10 pages, 2013.
- [19] N. Pandiarajan, R. Ramaprabha, and R. Muthu, "Application of circuit model for photovoltaic energy conversion system," *International Journal of Photoenergy*, vol. 2012, Article ID 410401, 14 pages, 2012.
- [20] C. Koukouvaos, D. Kandris, and M. Samarakou, "Computer-aided modelling and analysis of PV systems: a comparative study," *The Scientific World Journal*, vol. 2014, Article ID 101056, 17 pages, 2014.
- [21] H.-T. Yau, C.-J. Lin, and Q.-C. Liang, "PSO based PI controller design for a solar charger system," *The Scientific World Journal*, vol. 2013, Article ID 815280, 13 pages, 2013.
- [22] V. Salas, E. Olías, A. Barrado, and A. Lázaro, "Review of the maximum power point tracking algorithms for stand-alone photovoltaic systems," *Solar Energy Materials and Solar Cells*, vol. 90, no. 11, pp. 1555–1578, 2006.
- [23] M. F. Hsieh, I. H. Lin, D. G. Dorrell, M. J. Hsieh, and C. C. Lin, "Development of a wave energy converter using a two chamber oscillating water column," *IEEE Transactions on Sustainable Energy*, vol. 3, no. 3, pp. 482–497, 2012.
- [24] M. Folley and T. J. Whittaker, "Identification of non-linear flow characteristics of the LIMPET shoreline OWC," in *Proceedings of the 12th International Offshore and Polar Engineering Conference*, pp. 541–546, May 2002.
- [25] D. G. Dorrell, M.-F. Hsieh, and C.-C. Lin, "A small segmented oscillating water column using a Savonius rotor turbine," *IEEE Transactions on Industry Applications*, vol. 46, no. 5, pp. 2080–2088, 2010.
- [26] J. Falnes, *Ocean Waves and Oscillating Systems*, Cambridge University Press, Cambridge, UK, 2002.
- [27] D. G. Dorrell, M.-F. Hsieh, and C.-C. Lin, "A multichamber oscillating water column using cascaded savonius turbines," *IEEE Transactions on Industry Applications*, vol. 46, no. 6, pp. 2372–2380, 2010.
- [28] I. G. Morrison and C. A. Greated, "Oscillating water column modeling," in *Proceedings of the 23rd International Conference on Coastal Engineering*, pp. 502–511, October 1992.
- [29] D. G. Dorrell and W. Fillet, "Investigation of a small scale segmented oscillating water column utilizing savonius rotor turbine," in *Proceedings of the International Conference on Energy and Environment*, 2006.
- [30] P. Boccotti, *Wave Mechanics for Ocean Engineering*, Elsevier Oceanography Series, Amsterdam, The Netherlands, 2000.
- [31] O. Tremblay, L.-A. Dessaint, and A.-I. Dekkiche, "A generic battery model for the dynamic simulation of hybrid electric vehicles," in *Proceedings of the IEEE Vehicle Power and Propulsion Conference (VPPC '07)*, pp. 284–289, September 2007.
- [32] M. O. Haruni, *A stand-alone hybrid power system with energy storage [Ph.D. thesis]*, University of Tasmania, Sandy Bay, Australia, 2013.
- [33] M. Green, *Design Calculations For Buck-Boost Converters*, Texas Instruments, Dallas, Tex, USA, 2012.
- [34] M. E. Haque, M. Negnevitsky, and K. M. Muttaqi, "A novel control strategy for a variable-speed wind turbine with a permanent-magnet synchronous generator," *IEEE Transactions on Industry Applications*, vol. 46, no. 1, pp. 331–339, 2010.
- [35] M. E. Haque, K. M. Muttaqi, and M. Negnevitsky, "Control of a stand alone variable speed wind turbine with a permanent magnet synchronous generator," in *Proceedings of the IEEE Power and Energy Society General Meeting—Conversion and Delivery of Electrical Energy in the 21st Century*, July 2008.
- [36] K. J. Astrom and T. Hagglund, *PID Controllers: Theory, Design and Tuning*, Instrument Society of America, Research Triangle Park, NC, USA, 1995.
- [37] P. A. Dahono, A. Purwadi, and A. Qamaruzzaman, "LC filter design method for single-phase PWM inverters," in *Proceedings of the International Conference on Power Electronics and Drive Systems*, pp. 571–576, February 1995.
- [38] Geography of Malaysia, 2013, http://en.wikipedia.org/wiki/Geography_of_Malaysia.
- [39] List of islands of Malaysia, 2013, http://en.wikipedia.org/wiki/List_of_islands_of_Malaysia.
- [40] Z. M. Darus, N. A. Hashim, S. N. A. Manan, M. A. A. Rahman, K. N. A. Maulud, and O. A. Karim, "Potential of wind energy in sustainable development of resort island in Malaysia: a case study of Pulau Perhentian (Perhentian island)," in *Proceedings of the 10th WSEAS International Conference on Mathematical Methods, Computational Techniques and Intelligent Systems*, 2008.
- [41] R. G. Quayle and M. J. Changery, "Estimates of coastal deepwater wave energy potential for the world," in *Proceedings of the Oceans '81*, 1981.
- [42] D. Grenier, L.-A. Dessaint, O. Akhrif, Y. Bonnassieux, and B. LePioufle, "Experimental nonlinear torque control of a permanent-magnet synchronous motor using saliency," *IEEE*

Transactions on Industrial Electronics, vol. 44, no. 5, pp. 680–687, 1997.

- [43] P. C. Krause, O. Wasynczuk, and S. D. Sudhoff, *Analysis of Electrical Machinery and Drive System*, IEEE Press, Piscataway, NJ, USA, 2002.
- [44] L. Barote, R. Weissbach, R. Teodorescu, C. Marinescu, and M. Cirstea, “Stand-alone wind system with vanadium redox battery energy storage,” in *Proceedings of the 11th International Conference on Optimization of Electrical and Electronic Equipment (OPTIM '08)*, pp. 407–412, May 2008.
- [45] Perhentian Island, Malaysia, 2013, <http://www.turtlebaydivers.com/DiveLocation.htm>.

Research Article

Synthesis of CdIn₂S₄ Microsphere and Its Photocatalytic Activity for Azo Dye Degradation

Jianhui Huang,¹ Wei Lin,² and Jianqin Chen¹

¹ College of Environmental & Biological Engineering, Putian University, Putian 35110, China

² Department of General Surgery, Affiliated Hospital of Putian University, Putian 351100, China

Correspondence should be addressed to Jianhui Huang; owenhuang95@163.com

Received 20 February 2014; Accepted 20 March 2014; Published 30 March 2014

Academic Editors: J. Shi and H. Zhou

Copyright © 2014 Jianhui Huang et al. This is an open access article distributed under the Creative Commons Attribution License, which permits unrestricted use, distribution, and reproduction in any medium, provided the original work is properly cited.

CdIn₂S₄ was prepared by ultrasonic spray pyrolysis. The prepared CdIn₂S₄ was characterized by X-ray diffraction (XRD), field emission scanning electron microscopy (FSEM), transmission electron microscopy (TEM), UV-visible diffuse reflectance spectroscopy (UV-Vis DRS), and N₂-sorption techniques. Aqueous photocatalytic activity was evaluated by the decomposition of methyl orange under visible light irradiation. The results indicate that the prepared CdIn₂S₄ has spherical morphology with mesoporous structure which can efficiently degrade methyl orange in water. The sample prepared at 500°C exhibits the optimized photocatalytic activity.

1. Introduction

Azo dyes, a large class of synthetic organic dyes that contain nitrogen as the azo group -N=N- as part of their molecular structures. More than half the commercial dyes belong to this class which have been widely used in many industries such as the production of textiles, paint, ink, and cosmetics [1]. The effluent from azo dyes industries contains substantial amounts of such dyes and their breakdown products, which causes coloration of water and poses a threat to aquatic life [2–4], mutagenic/carcinogenic [5], and genotoxic [6]. Therefore dyes effluent poses a great threat to the environment and increasing attention has been paid to the treatment of dye effluent. While due to the complex aromatic structure and stability of these dyes, conventional biological treatment processes are ineffective for their degradation [7]. The absorption and coagulation processes are only able to absorb them up to some extent, but the sludge produced from both processes becomes more difficult to be disposal [8].

In the past several decades, semiconductor-mediated photocatalytic oxidation has been proved to be a promising technology for the treatment of water containing azo dyes [9]. Among a variety of semiconductor materials, the titanium dioxide (TiO₂) photocatalysts have been most extensively

investigated and used because of their physical properties and economic advantages, such as high redox power, photostability, chemical inertness, and cheapness [10]. However, TiO₂ can only absorb a very small ultraviolet part (3–4%) of solar light because of its wide band gap (3.2 eV for anatase) which constrains the extensive applications of TiO₂. Thus, considerable efforts have been devoted to develop new visible responded photocatalyst which is still a significant issue in both academic and practical applications.

Among various new photocatalysts, multinary chalcogenide semiconductors have attracted great attention because of the instability of the mono- and binary chalcogenide compounds [11–14]. Cadmium indium sulphide (CdIn₂S₄) belonging to ternary semiconductors of chalcogenide AB₂X₄ and being considered to have potential applications in optical devices, solar cells [15] and photocatalysts for H₂ evolution, bacterial inactivation, and organic pollutant elimination [16–18]. Considering the advantages of nanostructures over the bulk materials, attempts have been made to synthesize CdIn₂S₄ with variety of nanostructures. Up to now, the nanostructural CdIn₂S₄ has been synthesized by methods like hydrothermal [15, 19], microwave [20], and sol-gel [21] with template. In most cases, these techniques require high temperature or high pressure to obtain crystalline material. In

addition, the removal of the templates requires additional processing steps that can be costly and wasteful. Thus, a high-yield synthetic and template-free method for the CdIn_2S_4 preparation can undoubtedly benefit the design of high-performance materials in catalytic applications. Recently, ultrasonic spray pyrolysis technique (USP) is particularly attractive. It is fast, inexpensive, vacuumless, and suitable for mass production [22–24]. In the previous work, we have demonstrated that the USP method is a common method to prepare multinary sulfide [25].

In present work, the CdIn_2S_4 microspheres were synthesized using USP process. The effect of reaction conditions on the prepared CdIn_2S_4 was studied. The obtained microspherical CdIn_2S_4 was used as photocatalyst to oxidize azo dyes in aqueous solution.

2. Experimental Section

2.1. Catalysts Preparation. All of the reagents were of analytical grade and used without further purification. The CdIn_2S_4 photocatalyst was prepared by a USP method. In a typical synthesis, 0.532 g $\text{Cd}(\text{AC})_2 \cdot 2(\text{H}_2\text{O})$, 1.2 g $\text{InCl}_3(\text{H}_2\text{O})_4$, and 0.76 g $\text{CH}_4\text{N}_2\text{S}$ were added into 150 mL water under magnetic stirring to form a transparent solution. The solution was nebulized at $1.7 \text{ MHz} \pm 10\%$ (YUYUE402AI, Shanghai) and then carried by air with a flow rate 10 L/min through a quartz tube surrounded by a furnace thermostated at $500\sim 700^\circ\text{C}$. The quartz reaction tube with the diameter of 3.5 cm was 1 m long. The products were collected in a percolator with distilled water, separated by centrifugation, and washed thoroughly with ethanol and distilled water. The product was finally dried in an oven at 60°C for overnight.

2.2. Characterization. Powder X-ray diffraction (XRD) patterns were collected in θ - θ mode using a Bruker D8 Advance X-ray diffractometer (Cu $\text{K}\alpha 1$ irradiation, $\lambda = 1.5406 \text{ \AA}$). The morphology of the sample was investigated by field emission scanning electron microscopy (FSEM) (JSM-6700F). Transmission electron microscopy (TEM) was recorded on a FEI Tecnai 20 microscope. Carbon-coated copper grid was used as the sample holder. The sample was suspended in ethanol solution, followed by sonication for 30 min in the ultrasonic bath. Drops of the suspensions were applied on a copper grid coated with carbon. Nitrogen sorption experiments were carried out at 77 K by using Micromeritics ASAP 2020 equipment. All the samples were degassed at 140°C and 10^{-6} torr for 6 h prior to the measurement. The UV-visible diffuse reflectance spectra were performed on a Varian Cary 500 spectrometer with an integrating sphere attachment ranging from 200 nm to 800 nm. BaSO_4 was used as a reference sample in these measurements.

2.3. Evaluation of Photocatalytic Activity. The photocatalytic activities of the samples were evaluated by the decomposition of methyl orange (MO) a typical azo dye in aqueous solution. Catalyst (0.05 g) was suspended in a 100 mL Pyrex glass vessel containing MO with a concentration of 25 ppm. The visible light source was a 300 W halogen lamp (Philips Electronics)

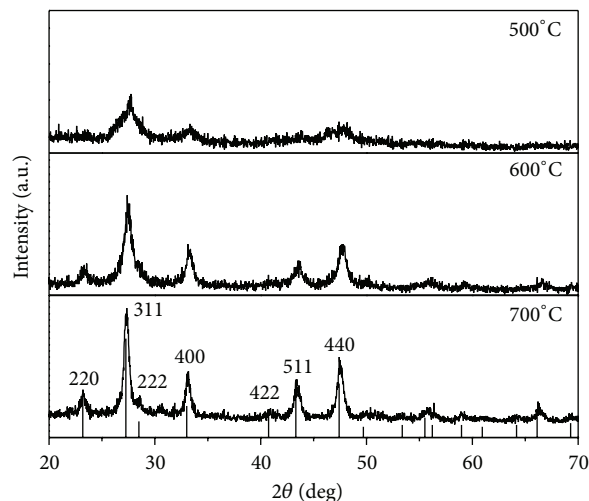


FIGURE 1: XRD patterns of CdIn_2S_4 prepared at different temperatures.

positioned beside a cylindrical reaction vessel with a flat side. The system was water-cooled to maintain the temperature. A 400 nm cutoff filter was placed in front of the vessel to ensure irradiation by visible light. The suspension was stirred in darkness for 1 h to achieve adsorption equilibrium and the reactor was irradiated to induce photocatalyzed decomposition reactions. At given irradiation time intervals, 3 mL of the reaction suspension was collected and centrifuged to remove the catalyst. The degraded solution was analyzed using a Varian Cary 50 Scan UV-Vis spectrophotometer.

3. Results and Discussion

3.1. Crystal Structure. The X-ray diffraction (XRD) patterns of the resultant products synthesized from USP process at different temperature are shown in Figure 1. The XRD patterns of the sample prepared at 700°C can be indexed to cubic CdIn_2S_4 well consistent with the reported data (JCPDS number 27-60, space group: $\text{Fd}\bar{3}m$). The peaks at 2θ values of 23.18, 27.25, 28.48, 33.00, 40.74, 43.31, and 47.40 match well with the (220), (311), (222), (400), (422), (511), and (440) crystal planes of CdIn_2S_4 , respectively. There is no any trace of impurity phase such as CdS , In_2S_3 under the instrument resolution, indicating the high purity of the sample. Furthermore, the intensity of the peaks according to CdIn_2S_4 is affected by the preparation temperature. The XRD pattern for the sample prepared at 500°C shows broad noisy peaks means the semi-crystalline nature of the sample. The intensity of peaks is increasing with the increasing of temperature. This suggests that the crystalline of CdIn_2S_4 increases with the increase of temperature. The calculated average crystal sizes of the samples prepared at 500, 600, and 700°C using the Scherrer equation are 5.4, 8.4, and 14.2 nm, respectively.

3.2. Morphology. Figure 2 depicts the FSEM images of prepared samples. Figure 2(a) is the low-magnification image of

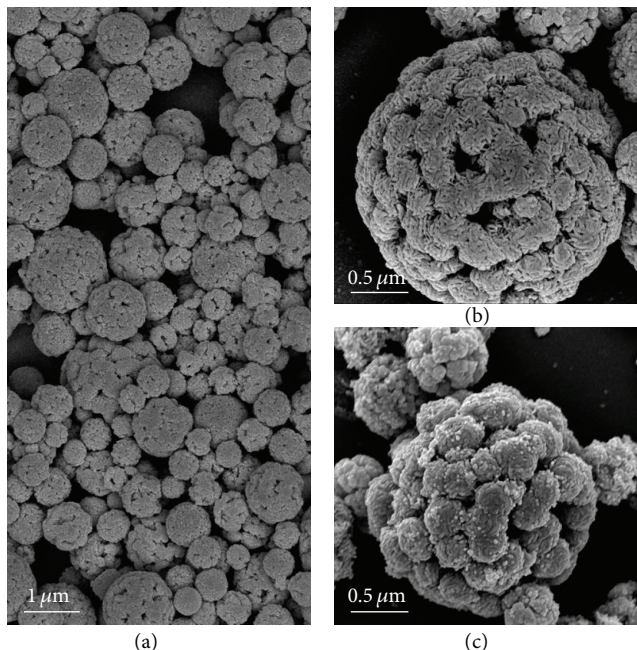


FIGURE 2: The FSEM images of CdIn₂S₄ prepared by ultrasonic spray pyrolysis. (a) and (b) 500°C, (c) 700°C.

the sample prepared at 500°C which indicates that the as-prepared samples consist entirely of spheres with a range of 100 nm to 1.5 μm. The ultrasonic nebulizer during the preparation is the key to form the spherical morphology. The aerosol produced from nebulizer consisted of numerous small liquid droplets which contained the precursor. These droplets would serve as microreactors and yield one spherical particle per droplet. The size of droplet and concentration of precursor determines the product dimension [26]. When these droplets are carried into the tubular reactor with air, the water in the droplet is heated and evaporating. At the same time, the thiourea in the droplet would decompose quickly and release H₂S which would react with the metal precursor quickly and generate submicrospherical CdIn₂S₄. The excess H₂S from thiourea will be absorbed by the water in the percolator which will not be released out of system. Figure 2(b) is the magnified surface morphologies of samples prepared at 500°C which shows the porous structure of sample. The porous structure will not be destroyed even prepared at high temperature of 700°C (see Figure 2(c)). The result also shows that the sample prepared at 500°C has a crude surface compared with the sample prepared at 700°C. This can be due to the larger catalyst particles for the sample prepared under higher temperature.

The TEM image of CdIn₂S₄ sphere in Figure 3 confirms that the prepared spheres are composed of small nanoparticles and have porous structure. The porous structure will endow the CdIn₂S₄ with more active points and larger light-harvesting ability which will benefit its photocatalytic performance. The composition of CdIn₂S₄ sphere was determined by energy dispersive X-ray spectroscopy (EDX) in the “A” position of Figure 3. The results of EDX analysis (Figure 4) imply that the as-prepared samples contain In, Cd, S, and a

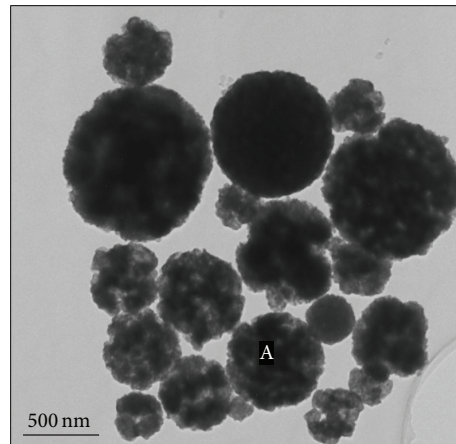


FIGURE 3: The TEM images of CdIn₂S₄ prepared at 500°C.

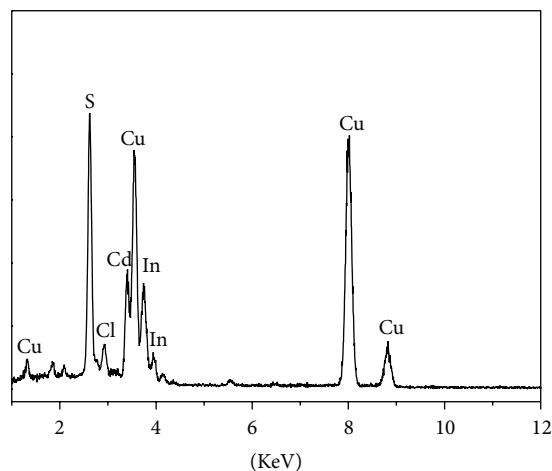


FIGURE 4: Energy-dispersive X-ray analysis spectra of CdIn₂S₄ prepared at 500°C.

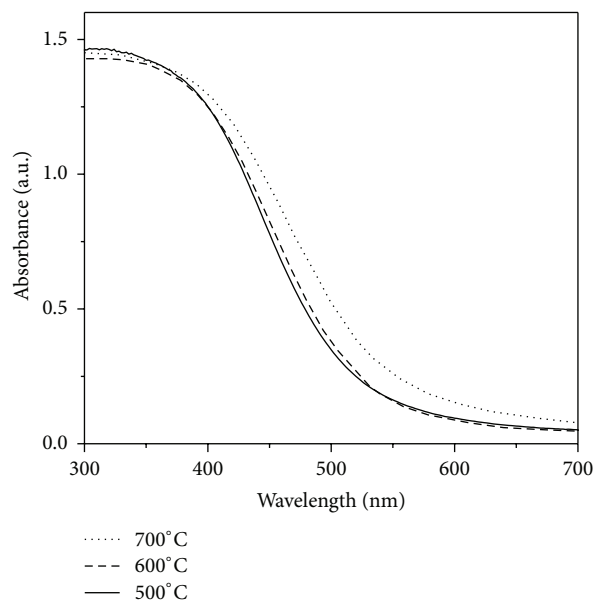


FIGURE 5: Diffuse reflectance UV-Vis spectra of CdIn₂S₄ prepared at different temperature.

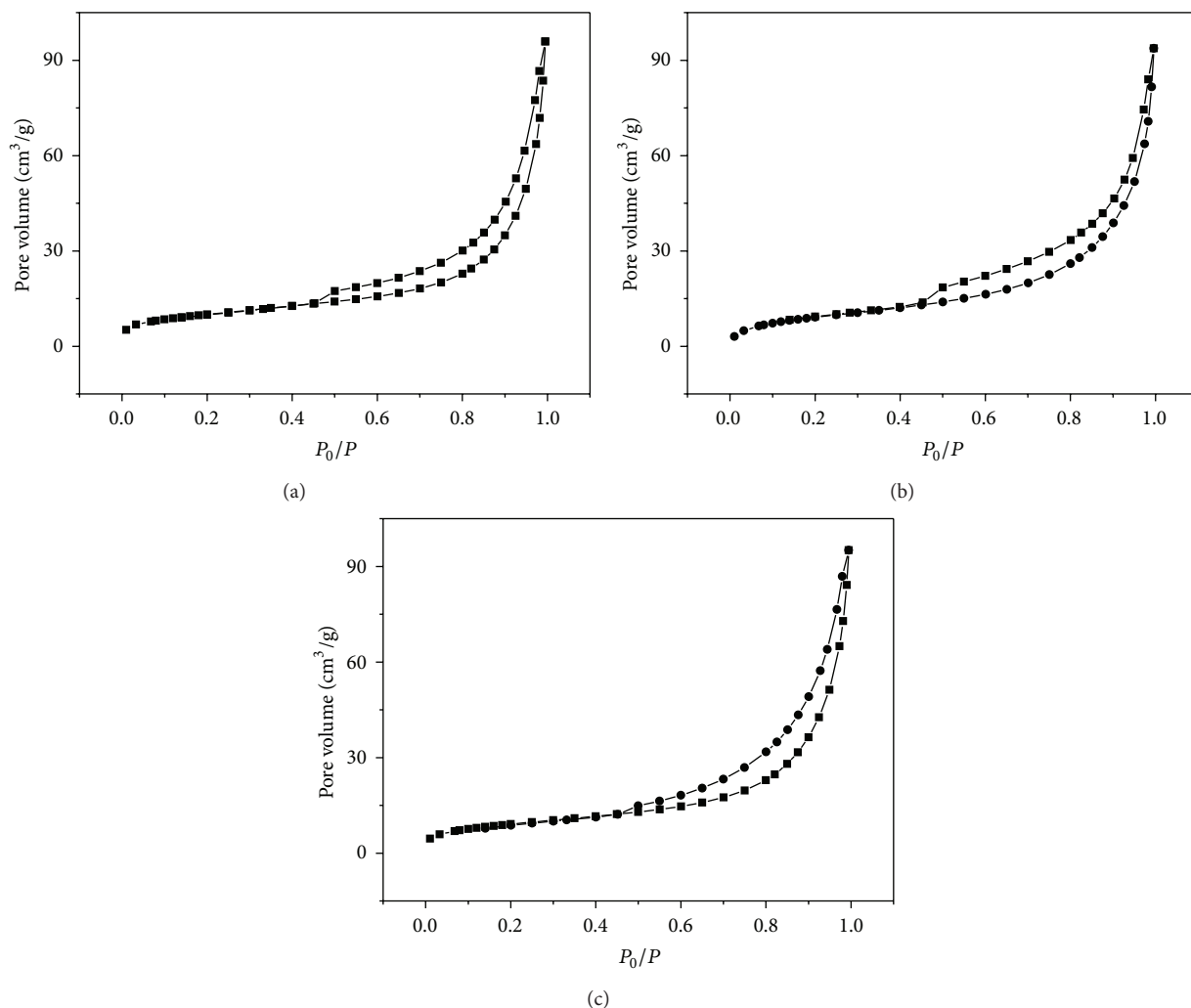


FIGURE 6: N_2 adsorption-desorption isothermal curves of $CdIn_2S_4$ prepared at different temperatures (a) $500^\circ C$, (b) $600^\circ C$, and (c) $700^\circ C$.

small amount of Cl element. The ratio of In to Cd in the microspheres is 1.95 which is very close to the atom ratio in $CdIn_2S_4$. The small amount Cl element is from the precursor of $InCl_3(H_2O)_4$ which is not completely removed during the washing of product.

3.3. Optical Properties. Figure 5 shows the light absorption properties of prepared samples. All the samples show remarkable absorption in the visible light region. Besides, the basic adsorption edge of the $CdIn_2S_4$ is shifted to shorter wavelength with the decreasing of temperature in preparation. The absorption edges of $CdIn_2S_4$ prepared at 500, 600, and $700^\circ C$ are 522, 528, and 541 nm corresponding to a band gap of 2.38, 2.35, and 2.29 eV, respectively. The blue shifts of adsorption edge are due to the quantum confinement effect, which is attributed to the smaller crystal size of $CdIn_2S_4$ prepared in low temperature.

3.4. Specific Surface Area and Pore Structure. Figure 6 shows the nitrogen adsorption-desorption isotherms of the $CdIn_2S_4$

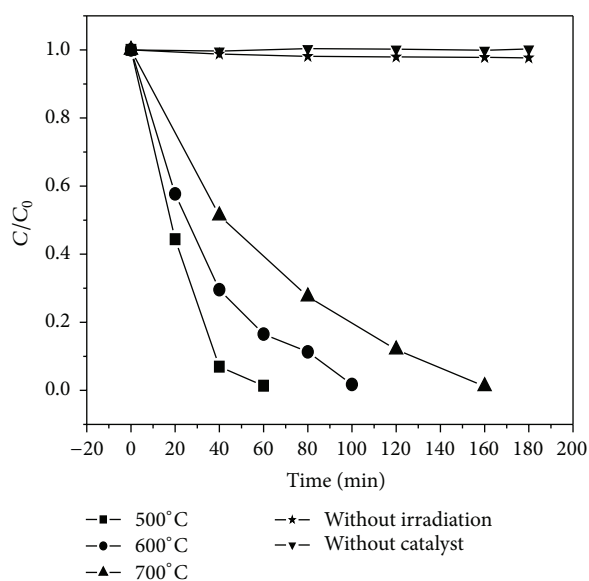
prepared at different temperature. All the samples show similar type-IV isotherms, which are representative of mesoporous solids. In addition, the surface area, pore size, and pore volume (see Table 1) have no significant difference for the samples prepared in the different temperature. This indicates that the mesoporous structures was not destroyed or did not shrink in the high temperature which is consistent with the result of SEM in Figure 2.

3.5. Photocatalytic Activity. Figure 7 shows the photocatalytic degradation of methyl orange (MO) on $CdIn_2S_4$ microspheres with otherwise identical conditions under visible-light irradiation ($\lambda > 400$ nm) after the adsorption-desorption equilibrium was reached. The control test (without catalyst) under visible light irradiation showed that the photolysis of MO was negligible. The dark control experiment with $CdIn_2S_4$ prepared at $500^\circ C$ alone reveals that the concentration of MO was also unchanged after 3 hours, which demonstrates that the adsorption/desorption equilibrium had been obtained after 1 hour in dark and the $CdIn_2S_4$ microspheres would not react with MO. The MO was

TABLE 1: Crystalline and porous properties of CdIn₂S₄ prepared at different temperatures.

Temperature (°C)	d^a (nm)	Pore size ^b (nm)	Surface area ^c (m ² g ⁻¹)	Pore volume ^d (cm ³ g ⁻¹)
500	5.4	13.5	36.1	0.15
600	8.4	13.5	34.5	0.15
700	14.2	13.6	33.5	0.15

^a d values of the samples estimated by Scherrer formula; ^bBJH pore sizes determined from the nitrogen desorption branches; ^cBET surface areas determined from the nitrogen adsorption and desorption isotherm measurement; ^dpore volumes is the BJH desorption cumulative pore volume of pores.

FIGURE 7: Photocatalytic activity of the CdIn₂S₄ sphere samples.

degraded quickly in the presence of CdIn₂S₄ under visible light irradiation and indicates the high photocatalytic activity of CdIn₂S₄ microspheres. The test also shows that the activities of doped samples were greatly influenced by the prepared temperature. The complete degradation of methyl orange for samples prepared at 500, 600, and 700°C needs 60, 100, and 160 min, respectively. Considering the similar surface area and pore structure among different samples, the higher photocatalytic activity for the sample prepared at 500°C can be due to the small crystal size which is of benefit to the separation of excited electron/hole pair during photocatalytic reaction.

4. Conclusions

The CdIn₂S₄ have been synthesized by using ultrasonic spray pyrolysis process without using any template. The prepared samples have spherical morphology with mesoporous structure whose products can be generated continuously at a rate of several grams per hour. The prepared CdIn₂S₄ exhibited excellent photocatalytic activity. We expect that these CdIn₂S₄ spheres prepared with this method will have immense importance in other regions such as solar cells, LED, and optoelectronics.

Conflict of Interests

The authors declare that there is no conflict of interests regarding the publication of this paper.

Acknowledgments

This work was supported by the National Natural Science Foundation of China (21103095), the Excellent Young Scientific Research Talents in University of Fujian, China (JA12285), the Education and Scientific Project for the Young and Middle Aged Teachers of Fujian, China (JA13279), and Scientific Project of Putian Science and Technology Bureau (2013S03(3)).

References

- [1] C. Sahoo, A. K. Gupta, and A. Pal, "Photocatalytic degradation of Methyl Red dye in aqueous solutions under UV irradiation using Ag⁺ doped TiO₂," *Desalination*, vol. 181, no. 1-3, pp. 91-100, 2005.
- [2] C. Wang, A. Yediler, D. Lienert, Z. Wang, and A. Kettrup, "Toxicity evaluation of reactive dyestuffs, auxiliaries and selected effluents in textile finishing industry to luminescent bacteria *Vibrio fischeri*," *Chemosphere*, vol. 46, no. 2, pp. 339-344, 2002.
- [3] A. A. Essawy, A. E.-H. Ali, and M. S. A. Abdel-Mottaleb, "Application of novel copolymer-TiO₂ membranes for some textile dyes adsorptive removal from aqueous solution and photocatalytic decolorization," *Journal of Hazardous Materials*, vol. 157, no. 2-3, pp. 547-552, 2008.
- [4] C. Wang, A. Yediler, D. Lienert, Z. Wang, and A. Kettrup, "Ozonation of an azo dye C.I. Remazol Black 5 and toxicological assessment of its oxidation products," *Chemosphere*, vol. 52, no. 7, pp. 1225-1232, 2003.
- [5] K. T. Chung and S. E. J. Stevens, "Degradation azo dyes by environmental microorganisms and helminths," *Environmental Toxicology and Chemistry*, vol. 12, no. 11, pp. 2121-2132, 1993.
- [6] A. Gottlieb, C. Shaw, A. Smith, A. Wheatley, and S. Forsythe, "The toxicity of textile reactive azo dyes after hydrolysis and decolourisation," *Journal of Biotechnology*, vol. 101, no. 1, pp. 49-56, 2003.
- [7] E. Razo-Flores, M. Luijten, B. Donlon, G. Lettinga, and J. Field, "Biodegradation of selected azo dyes under methanogenic conditions," *Water Science and Technology*, vol. 36, no. 6-7, pp. 65-72, 1997.
- [8] R. Ganesh, G. D. Boardman, and D. Michelsen, "Fate of azo dyes in sludges," *Water Research*, vol. 28, no. 6, pp. 1367-1376, 1994.
- [9] J. Huang, K. Ding, Y. Hou, X. Wang, and X. Fu, "Synthesis and photocatalytic activity of Zn₂GeO₄ nanorods for the degradation of organic pollutants in water," *ChemSusChem*, vol. 1, no. 12, pp. 1011-1019, 2008.

- [10] C. S. Turchi and D. F. Ollis, "Photocatalytic degradation of organic water contaminants: mechanisms involving hydroxyl radical attack," *Journal of Catalysis*, vol. 122, no. 1, pp. 178–192, 1990.
- [11] Q. Guo, G. M. Ford, H. W. Hillhouse, and R. Agrawal, "Sulfide nanocrystal inks for dense $\text{Cu}(\text{In}_{1-x}\text{Ga}_x)(\text{S}_{1-y}\text{Se}_y)_2$ absorber films and their photovoltaic performance," *Nano Letters*, vol. 9, no. 8, pp. 3060–3065, 2009.
- [12] X. Zhang, Y. Du, Z. Zhou, and L. Guo, "A simplified method for synthesis of band-structure-controlled $(\text{CuIn})_x\text{Zn}_{2(1-x)}\text{S}_2$ solid solution photocatalysts with high activity of photocatalytic H_2 evolution under visible-light irradiation," *International Journal of Hydrogen Energy*, vol. 35, no. 8, pp. 3313–3321, 2010.
- [13] I. Tsuji, Y. Shimodaira, H. Kato, H. Kobayashi, and A. Kudo, "Novel stannite-type complex sulfide photocatalysts $\text{A}_2^I\text{-Zn-A}^{\text{IV}}\text{-S}_4$ ($\text{A}^I = \text{Cu}$ and Ag ; $\text{A}^{\text{IV}} = \text{Sn}$ and Ge) for hydrogen evolution under visible-light irradiation," *Chemistry of Materials*, vol. 22, no. 4, pp. 1402–1409, 2010.
- [14] Y. Li, G. Chen, C. Zhou, and J. Sun, "A simple template-free synthesis of nanoporous $\text{ZnS-In}_2\text{S}_3\text{-Ag}_2\text{S}$ solid solutions for highly efficient photocatalytic H_2 evolution under visible light," *Chemical Communications*, no. 15, pp. 2020–2022, 2009.
- [15] L. Fan and R. Guo, "Fabrication of novel CdIn_2S_4 hollow spheres via a facile hydrothermal process," *Journal of Physical Chemistry C*, vol. 112, no. 29, pp. 10700–10706, 2008.
- [16] B. B. Kale, J.-O. Baeg, S. M. Lee, H. Chang, S.-J. Moon, and C. W. Lee, " CdIn_2S_4 nanotubes and "marigold" nanostructures: a visible-light photocatalyst," *Advanced Functional Materials*, vol. 16, no. 10, pp. 1349–1354, 2006.
- [17] W. J. Wang, T. W. Ng, W. K. Ho et al., " CdIn_2S_4 microsphere as an efficient visible-light-driven photocatalyst for bacterial inactivation: synthesis, characterizations and photocatalytic inactivation mechanisms," *Applied Catalysis B: Environmental*, vol. 129, pp. 482–490, 2013.
- [18] A. Bhirud, N. Chaudhari, L. Nikam et al., "Surfactant tunable hierarchical nanostructures of CdIn_2S_4 and their photohydrogen production under solar light," *International Journal of Hydrogen Energy*, vol. 36, no. 18, pp. 11628–11639, 2011.
- [19] W. L. Jiang, X. H. Yin, F. Xin, Y. D. Bi, Y. Liu, and X. Li, "Preparation of CdIn_2S_4 microspheres and application for photocatalytic reduction of carbon dioxide," *Applied Surface Science*, vol. 288, pp. 138–142, 2014.
- [20] S. K. Apte, S. N. Garaje, R. D. Bolade et al., "Hierarchical nanostructures of CdIn_2S_4 via hydrothermal and microwave methods: efficient solar-light-driven photocatalysts," *Journal of Materials Chemistry*, vol. 20, no. 29, pp. 6095–6102, 2010.
- [21] J. M. Thornton and D. Raftery, "Hydrogen evolution by templated cadmium indate nanoparticles under natural sunlight illumination," *International Journal of Hydrogen Energy*, vol. 38, no. 19, pp. 7741–7749, 2013.
- [22] Z. Ai, L. Zhang, and S. Lee, "Efficient visible light photocatalytic oxidation of NO on aerosol flow-synthesized nanocrystalline InVO_4 hollow microspheres," *Journal of Physical Chemistry C*, vol. 114, no. 43, pp. 18594–18600, 2010.
- [23] Y. Huang, Z. H. Ai, W. K. Ho, M. J. Chen, and S. C. Lee, "Ultrasonic spray pyrolysis synthesis of porous Bi_2WO_6 microspheres and their visible-light-induced photocatalytic removal of NO," *Journal of Physical Chemistry C*, vol. 114, no. 14, pp. 6342–6349, 2010.
- [24] S. E. Skrabalak and K. S. Suslick, "Porous MoS_2 synthesized by ultrasonic spray pyrolysis," *Journal of the American Chemical Society*, vol. 127, no. 28, pp. 9990–9991, 2005.
- [25] J. H. Huang, W. Cheuk, Y. F. Wu, F. S. C. Lee, and W. K. Ho, "Template-free synthesis of ternary sulfides submicrospheres as visible light photocatalysts by ultrasonic spray pyrolysis," *Catalysis Science & Technology*, vol. 2, pp. 1825–1827, 2012.
- [26] J. Zhang, A. Elsanousi, J. Lin et al., "Aerosol-assisted self-assembly of aluminum borate ($\text{Al}_{18}\text{B}_4\text{O}_{33}$) nanowires into three dimensional hollow spherical architectures," *Crystal Growth and Design*, vol. 7, no. 12, pp. 2764–2767, 2007.

Research Article

Photocatalysis and Photoelectrochemical Properties of Tungsten Trioxide Nanostructured Films

Chin Wei Lai

Nanotechnology & Catalysis Research Centre (NANOCAT), Institute of Postgraduate Studies (IPS), University of Malaya, 3rd Floor, Block A, 50603 Kuala Lumpur, Malaysia

Correspondence should be addressed to Chin Wei Lai; cwlai@um.edu.my

Received 13 January 2014; Accepted 4 March 2014; Published 20 March 2014

Academic Editors: J. Shi and H. Zhou

Copyright © 2014 Chin Wei Lai. This is an open access article distributed under the Creative Commons Attribution License, which permits unrestricted use, distribution, and reproduction in any medium, provided the original work is properly cited.

Tungsten trioxide (WO_3) possesses a small band gap energy of 2.4–2.8 eV and is responsive to both ultraviolet and visible light irradiation including strong absorption of the solar spectrum and stable physicochemical properties. Thus, controlled growth of one-dimensional (1D) WO_3 nanotubular structures with desired length, diameter, and wall thickness has gained significant interest. In the present study, 1D WO_3 nanotubes were successfully synthesized via electrochemical anodization of tungsten (W) foil in an electrolyte composed of 1 M of sodium sulphate (Na_2SO_4) and ammonium fluoride (NH_4F). The influence of NH_4F content on the formation mechanism of anodic WO_3 nanotubular structure was investigated in detail. An optimization of fluoride ions played a critical role in controlling the chemical dissolution reaction in the interface of W/ WO_3 . Based on the results obtained, a minimum of 0.7 wt% of NH_4F content was required for completing transformation from W foil to WO_3 nanotubular structure with an average diameter of 85 nm and length of 250 nm within 15 min of anodization time. In this case, high aspect ratio of WO_3 nanotubular structure is preferred because larger active surface area will be provided for better photocatalytic and photoelectrochemical (PEC) reactions.

1. Introduction

Design and controlled growth of nanostructure semiconductor assemblies has gained significant attention in recent years due to the scientific interests and potential applications [1, 2]. In this manner, WO_3 is one of the famous electrochromic inorganic materials since Deb's discovery in 1969 [3]. WO_3 film exhibits a broad range of functional properties, such as small band gap energy (2.4–2.8 eV), deeper valence band (+3.1 eV), stable physicochemical properties, and strong photocorrosion stability in aqueous solution [4–10]. The characteristics of WO_3 film make them suitable for electrochromic layers in a smart window [11]. Many studies pertaining to WO_3 nanostructures are mainly aimed at the formation of high active surface area in view of their use in electrochromic applications [9, 10]. However, several studies have reported that growth of well-aligned and uniformity of anodic WO_3 nanotubular structure was a difficult task and most of the studies were only able to grow anodic WO_3 into nanoporous instead of nanotubular

structure [7–10, 12, 13]. In the present study, we describe the synthesis of well-aligned anodic WO_3 nanotubes using electrochemical anodization technique in a fluorinated-based electrolyte. To the best of our knowledge, literatures on optimization of the geometrical features of regular anodic WO_3 nanotubular structures are still lacking. Thus, such mechanistic studies and understanding are very important to tailor the desired length, pore size, and wall thickness of ordered WO_3 nanotubular structures for high surface area to volume ratio. In this study, a comprehensive experiment was conducted to control the one-dimensional nanostructure of anodic WO_3 using electrochemical anodization to achieve effective photocatalytic degradation of MO dye and H_2 gas generation via PEC water splitting process.

2. Experimental Procedure

The high purity (99.95% purity with 0.1 mm in thickness) tungsten (W) foils from Alfa Aesar USA were used in

this study. Prior to anodization, W foils were degreased in ultrasonic bath containing ethanol for 30 minutes. The foils were then rinsed in deionized water and dried in nitrogen stream. Then, anodization was performed in a two-electrode configuration bath with W foil served as the anode and the platinum electrode served as the counter electrode. The electrolyte is composed of 100 mL of 1 M of sodium sulfate (Na_2SO_4 , Merck, USA) solution with ammonium fluoride (NH_4F , Merck, USA) at 40 V with sweep rate of 1 V/s. In the present study, different content of NH_4F (0.3, 0.5, and 0.7 wt%) will be added into 1 M Na_2SO_4 solution for several anodization duration (15, 30, and 60 min) in order to investigate the formation of anodic WO_3 nanotubular structures. As-anodized anodic WO_3 samples were cleaned using acetone (J.T. Baker, Nederland) and dried in nitrogen stream after anodization process. The morphologies of anodic WO_3 nanostructures were observed by field emission scanning electron microscopy (FESEM), using a FEI Quanta 200 (FESEM model, USA) at a working distance of around 1 mm. The cross-sectional observation was carried out on mechanically bent samples to get the thickness of the oxide layer. The chemical stoichiometry of the sample was characterized using energy dispersive X-ray (EDX) analysis, which is equipped in the FESEM. In order to assess the photocatalytic performance of the anodic WO_3 nanostructure formed, anodized W foil of 25 mm \times 25 mm was prepared and placed in 200 mL of 30 ppm MO dye in a customized photoreactor made of quartz glass. Two different surface morphologies of anodic WO_3 nanostructure were selected for MO dye degradation purpose (e.g., oxide layer and nanotubular structure). In the present study, both samples were left in the photoreactor for 30 min in a dark environment to achieve adsorption/desorption equilibrium. Then, both samples were photo-irradiated at room temperature by using a 150 W Xenon solar simulator (Zolix LSP-X150) with intensity of 800 W/m^2 . A 5 mL solution was removed at an interval of 1 h from the photoreactor, and concentration of the solution was measured using a UV spectrophotometer (PerkinElmer Lambda 35). Next, the photoelectrochemical properties of the selected samples were further characterized using a three-electrode water splitting cell, with WO_3 nanotubes as the working electrode, platinum rod as the counter electrode, and saturated calomel electrode (SCE) as the reference electrode. The bath with electrolyte composed of 0.5 M sulfuric acid aqueous solution was selected in this experimental work. The H_2 gas generated at platinum rod was collected using the water displacement technique. As the H_2 gas was produced in counter electrode in water splitting chamber, it was bubbling up into inverted burette. The volume of H_2 gas was determined by reading the gas level on the side of burette.

3. Results and Discussion

In the present study, the effect of fluoride content and anodization time on the morphology of anodic WO_3 layer was investigated. Figure 1 to Figure 3 showed the surface morphologies of anodic WO_3 layer in different fluoride content electrolyte from 15 min up to 60 min of anodization

time. As shown from the FESEM images, the appearance of anodic WO_3 layer was strongly dependent on the fluoride content and anodization times. Then, the EDX analysis was employed to investigate the composition of element of W and O from the anodic WO_3 layer. Based on the results obtained, the atomic percentage of W element was about 55 at% and O element was about 45% at%. During electrochemical anodization, fluoride content played an important role in controlling the chemical dissolution rate at the interface of W/ WO_3 [14]. Figure 1 exhibited variations of WO_3 surface morphology under low 0.3 wt% fluoride content electrolyte for different anodization times. It could be observed that formation of oxide layer on W foil was incomplete at 15 min of anodization time (Figure 1(a)). Interestingly, only thin compact oxide layer with randomly pits was formed after prolonging the anodization time to 30 min and 60 min (Figures 1(b) and 1(c)). The resultant thickness of oxide layer was approximately 100 nm. These results indicated that low fluoride concentration was insufficient in forming the deep and large pore size on the oxide layer due to the inactive chemical dissolution reaction [15]. In this case, oxygen ions within the electrolyte through the W surface towards the W/ WO_3 interface induce further growth of the oxide layer under applied potential. The high electric field across the oxide layer of WO_3 and subsequently induce the polarization of W–O bonding, which is able to transfer the W^{6+} ions from the pores and leave behind random pits [14, 15]. By further increasing the content of fluoride to 0.5 wt%, the irregular anodic WO_3 nanoporous structure with thickness of approximately 200 nm could be observed from Figures 2(a) to 2(c). However, it could be noticed that the pore diameter on the oxide layer was increasing up to 70 nm when prolonging the anodization time to 60 min. The uniform anodic nanoporous WO_3 layer could be achieved in 1 M Na_2SO_4 electrolyte composed of 0.5 wt% fluorides content. When the fluoride content was further increased to 0.7 wt%, a hollow cylinder oxide nanostructure was observed as shown in Figure 3(a), which indicated that the amount of fluoride in the electrolyte was sufficient to increase the chemical dissolution rate. This condition led to further acidification reactions to develop the nanoporous structure into nanotubular structure [16–18]. In this case, tungsten fluoro-complex ions within the electrolyte playing an important role in inducing chemical dissolution to enlarge and deepen pores and eventually transforming to nanotubular structure [14]. It is noteworthy to mention that the WO_3 nanotubes with diameters of approximately 85 nm and lengths of 250 nm were successfully formed when the fluoride content was increased to 0.7 wt%. However, nanotubular structure disappeared when further the anodization time increased to 30 min and 60 min and eventually resulted in irregular nanoporous structure (Figures 3(b) and 3(c)). The reason might be attributed to the excessive chemical etching on the wall surface of nanotubes during the chemical dissolution reactions. Thus, optimization of fluoride content identified in our electrolyte was 0.5 wt% in order to grow the well-aligned one-dimensional WO_3 nanotubes for 15 min electrochemical anodization duration. Figure 4 presented a simple schematic illustration of formation of

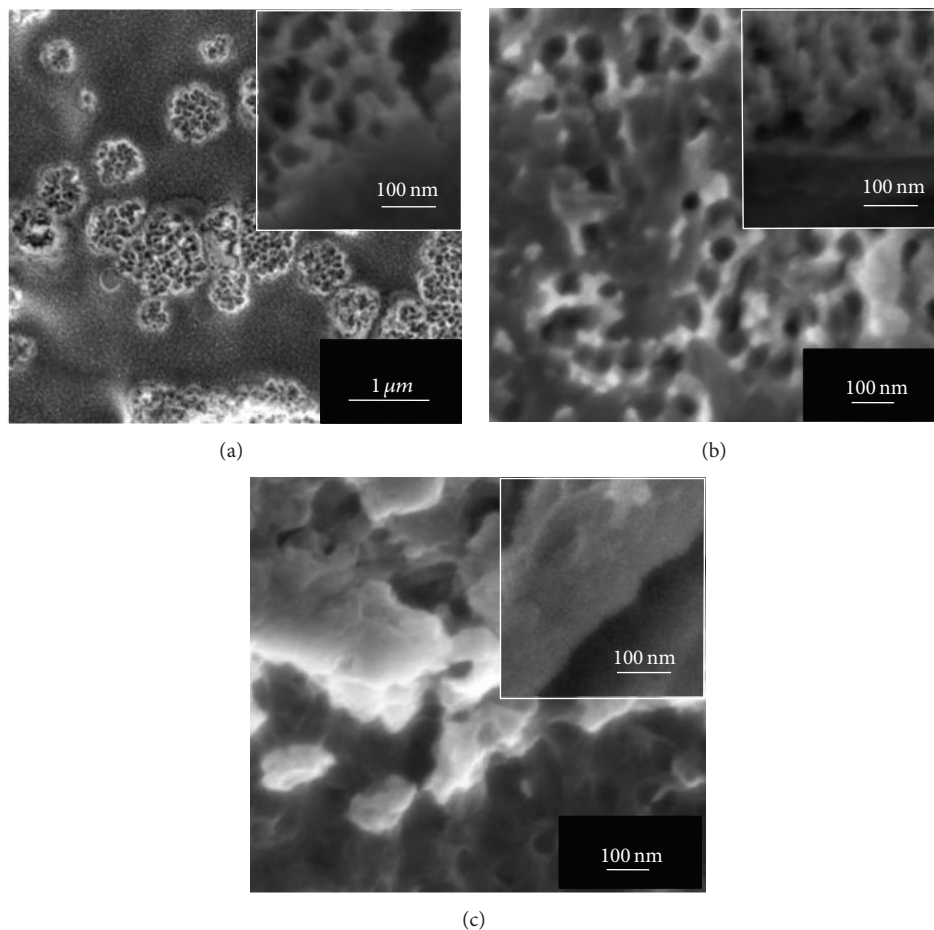


FIGURE 1: FESEM images of anodic WO_3 nanostructures obtained in 1M Na_2SO_4 electrolyte containing 0.3 wt% NH_4F for different anodization times at 40 V: (a) 15 min, (b) 30 min, and (c) 60 min. Insets show the cross-sectional view of anodic oxide layers.

anodic WO_3 nanostructured film during electrochemical anodization stage in the presence of insufficient and adequate fluoride content.

The photocatalytic removal ability of the selected sample of anodic WO_3 oxide layer was compared with that of the anodic WO_3 nanotubular structure by exposing the samples to MO dye under solar illumination. The initial MO dye concentration in the solution was fixed at 30 ppm. The changes in MO dye concentration were investigated within 5 hours and the result was shown in Figure 5. The degradation rates of MO dye concentration for sample “anodic WO_3 oxide layer” and sample “anodic WO_3 nanotubular structure” was decreased from 30 ppm to 13.5 ppm and 8.5 ppm, respectively. When anodic WO_3 nanotubular structure exposed to the $h\nu$ illumination that solar photonic energy is higher than its band gap energy (2.4–2.8 eV), the anodic WO_3 itself will generate pairs of photo-induced electrons (e^-) and holes (h^+). In this manner, the e^- and oxygen molecule (O_2) will combine to form super oxide anion ($\text{O}_2^{\bullet-}$), whereas the h^+ of anodic WO_3 and water molecule (H_2O) will generate hydroxyl radical ($\bullet\text{OH}$). These powerful oxidizing agents ($\bullet\text{OH}$ and $\text{O}_2^{\bullet-}$) will then decompose the MO dye (organic dye) into CO_2 and H_2O . This cycle will continue

when the $h\nu$ illumination is available. A simple schematic illustration of basic principal in photocatalytic degradation of MO dye is shown in Figure 6. In theoretical perspectives, the photocatalytic degradation performance of anodic WO_3 can be related on the ability to generate pairs of charge carriers, which will release powerful oxidizing agents ($\bullet\text{OH}$ and $\text{O}_2^{\bullet-}$) that are able to undergo the secondary reactions. In other words, anodic WO_3 nanotubular structure with larger surface area of active reaction sites (inner and outer wall surface of nanotubes) has better photon absorption under $h\nu$ illumination. The distance of light scattering inside the nanotubes extends and provides more photon absorption to trigger the photocatalytic degradation reaction.

On the other hand, the evolution rate of H_2 gas generated from the photoelectrochemical (PEC) water-splitting process under solar illumination was measured. The H_2 evolution as a function of time is shown in Figure 7. H_2 generation rate from water splitting reaction increased linearly with increasing exposure time. The sample (anodic WO_3 nanotubular structure) achieved a maximum evolution of approximately $1 \text{ mL}/\text{cm}^2$ within 1 hour, which is relatively higher compared with the anodic WO_3 oxide layer. The H_2 production completely stopped after the termination

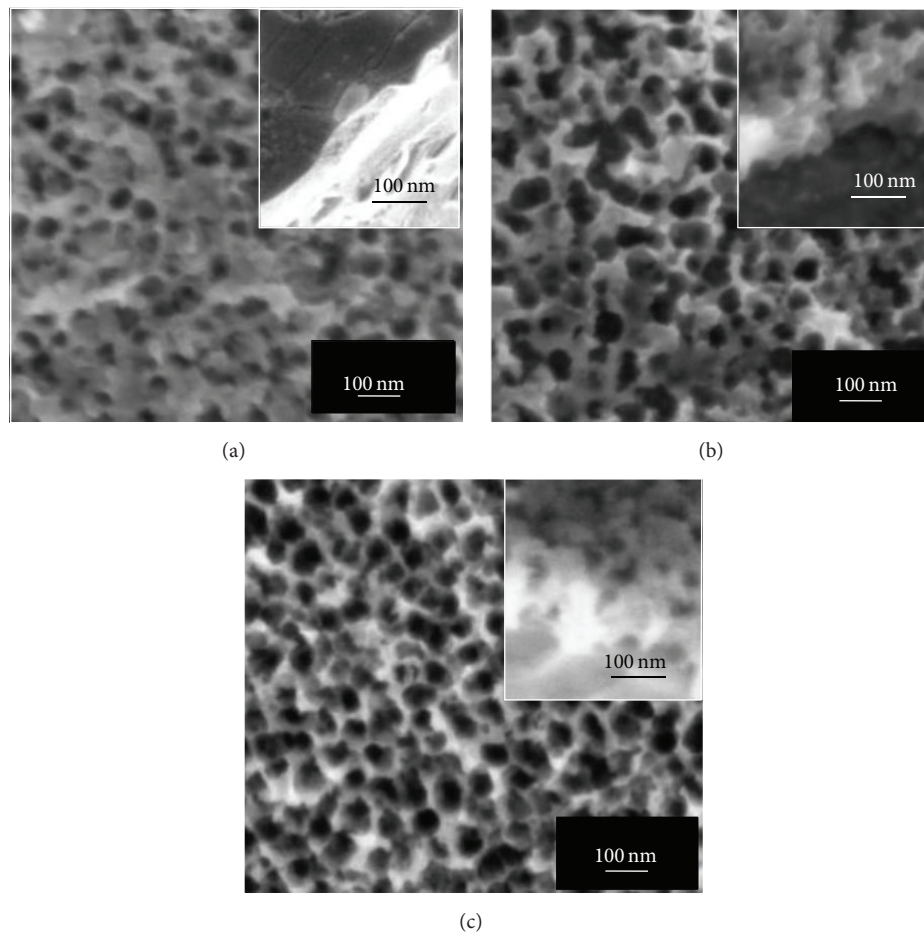


FIGURE 2: FESEM images of anodic WO_3 nanostructures obtained in 1M Na_2SO_4 electrolyte containing 0.5 wt% NH_4F for different anodization times at 40 V: (a) 15 min, (b) 30 min, and (c) 60 min. Insets show the cross-sectional view of anodic oxide layers.

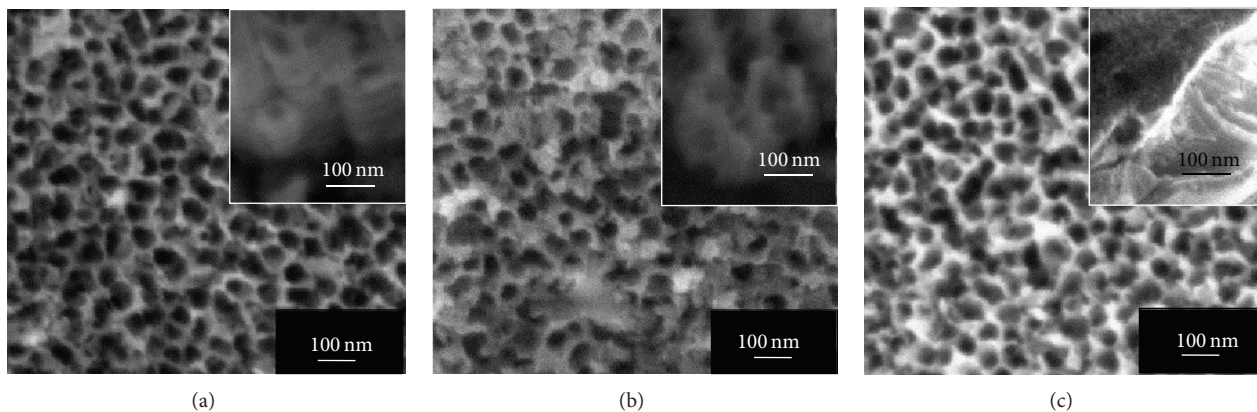


FIGURE 3: FESEM images of anodic WO_3 nanostructures obtained in 1M Na_2SO_4 electrolyte containing 0.7 wt% NH_4F for different anodization times at 40 V: (a) 15 min, (b) 30 min, and (c) 60 min. Insets show the cross-sectional view of anodic oxide layers.

of $h\nu$ illumination. This observation clearly shows that H_2 is only produced photocatalytically. A constant production rate of H_2 gas could be observed in the present study. In theoretical perspectives, PEC water splitting process is the general term for a chemical reaction in which water is

separated into O_2 and H_2 using anodic WO_3 film that catalyze the water splitting reaction. A basic schematic diagram of such overall water splitting reaction using a semiconductor photocatalyst is presented in Figure 8. The water splitting reaction can be summarized as follows: $2\text{H}_2\text{O}(l) \rightarrow$

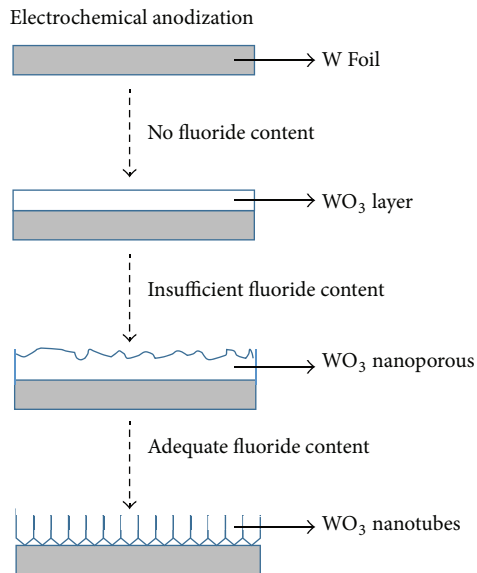


FIGURE 4: Schematic illustration of formation and mechanistic studies of anodic WO₃ nanostructured film with and without fluoride content during electrochemical anodization stage.

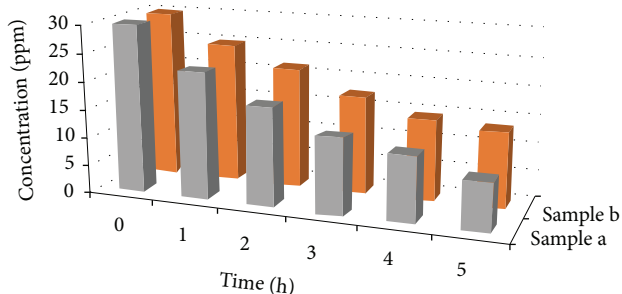


FIGURE 5: Photodegradation of MO dye: (a) anodic WO₃ nanostructures obtained in 1 M Na₂SO₄ electrolyte containing 0.7 wt% NH₄F for 15 min at 40 V, (b) anodic WO₃ nanostructures obtained in 1 M Na₂SO₄ electrolyte containing 0.3 wt% NH₄F for 15 min at 40 V.

O₂(g) + 2H₂(g). The overall water splitting reaction is considered as a thermodynamically uphill reaction with a large Gibbs free energy of $\Delta G^0 = +237.2 \text{ KJ mol}^{-1}$. This reaction indicates that photon energy is required to overcome the large positive change in Gibbs free energy through PEC water splitting process [19, 20]. The light-driven water splitting process is triggered when anodic WO₃ film absorbs photons from $h\nu$ illumination with energies greater than its band gap energy. This light absorption generates negative e⁻ in the conduction band and positive h⁺ in the valence band. The h⁺ performs work at the anodic WO₃ electrolyte interface oxidizing water molecules to create O₂ and H⁺ ions within the electrolyte. Then, the e⁻ will move through the external circuit to the platinum electrode (counter electrode) where they reduce H⁺ ions creating H₂ molecules due to the electric field or under external bias [20]. The PEC water splitting performance is consistent with the photocatalytic degradation. In summary, the self-organized WO₃ nanotubular structure

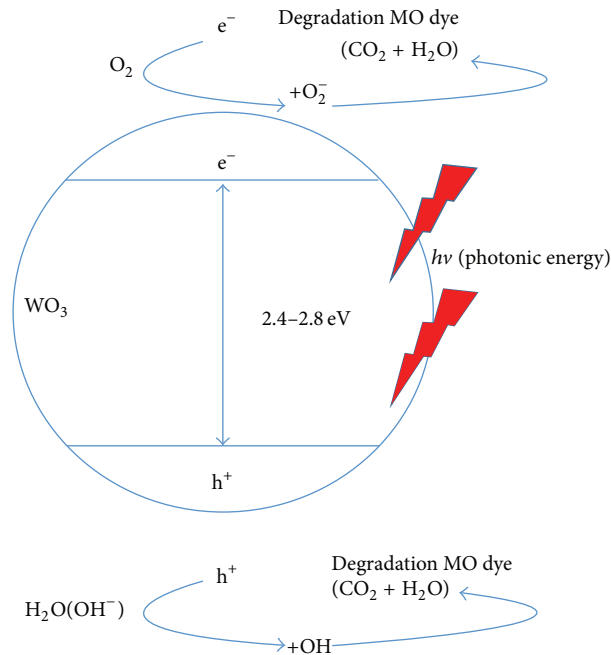


FIGURE 6: The overall mechanism of the photocatalytic degradation of MO dye using WO₃ nanostructured film under solar illumination.

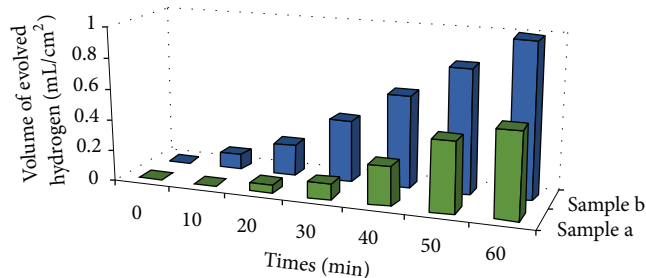


FIGURE 7: H₂ evolution under solar illumination of (a) anodic WO₃ nanostructures obtained in 1 M Na₂SO₄ electrolyte containing 0.3 wt% NH₄F for 15 min at 40 V and (b) anodic WO₃ nanostructures obtained in 1 M Na₂SO₄ electrolyte containing 0.7 wt% NH₄F for 15 min at 40 V.

has strong ability to release much more photo-induced e⁻/h⁺ pairs than that of compact layer structure. Thus, it is crucial to maximize the active surface area of photocatalyst (anodic WO₃) for better photocatalytic and photoelectrochemical performance.

4. Conclusion

In conclusion, complete transformation of W foil to one-dimensional WO₃ nanotubes with an average diameter of 85 nm and length of 250 nm could be achieved within 15 min in an electrolyte composed of 1M of Na₂SO₄ and 0.7 wt% of NH₄F. The main reason attributed to the sufficiency of tungsten fluoro-complex ions induced chemical dissolution to enlarge and deepen pores and eventually transform to nanotubes. The ability to grow large active surface area

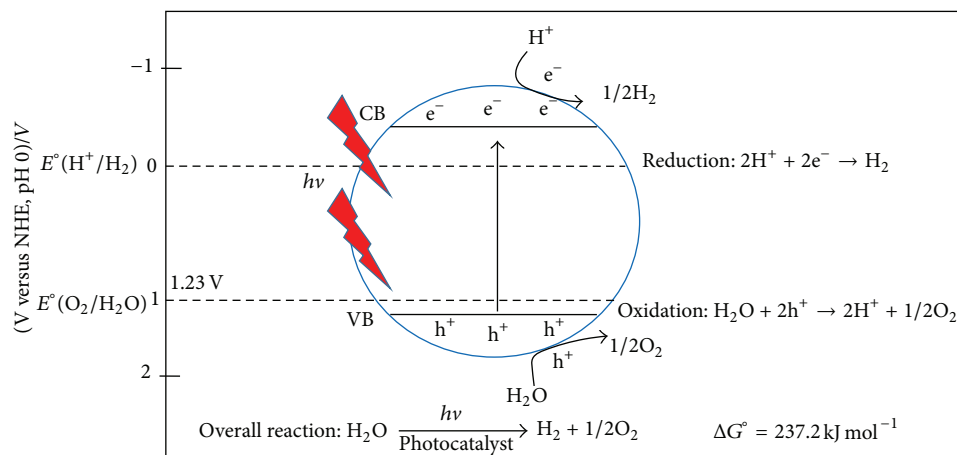


FIGURE 8: Basic principle of the overall water splitting for H_2 generation using a WO_3 nanostructured film.

of anodic WO_3 nanostructures demonstrated a substantial enhancement in the degradation of MO dye and H_2 generation via water splitting process, as compared to the anodic WO_3 oxide layers.

Conflict of Interests

The author declares that there is no conflict of interests regarding the publication of this paper.

Acknowledgments

This research is supported by High Impact Research Chancellor Grant UM.C/625/1/HIR/228 (J55001-73873) from the University of Malaya. In addition, authors would like to thank University of Malaya for sponsoring this work under University of Malaya Research Grant (UMRG, RP022-2012D).

References

- [1] C. A. Grimes, "Synthesis and application of highly ordered arrays of TiO_2 nanotubes," *Journal of Materials Chemistry*, vol. 17, pp. 1451–1457, 2013.
- [2] C. W. Lai and S. Sreekantan, "Preparation of hybrid WO_3 - TiO_2 nanotube photoelectrodes using anodization and wet impregnation: improved water-splitting hydrogen generation performance," *International Journal of Hydrogen Energy*, vol. 38, no. 5, pp. 2156–2166, 2013.
- [3] S. K. Deb, "A novel electrophotographic system," *Applied Optics*, vol. 8, no. 1, pp. 192–195, 1969.
- [4] C. Trimble, M. DeVries, J. S. Hale, D. W. Thompson, T. E. Tiwald, and J. A. Woollam, "Infrared emittance modulation devices using electrochromic crystalline tungsten oxide, polymer conductor, and nickel oxide," *Thin Solid Films*, vol. 355, pp. 26–34, 1999.
- [5] I. Bedja, S. Hotchandani, R. Carpentier, K. Vinodgopal, and P. V. Kamat, "Electrochromic and photoelectrochemical behavior of thin WO_3 films prepared from quantized colloidal particles," *Thin Solid Films*, vol. 247, no. 2, pp. 195–200, 1994.
- [6] C. W. Lai and S. Sreekantan, "Fabrication of WO_3 nanostructures by anodization method for visible-light driven water splitting and photodegradation of methyl orange," *Materials Science in Semiconductor Processing*, vol. 16, no. 2, pp. 303–310, 2012.
- [7] A. Watcharenwong, W. Chanmanee, N. R. de Tacconi, C. R. Chenthamarakshan, P. Kajitvichyanukul, and K. Rajeshwar, "Anodic growth of nanoporous WO_3 films: morphology, photoelectrochemical response and photocatalytic activity for methylene blue and hexavalent chrome conversion," *Journal of Electroanalytical Chemistry*, vol. 612, no. 1, pp. 112–120, 2008.
- [8] X. Zhang, K. Huo, L. Huo, L. Hu, and P. K. Chu, "Fabrication and photocatalytic activity of nanoporous WO_3 film," *Nanoscience and Nanotechnology Letters*, vol. 2, no. 1, pp. 51–57, 2010.
- [9] W. Li, J. Li, X. Wang, S. Luo, J. Xiao, and Q. Chen, "Visible light photoelectrochemical responsiveness of self-organized nanoporous WO_3 films," *Electrochimica Acta*, vol. 56, no. 1, pp. 620–625, 2010.
- [10] S. Berger, H. Tsuchiya, A. Ghicov, and P. Schmuki, "High photocurrent conversion efficiency in self-organized porous WO_3 ," *Applied Physics Letters*, vol. 88, no. 20, Article ID 203119, 2006.
- [11] C. G. Granqvist, "Electrochromic tungsten oxide films: review of progress 1993–1998," *Solar Energy Materials and Solar Cells*, vol. 60, no. 3, pp. 201–262, 2000.
- [12] V. Cristino, S. Caramori, R. Argazzi, L. Meda, G. L. Marra, and C. A. Bignozzi, "Efficient photoelectrochemical water splitting by anodically grown WO_3 electrodes," *Langmuir*, vol. 27, no. 11, pp. 7276–7284, 2011.
- [13] Y. Nah, A. Ghicov, D. Kim, and P. Schmuki, "Enhanced electrochromic properties of self-organized nanoporous WO_3 ," *Electrochemistry Communications*, vol. 10, no. 11, pp. 1777–1780, 2008.
- [14] C. W. Lai, S. B. A. Hamid, and S. Sreekantan, "A novel solar driven photocatalyst: well-aligned anodic WO_3 nanotubes," *International Journal of Photoenergy*, vol. 2013, Article ID 745301, 6 pages, 2013.
- [15] C. W. Lai, S. Sreekantan, and Z. Lockman, "Photoelectrochemical behaviour of uniform growth TiO_2 nanotubes via bubble blowing synthesised in ethylene glycol with hydrogen peroxide," *Journal of Nanoscience and Nanotechnology*, vol. 12, no. 5, pp. 4057–4066, 2012.
- [16] C. W. Lai, S. Sreekantan, and J. Nanomater, "Effect of applied potential on the formation of self-organized TiO_2 nanotube

- arrays and its photoelectrochemical response," *Journal of Nanomaterials*, vol. 2011, Article ID 142463, 7 pages, 2011.
- [17] Y. C. Nah, I. Paramasivam, and P. Schmuki, "Doped TiO₂ and TiO₂ nanotubes: synthesis and applications," *ChemPhysChem*, vol. 11, no. 13, pp. 2698–2713, 2010.
- [18] Z. Su and W. Zhou, "Formation, morphology control and applications of anodic TiO₂ nanotube arrays," *Journal of Materials Chemistry*, vol. 21, pp. 8955–8970, 2011.
- [19] D. Y. C. Leung, X. L. Fu, C. F. Wang et al., "Hydrogen production over titania-based photocatalysts," *ChemSusChem*, vol. 3, no. 6, pp. 681–694, 2010.
- [20] C. W. Lai and S. Sreekantan, "Study of WO₃ incorporated C-TiO₂ nanotubes for efficient visible light driven water splitting performance," *Journal of Alloys and Compounds*, vol. 547, pp. 43–50, 2013.

Research Article

Enhanced Water Splitting by Fe₂O₃-TiO₂-FTO Photoanode with Modified Energy Band Structure

Eul Noh,¹ Kyung-Jong Noh,¹ Kang-Seop Yun,¹ Bo-Ra Kim,¹ Hee-June Jeong,¹ Hyo-Jin Oh,¹ Sang-Chul Jung,² Woo-Seung Kang,³ and Sun-Jae Kim¹

¹ Institute/Faculty of Nanotechnology and Advanced Materials Engineering, Sejong University, Seoul 143-747, Republic of Korea

² Department of Environmental Engineering, Sunchon National University, Suncheon, Jeonnam 540-742, Republic of Korea

³ Department of Metallurgical & Materials Engineering, Inha Technical College, Incheon 402-752, Republic of Korea

Correspondence should be addressed to Woo-Seung Kang; wkang651@inhac.ac.kr and Sun-Jae Kim; sjkim1@sejong.ac.kr

Received 19 October 2013; Accepted 24 November 2013

Academic Editors: D. Jing, J. Shi, and H. Zhou

Copyright © 2013 Eul Noh et al. This is an open access article distributed under the Creative Commons Attribution License, which permits unrestricted use, distribution, and reproduction in any medium, provided the original work is properly cited.

The effect of TiO₂ layer applied to the conventional Fe₂O₃/FTO photoanode to improve the photoelectrochemical performance was assessed from the viewpoint of the microstructure and energy band structure. Regardless of the location of the TiO₂ layer in the photoanodes, that is, Fe₂O₃/TiO₂/FTO or TiO₂/Fe₂O₃/FTO, high performance was obtained when α -Fe₂O₃ and H-TiNT/anatase-TiO₂ phases existed in the constituent Fe₂O₃ and TiO₂ layers after optimized heat treatments. The presence of the Fe₂O₃ nanoparticles with high uniformity in the each layer of the Fe₂O₃/TiO₂/FTO photoanode achieved by a simple dipping process seemed to positively affect the performance improvement by modifying the energy band structure to a more favorable one for efficient electrons transfer. Our current study suggests that the application of the TiO₂ interlayer, together with α -Fe₂O₃ nanoparticles present in the each constituent layers, could significantly contribute to the performance improvement of the conventional Fe₂O₃ photoanode.

1. Introduction

Green energy sources have been extensively investigated to replace the fossil fuels due to their inherent problems of pollution and limited resources [1]. Among them, hydrogen (H₂) gas was one of the most actively studied energy sources owing to its abundance, high specific energy capacity, and environmentally friendliness [2–4]. Hydrogen can be produced by using hydrocarbons such as fossil fuels, natural gas, and water. Production of hydrogen gas by electrolysis of water has been known to be the most efficient way [5–7]. Energy required to generate hydrogen and oxygen by electrolysis of water can be supplied through sun light. For the sun light to be effectively utilized, electrodes having functions of photoabsorbent and catalyst need to be employed for electrolysis of water. Photoelectrochemical (PEC) system is an efficient approach to produce hydrogen gas from water by utilizing an unlimited resource of the sun light without generating environmentally deleterious byproducts. With the development

of PEC system, much attention has been paid to the fabrication of high efficient photoelectrode for water splitting [4, 8–10]. Among other things, materials extensively studied for the photoelectrode were Co [11, 12], Co-Pi [13, 14], IrO₂ [15], TiO₂ [16–18], CuO [19], WO₃ [20], Fe₂O₃ [21], and so forth.

In particular, more interest has been drawn to Fe₂O₃ material which could harvest visible part of solar spectrum [21–23]. However, Fe₂O₃ has some critical issues to be resolved for the application to the PEC system as photoelectrode such as electron-hole recombination. Several approaches have been taken to reduce the recombination; application of nanostructured materials, doping with appropriate materials, and so forth. Photocurrent density generated with the Fe₂O₃ nanorods and nanowires was reported to have 1.3 mA/cm² [21] and 0.54 mA/cm² at 1.23 (V versus RHE) [22], respectively. On the other hand, Fe₂O₃ photoanode doped with Ti and Si showed a little better performance of 1.83 mA/cm² [24] and 2.2 mA/cm² at 1.23 (V versus RHE) [25], respectively. However, the photocurrent density

of Fe_2O_3 photoanode modified with the nanostructures and doping was found to be still far below the theoretical value of 12.6 mA/cm^2 at 1.23 V versus RHE). From our previous work, we reported a high photocurrent density of 1.32 mA/cm^2 at 1.23 V versus RHE) with $\text{Fe}_2\text{O}_3/\text{FTO}$ photoanode without any doping [26], synthesized by a simple process of dip coating and short-time heat treatment at 500°C of nanosized Fe_2O_3 on the FTO substrate. Our results confirmed the importance of microstructure of Fe_2O_3 to the reduction of electron-hole recombination, which could be modified and optimized by the coating amount of Fe_2O_3 and following heat treatment conditions [27]. Taking advantage of photocatalytic effect of TiO_2 , $\text{Fe}_2\text{O}_3/\text{TiO}_2/\text{FTO}$ photoanode was also fabricated in another study. From the energy band structure viewpoint of the photoanode, the electrons generated on the Fe_2O_3 film should overcome a barrier to be transferred to FTO, probably deteriorating the performance [28]. However, the photoanode showed the opposite result of much higher photocurrent density of 4.81 mA/cm^2 at 1.23 V versus RHE) [29].

In this current work, the effect of microstructure and energy band structure of the photoanodes with the different arrangement of the constituent elements (e.g., $\text{TiO}_2/\text{Fe}_2\text{O}_3/\text{FTO}$, $\text{Fe}_2\text{O}_3/\text{TiO}_2/\text{FTO}$) on the performance was investigated and discussed in relation with the electrons transfer in the photoanode.

2. Experimental Details

FTO glasses (Asahi Glass Co.) as a conducting substrate of Fe_2O_3 photoanode film for water splitting was at first etched for 20 min using Piranha solution (7:3 = 70% conc. H_2SO_4 :30% H_2O_2) to make them have fresh surface and then were dipped simply to make H-TiNT (hydrogen titanate nanotube) particles supported in aqueous $\text{Fe}(\text{NO}_3)_3$ solution (corresponding to Fe_2O_3 precursor) or H-TiNT particles dispersed solution (corresponding to TiO_2 precursor particles). In this study, various photoanode arrangements such as $\text{Fe}(\text{NO}_3)_3/\text{FTO}$, $\text{Fe}(\text{NO}_3)_3/\text{H-TiNT}/\text{FTO}$, and $\text{H-TiNT}/\text{Fe}(\text{NO}_3)_3/\text{FTO}$ were prepared. Coated $\text{Fe}(\text{NO}_3)_3$ and H-TiNT particles were transformed into Fe_2O_3 and TiO_2 phases, respectively, with heat treatments at 500°C for 10 min in air. In other words, for the performance improvement of Fe_2O_3 film, the arrangements with H-TiNT interlayer incorporated in between $\text{Fe}(\text{NO}_3)_3$ and FTO and with H-TiNT top layer on the $\text{Fe}(\text{NO}_3)_3/\text{FTO}$ were tried. All aqueous solutions in this experiment were prepared using distilled water with $1.8 \text{ M}\Omega$.

To make H-TiNT interlayer (finally $\text{Fe}_2\text{O}_3/\text{TiO}_2/\text{FTO}$ arrangement), the FTO glass after having been surface-treated for 20 min in 0.2 M polyethyleneimine (PEI, Aldrich Co.) aqueous solution containing positively charged ions was used as a transparent conductive substrate. First, the surface-pretreated FTO glass was immersed for 20 min in an aqueous 10 g/L H-TiNT particle solution dispersed together with 0.2 M tetrabutylammonium hydroxide (TBAOH, Aldrich Co.) to produce negatively charged ions. Afterwards, using the same method, an H-TiNT-treated film was subsequently

immersed in 0.2 M polydiallyldimethylammonium chloride (PDDA, Aldrich Co.) aqueous solution, which contained positively charged ions. The obtained H-TiNT/FTO glass was dried under UV-Vis light irradiation (Hg-Xe 200 W lamp, Super-cure, SAN-EI Electric) to remove water and all surfactants, such as PEI, TBAOH, and PDDA using photocatalytic removal reaction occurred by H-TiNT particles with optical energy bandgap of 3.5 eV [24], without any sintering. Then, for the $\text{Fe}(\text{NO}_3)_3$ nanoparticle coating process, the dried H-TiNT/FTO substrates were dipped in an aqueous 1.0 M $\text{Fe}(\text{NO}_3)_3$ solution with dipping times of 12 hrs. For formations of H-TiNT top layer on $\text{Fe}(\text{NO}_3)_3/\text{FTO}$ films (finally $\text{TiO}_2/\text{Fe}_2\text{O}_3/\text{FTO}$ arrangement), the precursor solution of Fe_2O_3 film supported was made of 1.0 M $\text{Fe}(\text{NO}_3)_3 \cdot 9\text{H}_2\text{O}$ and 0.2 M TBAOH (tetrabutylammonium hydroxide, Aldrich) for dipping fresh FTO substrate for 12 hrs. After that, obtained $\text{Fe}(\text{NO}_3)_3/\text{FTO}$ were dried at 80°C for 12 hrs. For formation of H-TiNT/ $\text{Fe}(\text{NO}_3)_3/\text{FTO}$ films, repetitive self-assembling of oppositely charged ions in an aqueous solution was applied to coat directly the H-TiNT particles using the same process explained above. All dipping process was carried out at room temperature in air.

All heat treatment was done inside a box furnace with heating rate of $500^\circ\text{C}/\text{sec}$ to produce the final photoanode thin film with $\alpha\text{-Fe}_2\text{O}_3$ phase for the water splitting process, where the rapid heating rate was accomplished by plunging the samples into the hot zone of the furnace maintained at the setting temperatures of $420\sim 550^\circ\text{C}$. Repetition of this process yielded an H-TiNT particle thin film coated on the FTO or Fe_2O_3 film with approximately 700~1000 nm thickness as previously reported in our researches [30]. After the heat treatment at various conditions, the surface microstructure of the Fe_2O_3 thin films was observed with scanning electron microscope (SEM; S-4700, Hitachi) and their crystallinity was analyzed using X-ray diffractometer (XRD; D/MAX 2500, Rigaku), Raman spectroscopy (Renishaw, inVia Raman microscope), UV-Vis spectroscopy (S-3100, Sinco). To measure the I - V and C - V electrochemical properties using $\mu\text{Autolab}$ type III potentiostat (Metrohm Autolab), a calomel electrode and a Pt wire were used as the reference and counter electrodes, respectively, when the as-prepared, heat-treated coated $\text{Fe}_2\text{O}_3/\text{H-TiNT}$ composite films with various arrangements were used as the working electrode in an aqueous 1.0 M NaOH deaerated solution under irradiation of 100 mW/cm^2 UV-Vis spectrum (Hg-Xe 200 W lamp, Super-cure, SAN-EI Electric). The measured potentials versus calomel were converted to the reversible hydrogen electrode (RHE) scale in all I - V graphs.

3. Results and Discussions

Figure 1 shows I - V photoelectrochemical data and surface morphology of the Fe_2O_3 precursor/(H-TiNT)/FTO samples, which had been heat treated at the predetermined temperatures of $420\sim 550^\circ\text{C}$ for 10 min. The amount of Fe_2O_3 in the samples was 65.48 wt% for the $\text{Fe}_2\text{O}_3/\text{H-TiNT}/\text{FTO}$ and about 30 wt% for the $\text{Fe}_2\text{O}_3/\text{FTO}$, which was determined based on the I - V photoelectrochemical performance as

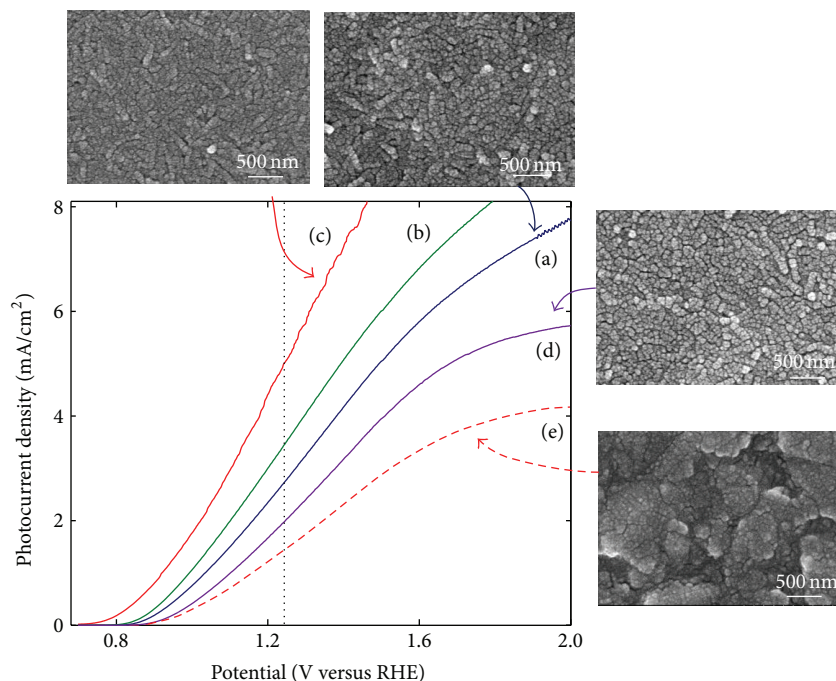


FIGURE 1: Photoelectrochemical I - V characteristics of Fe_2O_3 precursor/ H-TiNT/FTO heat treated at (a) 420°C , (b) 460°C , (c) 500°C , and (d) 550°C in the air, compared to (e) Fe_2O_3 precursor/ FTO heat treated at 500°C .

reported in our previous study [29]. All the samples were measured in the 1.0 M NaOH solution under 100 mW/cm^2 of UV-Vis light illumination, and the linear sweep voltammetry was in the range of $0.0\sim+2.0$ (V versus RHE). The photocurrent densities were obtained by eliminating the “dark” fraction from “illumination” data, where dark data was measured in the dark room without UV light illumination. For the comparison, sample (e) without TiO_2 interlayer was adopted from our previous work [26].

Regardless of the heat treatment temperatures, the performance improvement was observed in the samples with TiO_2 interlayer incorporated in between Fe_2O_3 and FTO . In particular, sample (c) prepared under the same condition as sample (e) other than the presence of TiO_2 interlayer film showed about 3 times increase of photocurrent density at 1.23 (V versus RHE) and the reduction of the onset voltage to about 0.75 V. These results suggest that the TiO_2 interlayer can play a significant role in the efficient collection and conversion of photoenergy. The extent of performance improvement was found to be affected by the heat treatment temperature; it showed a gradual improvement with the heat treatment temperature of up to 500°C , above which it rather deteriorated. A similar result was observed with the $\text{Fe}_2\text{O}_3/\text{FTO}$ samples without TiO_2 interlayer film in our previous work [26].

Morphology of the $\text{Fe}_2\text{O}_3/\text{FTO}$ sample after heat treatment at 500°C for 10 min was shown in Figure 1(e). The Fe_2O_3 particles were observed to form a film conformal to the FTO substrate, indicating a very thin and uniform film as noted by Oh et al. [31]. Microstructure changes of the Fe_2O_3 precursor/ H-TiNT/FTO samples were also monitored as a function of heat treatment temperature of $420\sim550^\circ\text{C}$. The

as-coated porous and rough H-TiNT particles with fibrous morphology as reported in our previous work [27] were broken into spherical particles through the heat treatments. It is noteworthy that the Fe_2O_3 particles in the $\text{Fe}_2\text{O}_3/\text{H-TiNT/FTO}$ samples were relatively smaller than those in the $\text{Fe}_2\text{O}_3/\text{FTO}$ sample, suggesting that the growth of the Fe_2O_3 particles was restrained by H-TiNT during the heat treatments. However, no noticeable microstructural differences were observed among the $\text{Fe}_2\text{O}_3/\text{H-TiNT/FTO}$ samples which could explain the performance variation occurred in the samples.

The contribution of the TiO_2 interlayer placed in between Fe_2O_3 and FTO on the photocurrent density improvement at 1.23 (V versus RHE) as a function of heat treatment temperature was quantitatively expressed in Figure 2. The data for the $\text{Fe}_2\text{O}_3/\text{FTO}$ samples were taken as a reference from our previous work [26]. The effect of the TiO_2 interlayer on the performance improvement was substantially increased with the temperature to the highest at 500°C , above which it rather declined.

Phase changes of the constituent materials in the samples with the heat treatments were observed in our previous work [30]. It was observed that Fe_2O_3 precursor was gradually transformed into $\alpha\text{-Fe}_2\text{O}_3$ phase with the increase of heat treatment temperature from 420 to 550°C . However, peaks corresponding to $\alpha\text{-Fe}_2\text{O}_3$ phase became weaker above 500°C . On the other hand, H-TiNT was transformed gradually but not fully into anatase- TiO_2 phase due to the short heat treatment time of 10 min. Therefore, from the phase and photocurrent density changes of the samples, the performance improvement is considered to be closely associated with

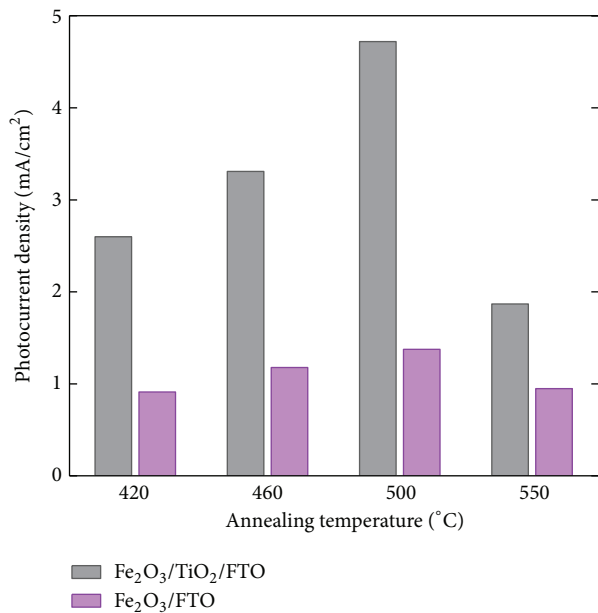


FIGURE 2: Comparison of photocurrent densities at 1.23 V versus RHE for $\text{Fe}_2\text{O}_3/\text{TiO}_2/\text{FTO}$ and $\text{Fe}_2\text{O}_3/\text{FTO}$ samples with annealing temperatures.

the phases present in the samples: the best performance could be obtained when H-TiNT and anatase- TiO_2 phases coexisted with the well-developed $\alpha\text{-Fe}_2\text{O}_3$ phase in the sample.

Effect of the coating layers arrangement in the $\text{Fe}_2\text{O}_3\text{-TiO}_2\text{-FTO}$ samples was investigated in terms of the performance in Figure 3, in which the photocurrent densities were obtained by eliminating the “dark” fraction from “illumination” data. All the samples except sample (d) were heat treated once at 500°C for 10 min in the air following synthesis of the multilayered electrodes. Sample (d) was heat treated twice under the same condition mentioned above: once after TiNT coating on the FTO, then repeated after Fe_2O_3 coating on the heat-treated TiO_2/FTO layer. Regardless of the location of TiO_2 layer, above or below Fe_2O_3 layer ($\text{Fe}_2\text{O}_3/\text{TiO}_2/\text{FTO}$ (Figures 3(b) and 3(d)) or $\text{TiO}_2/\text{Fe}_2\text{O}_3/\text{FTO}$ (Figure 3(c))), samples containing TiO_2 layer (Figures 3(b), 3(c), and 3(d)) showed much better performance compared to that (Figure 3(a)) without TiO_2 layer, increased photocurrent density as well as reduced onset voltage.

Microstructure observed in Figure 4 suggested that film uniformity along with the controlled particles size could play an important role for the performance improvement, $\text{Fe}_2\text{O}_3/\text{TiO}_2/\text{FTO}$ sample (Figure 4(b)) with the best performance consisted of smaller particles with high uniformity than sample (c) of $\text{TiO}_2/\text{Fe}_2\text{O}_3/\text{FTO}$. Double heat-treated sample (d) of $\text{Fe}_2\text{O}_3/\text{TiO}_2/\text{FTO}$ showed an inferior performance to the corresponding sample (b) with the same layer structure, which was annealed only one time. This result also confirmed the importance of microstructure to the performance; the poor microstructure with agglomerated particles and cracked surface after the double heat treatment

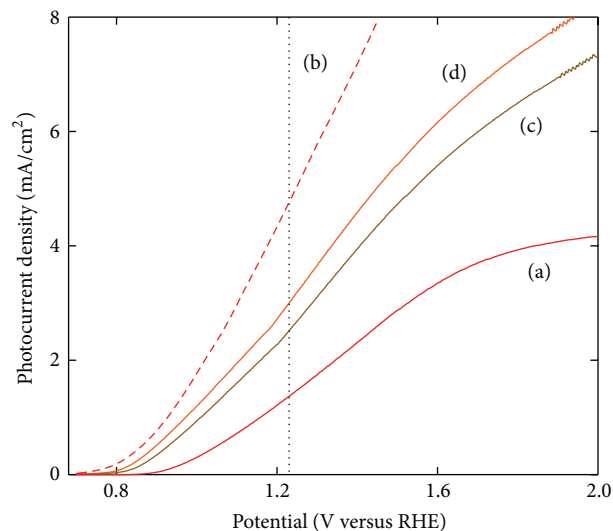


FIGURE 3: Photoelectrochemical $I\text{-}V$ characteristics of the samples with the stacking structures of (a) $\text{Fe}_2\text{O}_3/\text{FTO}$, (b) $\text{Fe}_2\text{O}_3/\text{TiO}_2/\text{FTO}$, and (c) $\text{TiO}_2/\text{Fe}_2\text{O}_3/\text{FTO}$, which were all heat treated at 500°C for 10 min in the air. Curve (d) was obtained from $\text{Fe}_2\text{O}_3/\text{TiO}_2/\text{FTO}$ double heat treated under the same condition as above: 1st after H-TiNT coating on FTO and 2nd after Fe_2O_3 coating on the heat-treated H-TiNT/FTO.

as shown in sample (d) adversely affected the performance of the sample. On the other hand, Figure 4(a) shows the Fe_2O_3 precursor powders becoming much larger when heat treated at 500°C for 10 min, compared to the Fe_2O_3 particles existing together with the TiO_2 in the case of Figures 4(b)–4(d). These observations are consistent with the results of Figure 1, which showed the restrained growth of the Fe_2O_3 particles by H-TiNT during the heat treatment.

It is noteworthy that among the samples with TiO_2 layer, the sample (Figures 4(b) and 4(d)) with the TiO_2 layer in between Fe_2O_3 and FTO layer showed better result than the sample (Figure 4(c)) having the TiO_2 layer above Fe_2O_3 layer. These results were discussed in terms of energy band structure and microstructure. Energy band diagrams of the $\text{Fe}_2\text{O}_3/\text{TiO}_2/\text{FTO}$ and $\text{TiO}_2/\text{Fe}_2\text{O}_3/\text{FTO}$ samples without UV-Vis light irradiation were schematically drawn in Figures 5(a) and 5(b), respectively. It was proposed by Wang et al. that a photoelectrode with TiO_2 based film such as SrTiO_3 located above Fe_2O_3 film was a favorable structure for electrons transfer from the energy band diagram consideration [32]. Their claim seems to be reasonable from the comparison of the energy band diagrams when being not under UV-Vis light. However, our results showed that the electrons generated on the Fe_2O_3 layer in the $\text{Fe}_2\text{O}_3/\text{TiO}_2/\text{FTO}$ photoanode could be transferred to the TiO_2/FTO when being under the UV-Vis light irradiation by overcoming the discontinuity of the conduction bands.

On the other hand, the microstructure of the $\text{Fe}_2\text{O}_3/\text{TiO}_2/\text{Fe}_2\text{O}_3$ sample synthesized for the current work was also carefully considered. While synthesizing the $\text{Fe}_2\text{O}_3/\text{TiO}_2/\text{FTO}$ sample, some of the Fe_2O_3 nanoparticles could be

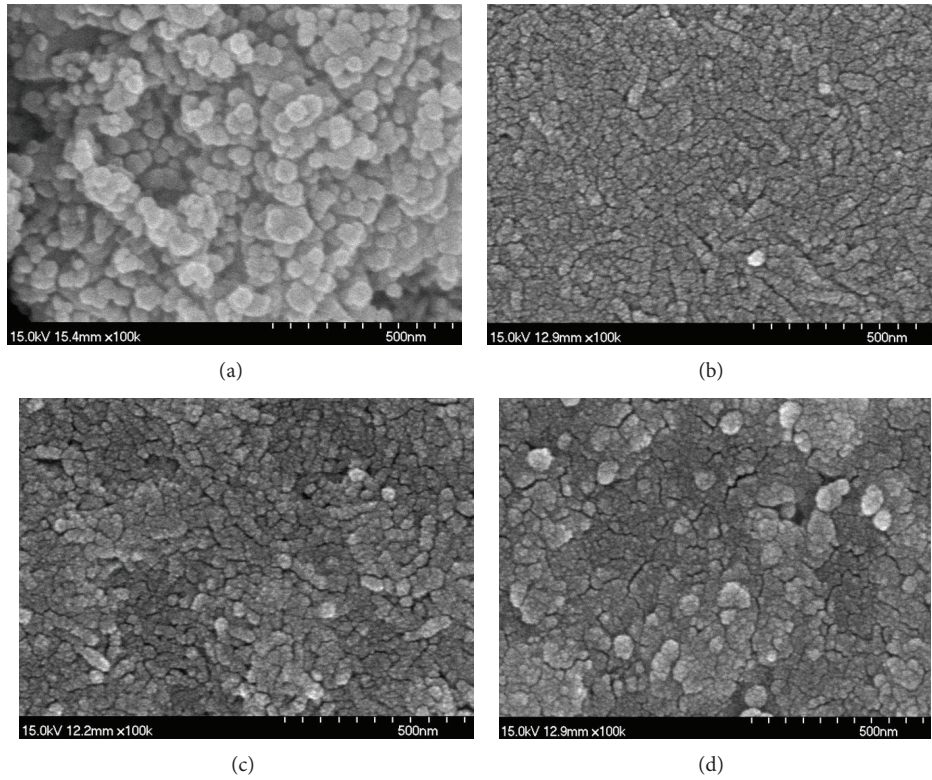


FIGURE 4: SEM photos of (a) $\text{Fe}(\text{NO}_3)_3$ powders heat treated at 500°C for 10 min, and (b), (c), (d) correspond to Figures 3(b), 3(c), and 3(d), respectively.

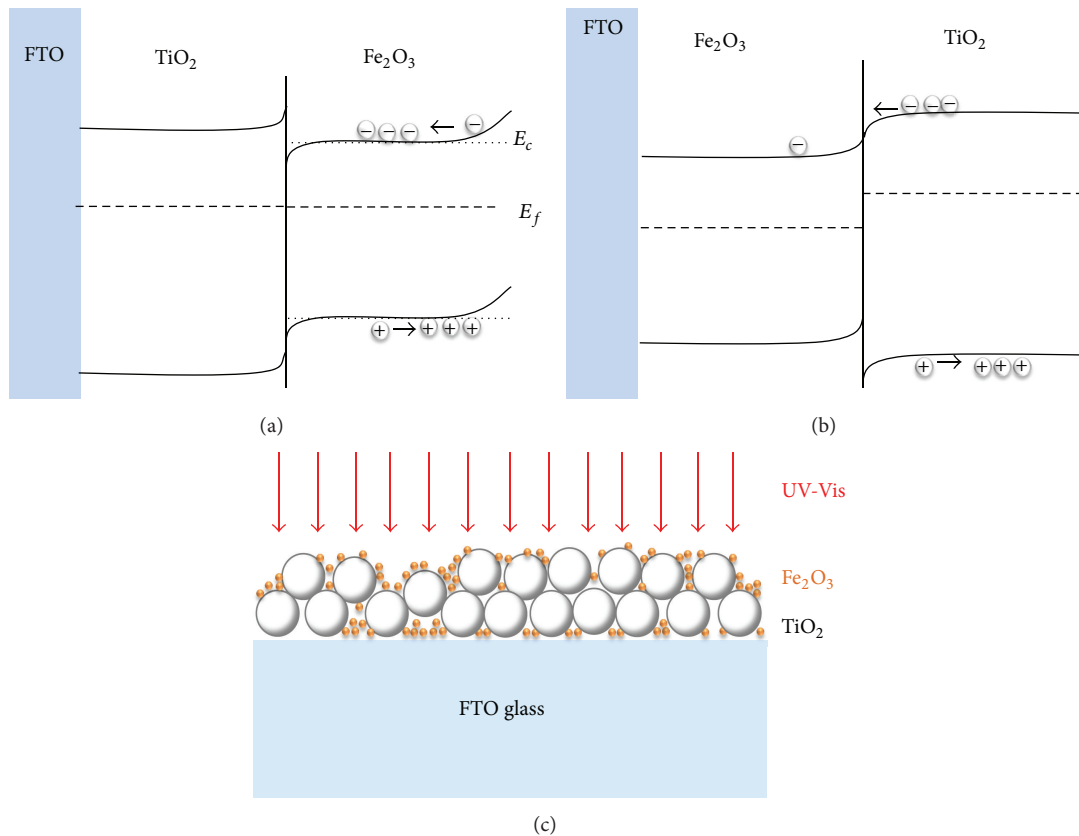


FIGURE 5: Energy band diagrams of (a) $\text{Fe}_2\text{O}_3/\text{TiO}_2/\text{FTO}$ and (b) $\text{TiO}_2/\text{Fe}_2\text{O}_3/\text{FTO}$ photoanode and (c) schematic microstructure of $\text{Fe}_2\text{O}_3\text{-TiO}_2\text{-FTO}$.

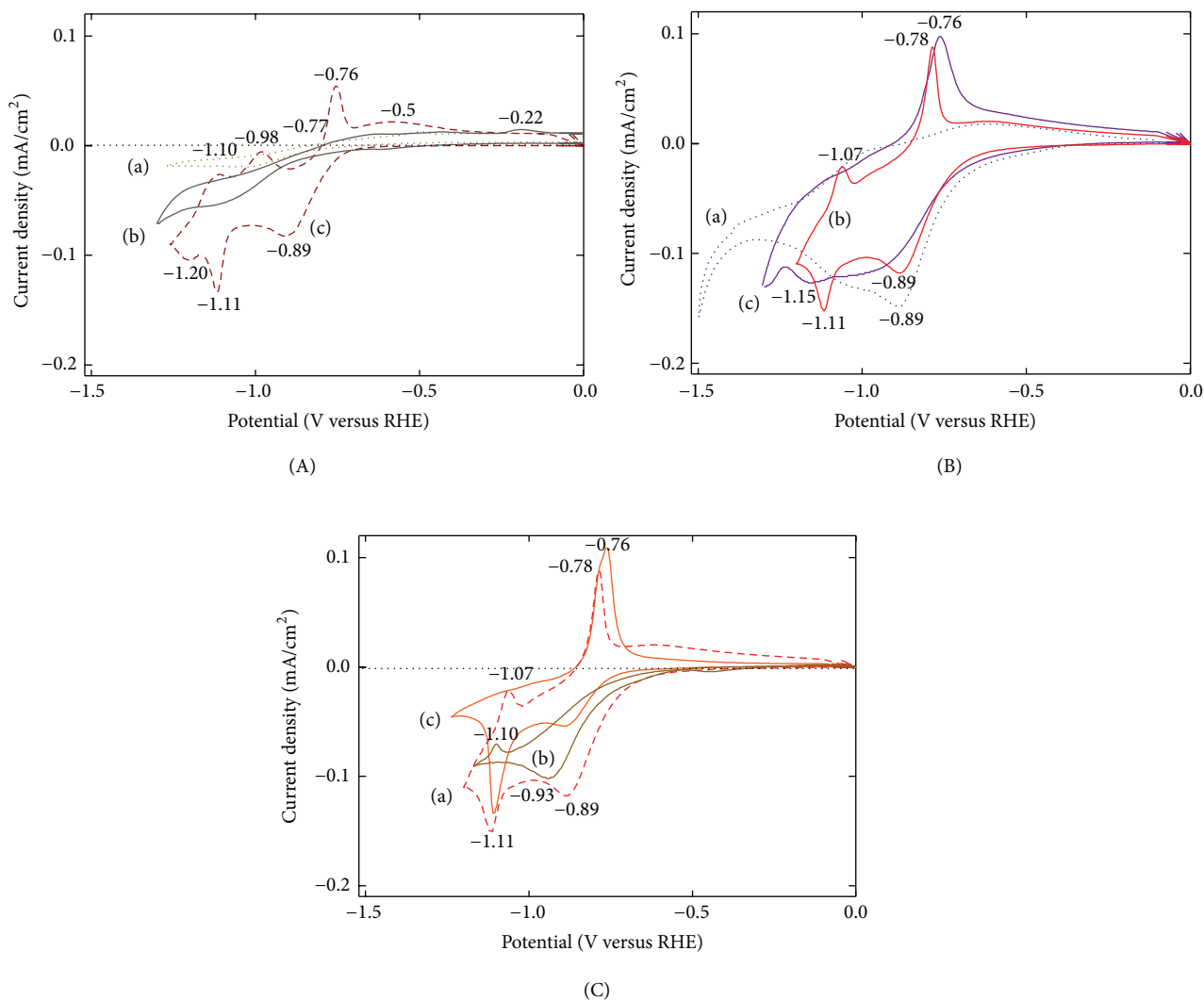


FIGURE 6: CV characteristics measured under 100 mW/cm² UV-Vis illumination: (A) (a) FTO glass, (b) TiO₂/FTO, and (c) Fe₂O₃/FTO samples were investigated after heat treatment at 500°C for 10 min in the air, (B) Fe₂O₃/TiO₂/FTO samples were become heat treated for 10 min in the air at (a) 420°C, (b) 500°C, and (c) 550°C, (C) (a) Fe₂O₃/TiO₂/FTO and (b) TiO₂/Fe₂O₃/FTO heat treated at 500°C for 10 min in the air, and (c) Fe₂O₃/TiO₂/FTO sample double heat treated, corresponding to (d) in Figure 3.

infiltrated to the bottom FTO substrate through TiO₂ particles when TiNT/FTO was placed in the precursor solution of Fe₂O₃. As a result, Fe₂O₃ nanoparticles could also be present in the middle TiO₂ and the bottom FTO layer as depicted in Figure 5(c). Thus, our sample of Fe₂O₃/TiO₂/FTO seemed actually to have an energy band diagram combining both of Figures 5(a) and 5(b), indicating that the photoanode with Fe₂O₃ nanoparticles present even in the middle and bottom substrate is preferable for the performance enhancement.

Oxidation-reduction reactions for the selected photoanode samples were observed by using cyclic voltammetry (CV) to investigate the effect of the coating sequence of constituent films and heat treatment condition on the photoelectrode performance. CV data for the samples of FTO glass, TiO₂/FTO, and Fe₂O₃/FTO were obtained as a reference in Figures 6(A)-(a), 6(A)-(b), and 6(A)-(c), respectively. As expected the sample including Fe₂O₃ showed active reactions with

the applied potential. According to the data (Figure 6(B)) from the Fe₂O₃/TiO₂/FTO samples heat treated at the various temperature of 420 ~ 550°C for 10 min, the sample heat treated at 500°C showed multiple oxidation-reduction peaks, contributing to higher photocurrent density. These results were found to be consistent with *I-V* data of the samples described in Figure 1 where the sample heat-treated at 500°C showed best performance. The sample of Fe₂O₃/TiO₂/FTO which showed best result after heat treatment at 500°C was then compared with TiO₂/Fe₂O₃/FTO sample to see the effect of the location of TiO₂ layer placed in the photoanode, which was also heat treated under the same condition. These samples showed a clear contrast in the results as shown in Figures 6(C)-(a) and 6(C)-(b), respectively: Fe₂O₃/TiO₂/FTO sample produced more and clear oxidation-reduction peaks. On the other hand, the sample of Fe₂O₃/TiO₂/FTO, which was heat treated twice after each coating of TiO₂ and Fe₂O₃

layers, showed an intermediate performance (Figure 6(C)-(c)). These results were all well consistent with the *I-V* data in Figure 3 where the sample of Fe₂O₃/TiO₂/FTO heat treated once (Figure 3(b)) at 500°C showed best performance followed by the sample double heat treated (Figure 3(d)) and TiO₂/Fe₂O₃/FTO sample (Figure 3(c)).

4. Conclusions

Fe₂O₃-TiO₂ based photoanodes for water splitting were synthesized on the FTO substrate and their performance results were understood from the microstructure and energy band aspects. Comparatively, the photoanode (Fe₂O₃/TiO₂/FTO) comprising top layer of α -Fe₂O₃ nanoparticles along with the interlayer having mixed phases of H-TiNT/anatase-TiO₂ showed best performance. The nanoscaled Fe₂O₃ particles with high uniformity were observed to contribute to the performance enhancement. In addition, the presence of the Fe₂O₃ nanoparticles in the middle and bottom layers caused by the infiltration of the precursor solution of Fe₂O₃ during synthesis seemed to modify the energy band structure to more favorable one for efficient electrons transfer. Our current results suggest that the application of the TiO₂ interlayer, together with optimized amount of α -Fe₂O₃ nanoparticles present in the constituent layers, could significantly contribute to the performance improvement of the conventional Fe₂O₃ photoanode.

Acknowledgments

This research was supported by the Basic Science Research Program through the National Research Foundation of Korea funded by the Ministry of Education, Science, and Technology (no. 2011-0016699) and Korea Institute of Energy Technology Evaluation and Planning funded by Ministry of Knowledge Economy. (no. 20113030010050-12-2-200).

References

- [1] T. N. Veziroglu and S. Şahin, "21st century's energy: hydrogen energy system," *Energy Conversion and Management*, vol. 49, pp. 1820–1831, 2008.
- [2] N. Z. Muradov, "How to produce hydrogen from fossil fuels without carbon dioxide emission," *International Journal of Hydrogen Energy*, vol. 18, no. 3, pp. 211–215, 1993.
- [3] E. Y. García and M. A. Laborde, "Hydrogen production by the steam reforming of ethanol: thermodynamic analysis," *International Journal of Hydrogen Energy*, vol. 16, no. 5, pp. 307–312, 1991.
- [4] A. Fujishima and K. Honda, "Electrochemical photolysis of water at a semiconductor electrode," *Nature*, vol. 238, no. 5358, pp. 37–38, 1972.
- [5] A. J. Bard and M. A. Fox, "Artificial photosynthesis: solar splitting of water to hydrogen and oxygen," *Accounts of Chemical Research*, vol. 28, no. 3, pp. 141–145, 1995.
- [6] O. Khaselev and J. A. Turner, "A monolithic photovoltaic-photoelectrochemical device for hydrogen production via water splitting," *Science*, vol. 280, no. 5362, pp. 425–427, 1998.
- [7] J. A. Turner, "Sustainable hydrogen production," *Science*, vol. 305, no. 5686, pp. 972–974, 2004.
- [8] P. Kumar, P. Sharma, R. Shrivastav, S. Dass, and V. R. Satsangi, "Electrodeposited zirconium-doped α -Fe₂O₃ thin film for photoelectrochemical water splitting," *International Journal of Hydrogen Energy*, vol. 36, no. 4, pp. 2777–2784, 2011.
- [9] P. R. Mishra, P. K. Shukla, and O. N. Srivastava, "Study of modular PEC solar cells for photoelectrochemical splitting of water employing nanostructured TiO₂ photoelectrodes," *International Journal of Hydrogen Energy*, vol. 32, no. 12, pp. 1680–1685, 2007.
- [10] Y. Sun, C. J. Murphy, K. R. Reyes-Gil et al., "Photoelectrochemical and structural characterization of carbon-doped WO₃ films prepared via spray pyrolysis," *International Journal of Hydrogen Energy*, vol. 34, no. 20, pp. 8476–8484, 2009.
- [11] A. Kay, I. Cesar, and M. Grätzel, "New benchmark for water photooxidation by nanostructured α -Fe₂O₃ films," *Journal of the American Chemical Society*, vol. 128, no. 49, pp. 15714–15721, 2006.
- [12] D. K. Zhong, J. Sun, H. Inumaru, and D. R. Gamelin, "Solar water oxidation by composite catalyst/ α -Fe₂O₃ photoanodes," *Journal of the American Chemical Society*, vol. 131, no. 17, pp. 6086–6087, 2009.
- [13] M. W. Kanan and D. G. Nocera, "In situ formation of an oxygen-evolving catalyst in neutral water containing phosphate and Co₂⁺," *Science*, vol. 321, no. 5892, pp. 1072–1075, 2008.
- [14] D. K. Zhong and D. R. Gamelin, "Photo-electrochemical water oxidation by cobalt catalyst ("Co-Pi")/ α -Fe₂O₃ composite photoanodes: oxygen evolution and resolution of a kinetic bottleneck," *Journal of the American Chemical Society*, vol. 132, no. 12, pp. 4202–4207, 2010.
- [15] S. D. Tilley, M. Cornuz, K. Sivula, and M. Grätzel, "Light-induced water splitting with hematite: improved nanostructure and iridium oxide catalysis," *Angewandte Chemie*, vol. 49, no. 36, pp. 6405–6408, 2010.
- [16] Y. Guo, X. Quan, N. Lu, H. Zhao, and S. Chen, "High photocatalytic capability of self-assembled nanoporous WO₃ with preferential orientation of (002) planes," *Environmental Science and Technology*, vol. 41, no. 12, pp. 4422–4427, 2007.
- [17] Z. Zhang, M. F. Hossain, and T. Takahashi, "Self-assembled hematite (α -Fe₂O₃) nanotube arrays for photoelectrocatalytic degradation of azo dye under simulated solar light irradiation," *Applied Catalysis B*, vol. 95, no. 3–4, pp. 423–429, 2010.
- [18] J. Matos, J. Laine, and J.-M. Herrmann, "Effect of the type of activated carbons on the photocatalytic degradation of aqueous organic pollutants by UV-irradiated titania," *Journal of Catalysis*, vol. 200, no. 1, pp. 10–20, 2001.
- [19] Y. S. Chaudhary, S. A. Khan, C. Tripathi, R. Shrivastav, V. R. Satsangi, and S. Dass, "A study on 170 MeV Au¹³⁺ irradiated nanostructured metal oxide (Fe₂O₃ and CuO) thin films for PEC applications," *Nuclear Instruments and Methods in Physics Research B*, vol. 244, no. 1, pp. 128–131, 2006.
- [20] A. Mao, J. K. Kim, K. Shin et al., "Hematite modified tungsten trioxide nanoparticle photoanode for solar water oxidation," *Journal of Power Sources*, vol. 210, pp. 32–37, 2012.
- [21] E. Thimsen, F. Le Formal, M. Grätzel, and S. C. Warren, "Influence of plasmonic Au nanoparticles on the photoactivity of Fe₂O₃ electrodes for water splitting," *Nano Letters*, vol. 11, no. 1, pp. 35–43, 2011.

- [22] S. Saremi-Yarahmadi, B. Vaidhyanathan, and K. G. U. Wijayantha, "Microwave-assisted low temperature fabrication of nanostructured α -Fe₂O₃ electrodes for solar-driven hydrogen generation," *International Journal of Hydrogen Energy*, vol. 35, no. 19, pp. 10155–10165, 2010.
- [23] T. Bak, J. Nowotny, M. Rekas, and C. C. Sorrell, "Photo-electrochemical hydrogen generation from water using solar energy. Materials-related aspects," *International Journal of Hydrogen Energy*, vol. 27, no. 10, pp. 991–1022, 2002.
- [24] G. Wang, Y. Ling, D. A. Wheeler et al., "Facile synthesis of highly photoactive α -Fe₂O₃-based films for water oxidation," *Nano Letters*, vol. 11, no. 8, pp. 3503–3509, 2011.
- [25] A. Kay, I. Cesar, and M. Grätzel, "New benchmark for water photooxidation by nanostructured α -Fe₂O₃ films," *Journal of the American Chemical Society*, vol. 128, no. 49, pp. 15714–15721, 2006.
- [26] K. J. Noh, B. R. Kim, G. J. Yoon, S. C. Jung, W. S. Kang, and S. J. Kim, "Microstructural effect on the photoelectrochemical performance of hematite-Fe₂O₃ photoanode for water splitting," *Electronic Materials Letters*, vol. 8, pp. 345–350, 2012.
- [27] H.-J. Oh, K.-J. Noh, H.-K. Ku et al., "Preparation of hydrogen titanate nanotube/FTO glass thin film obtained by the layer-by-layer-self assembling method for water splitting," *Journal of Nanoscience and Nanotechnology*, vol. 11, no. 8, pp. 7210–7213, 2011.
- [28] L. Peng, T. Xie, Y. Lu, H. Fan, and D. Wang, "Synthesis, photoelectric properties and photocatalytic activity of the Fe₂O₃/TiO₂ heterogeneous photocatalysts," *Physical Chemistry Chemical Physics*, vol. 12, no. 28, pp. 8033–8041, 2010.
- [29] K. J. Noh, H. J. Oh, B. R. Kim, S. C. Jung, W. S. Kang, and S. J. Kim, "Photoelectrochemical properties of Fe₂O₃ supported on TiO₂-based thin films converted from self-assembled hydrogen titanate nanotube powders," *Journal of Nanomaterials*, vol. 2012, Article ID 475430, 6 pages, 2012.
- [30] K. J. Noh, H. J. Oh, H. K. Ku et al., "Annealing effect on the microstructure and electrochemical properties of Fe₂O₃/H-TiNT/FTO thin film," *Journal of Nanoscience and Nanotechnology*, vol. 13, pp. 1863–1866, 2013.
- [31] H. J. Oh, K. J. Noh, B. R. Kim, W. S. Kang, S. C. Jung, and S. J. Kim, "Fabrication of Fe₂O₃/TiO₂ photoanode for improved photoelectrochemical water splitting," *Japanese Journal of Applied Physics*, vol. 52, Article ID 01AC15, 2013.
- [32] Y. Wang, T. Yu, X. Chen et al., "Enhancement of photoelectric conversion properties of SrTiO₃/ α -Fe₂O₃ heterojunction photoanode," *Journal of Physics D*, vol. 40, no. 13, pp. 3925–3930, 2007.